Ultrafast dynamics of small quantum systems studied using electron-ion coincidence spectroscopy

Ganguly, Smita

2023

[Link to publication](#)

Ultrafast dynamics of small quantum systems

Studied using electron-ion coincidence spectroscopy

SMITA GANGULY
DEPARTMENT OF PHYSICS | FACULTY OF SCIENCE | LUND UNIVERSITY

Ultrafast dynamics of small quantum systems

studied using electron-ion coincidence spectroscopy

Smita Ganguly

Organization LUND UNIVERSITY	Document name DOCTORAL DISSERTATION
Division of Synchrotron Radiation Research Department of Physics, Box 118 S-22100 Lund	Date of issue 2023-05-22
Author Smita Ganguly	Sponsoring organization

Title and subtitle Ultrafast dynamics of small quantum systems studied using electron-ion coincidence spectroscopy

Abstract

Studying how small quantum systems, like molecules and clusters, interact with X-rays is crucial to understanding the ultrafast processes that occur in nature on incredibly short timescales, ranging from femtoseconds to picoseconds. X-rays excite small quantum systems to unstable core hole states, leading to a cascade of phenomena, including Auger decay, nuclear rearrangement, and dissociation. The dissociation of molecules is influenced by the initial site of X-ray excitation, as well as the properties of the Auger populated states, such as charge localization and internal energy. In clusters, the dissociation process depends on intermolecular interactions, cluster size, and geometry. The interplay between electronic and nuclear dynamics in core-excited/ionized molecules and clusters is a critical factor that needs to be assessed.

This thesis investigates X-ray-induced fragmentation of molecular adamantane and CO_2 clusters using synchrotron radiation. The kinematics of molecular and cluster fragmentation is measured using advanced techniques, such as 3D momentum imaging of the ion fragments and multiparticle coincidence spectroscopy. Site-selective fragmentation of the carbon cage of the adamantane molecule is studied using Auger-electron Photoion coincidence spectroscopy, revealing the influence of the core-hole site on the Auger decay and dissociation process. Statistical data analysis treatment is developed and implemented to remove background contamination in the coincidence data using experimental random coincidences. The results highlight that the fragmentation of adamantane cation and dication is a complex dynamical process with competing relaxation pathways involving cage opening, hydrogen migration, and carbon-carbon bond breaking. Additionally, the thesis investigates the photoreactions of core-ionized CO_2 clusters, reporting a significantly increased production of O_2^+ compared to isolated CO_2 molecules. Through quantum chemistry calculations and multi-coincidence 3D momentum imaging, the study determined that the enhanced production of O_2^+ is due to a size-dependent structural transition of the clusters. The study also proposes two relevant photoreactions involving intermolecular interactions.

This thesis highlights the complexity of core-hole dynamics in molecular and cluster chemistry and emphasizes the need for meticulous experimental and theoretical investigations of the underlying mechanisms. It also discusses the relevance of the results in the context of X-ray-induced astrochemistry. Indeed, the experiments presented are conducted in vacuum chambers in a controlled environment and can crudely replicate the conditions found in astrophysical environments. From the adamantane study, we conclude that X-ray absorption emphatically results in dissociation into smaller hydrocarbons and low photostability can play a part in the absence of diamondoids in the interstellar medium. From the CO_2 clusters study, we found an enhancement in the O_2^+ yield, which can significantly influence the ion balance in CO_2-rich atmospheres like Mars.

Key words Electron-ion coincidence spectroscopy, cluster photodissociation, fragmentation dynamics, molecular photodissociation, site selective fragmentation, cluster astrochemistry, CO_2 cluster, adamantane.

Classification system and/or index terms (if any)	
Supplementary bibliographical information	Language English
ISSN and key title	**ISBN** 978-91-8039-725-4 (print) 978-91-8039-726-1 (pdf)
Recipient´s notes	**Number of pages** 195	Price
	Security classification	

Signature   Date 2023-05-02

Ultrafast dynamics of small quantum systems

studied using electron-ion coincidence spectroscopy

Smita Ganguly

LUND
UNIVERSITY

Cover image: XPS detector image of Xenon recorded using EPICEA, combined with Vincent van Gogh's '*The Starry Night*' painting using AI algorithm *Deep Dream Generator*.

Back cover: Adorable picture of my pet rabbit Wally.

Quotes page: 'Water colour painting of traditional Japanese street' generated using AI algorithm *Deep Dream Generator*.

*"Yes, you see, there's no such thing as **coincidence**. There are no accidents in life. Everything that happens is the result of a calculated move that leads us to where we are."*

— J.M. Darhower

Contents

Abstract

Studying how small quantum systems, like molecules and clusters, interact with X-rays is crucial to understanding the ultrafast processes that occur in nature on incredibly short timescales, ranging from femtoseconds to picoseconds. X-rays excite small quantum systems to unstable core hole states, leading to a cascade of phenomena, including Auger decay, nuclear rearrangement, and dissociation. The dissociation of molecules is influenced by the initial site of X-ray excitation, as well as the properties of the Auger populated states, such as charge localization and internal energy. In clusters, the dissociation process depends on intermolecular interactions, cluster size, and geometry. The interplay between electronic and nuclear dynamics in core-excited/ionized molecules and clusters is a critical factor that needs to be assessed.

This thesis investigates X-ray-induced fragmentation of molecular adamantane and CO_2 clusters using synchrotron radiation. The kinematics of molecular and cluster fragmentation is measured using advanced techniques, such as 3D momentum imaging of the ion fragments and multiparticle coincidence spectroscopy. Site-selective fragmentation of the carbon cage of the adamantane molecule is studied using Auger-electron Photoion coincidence spectroscopy, revealing the influence of the core-hole site on the Auger decay and dissociation process. Statistical data analysis treatment is developed and implemented to remove background contamination in the coincidence data using experimental random coincidences. The results highlight that the fragmentation of adamantane cation and dication is a complex dynamical process with competing relaxation pathways involving cage opening, hydrogen migration, and carbon-carbon bond breaking. Additionally, the thesis investigates the photoreactions of core-ionized CO_2 clusters, reporting a significantly increased production of O_2^+ compared to isolated CO_2 molecules. Through quantum chemistry calculations and multi-coincidence 3D momentum imaging, the study determined that the enhanced production of O_2^+ is due to a size-dependent structural transition of the clusters. The study also proposes two relevant photoreactions involving intermolecular interactions.

This thesis highlights the complexity of core-hole dynamics in molecular and cluster chemistry and emphasizes the need for meticulous experimental and theoretical investigations of the underlying mechanisms. It also discusses the relevance of the results in the context of X-ray-induced astrochemistry. Indeed, the experiments presented are conducted in vacuum chambers in a controlled environment and can crudely replicate the conditions found in astrophysical environments. From the adamantane study, we conclude that X-ray absorption emphatically results in dissociation into smaller hydrocarbons and low photostability can play a part in the absence of diamondoids in the interstellar medium. From the CO_2 clusters study, we found an enhancement in the O_2^+ yield, which can significantly influence the ion balance in CO_2-rich atmospheres like Mars.

Popular Science Summary

Have you ever wondered how X-rays from the Sun can activate unique chemistry in the atmosphere of Mars? Or how the absence of certain hydrocarbons in astronomical observations can be explained by their interaction with ionizing radiation? These are the fascinating questions that are explored in this PhD thesis using X-rays and state-of-the-art electron-ion spectrometers. Are you ready to explore the tiny world of molecules and clusters at the quantum level? Buckle up because things are about to get small and fast!

When a molecule absorbs an X-ray photon, it *excites* the molecule to a highly unstable state. This excited molecule then relaxes to reach a stable state, releasing charged particles like electrons and ions in the process. By analyzing the properties of these particles, we can track the molecule's evolution over time. However, this process happens very quickly, on a timescale of femtoseconds, so specialized experimental methods are required to capture these *ultrafast dynamics*. This thesis focuses on studying the ultrafast behavior of photoexcited molecules and nano-clusters by detecting the charged particles they emit simultaneously. This technique is called '*coincidence detection*'. The study investigates the implications of these photoreactions, both from a fundamental physics perspective and in specific astrochemistry scenarios.

Planetary atmospheres contain many molecular clusters, formed by the condensation of molecules into small nanoparticles that eventually grow into clouds. CO_2 clusters are expected to exist in CO_2-rich atmospheres such as Mars, where the Sun's X-rays can activate unique photochemical reactions. In Paper I, we studied CO_2 clusters that were ionized by X-rays using complete momentum imaging of ions. We investigated the high production of O_2^+ ions using both experimental and theoretical methods. Hydrocarbons are a significant part of the space between stars, but a particular kind of hydrocarbon, diamondoids, has not been observed in space. In Papers II and III, we investigate the photochemistry of adamantane, which is the smallest diamondoid, using electron-ion coincidence detection. Our observations reveal that adamantane breaks down into smaller hydrocarbons upon absorbing X-ray photons and could be responsible for the absence of diamondoids in astronomical observations. We also analyze the mechanisms behind the loss of hydrogen in adamantane and compare it to other hydrocarbons.

The scientific questions discussed in this thesis require advanced experimental methods. Another part of this thesis, therefore, describes the commissioning of a new electron-ion spectrometer for use in future experiments at the MAXIV laboratory (paper IV). Data analysis routines for electron-ion coincidence data are also developed and discussed for the different spectrometers used in this work.

List of Papers

Paper I

The origin of enhanced O_2^+ production from photoionized CO_2 clusters

Smita Ganguly, Dario Barreiro-Lage, Noelle Walsh, Bart Oostenrijk, Stacey L. Sorensen, Sergio Díaz-Tendero and Mathieu Gisselbrecht

I analyzed the experimental data, made the figures in the manuscript and was the main responsible for writing the manuscript.

Paper II

Coincidence study of core-ionized adamantane: site-sensitivity within a carbon cage?

Smita Ganguly, Mathieu Gisselbrecht, Per Eng-Johnsson, Raimund Feifel, Paul-Antoine Hervieux, Zeinab Alfaytarouni, Reinhold F. Fink, Sergio Díaz-Tendero, Aleksandar R. Milosavljević, Patrick Rousseau and Sylvain Maclot.

I participated in the experimental beamtime via Zoom and performed online analysis during the beamtime. I wrote the data analysis code and analyzed the experimental data. I was the main responsible for writing the manuscript.

Paper III

Resonant inner-shell photofragmentation of Adamantane

Smita Ganguly, Mathieu Gisselbrecht, Per Eng-Johnsson, Raimund Feifel, Sergio Díaz-Tendero, Eva Muchová, Aleksandar R. Milosavljević, Patrick Rousseau and Sylvain Maclot.

I participated in the experimental beamtime via Zoom and performed online analysis during the beamtime. I wrote the data analysis code and analyzed the experimental data. I wrote the manuscript with Mathieu Gisselbrecht.

Paper IV

ICE – A mobile reaction microscope end station for AMO science at MAX IV Laboratory

Noelle Walsh, Smita Ganguly, Bart Oostenrijk, Georgia Michailoudi, Stacey L. Sorensen, Mathieu Gisselbrecht, Ville Lindblom, Maxim Tchaplyguine, Alexei Preobrajenski, Alexander Generalov, Gunnar Öhrwall and Johan Adell.

In manuscript

I took part in preparing and performing the commissioning experiments of the ICE end station.

Acknowledgements

<div style="text-align: right">

The road has been long,

But every step was worth it.

Journey's end is in sight.

</div>

As I look back on my PhD journey, my heart fills with gratitude for the incredible people who have been a part of this academic adventure. I can hardly believe it's been 4.5 years since I first arrived in Sweden as a bright-eyed 23-year-old, ready to explore new horizons. This journey has been nothing short of transformative, both personally and professionally, thanks to the unwavering support and guidance of so many amazing individuals.

I want to thank my main supervisor, Mathieu Gisselbrecht, whose expertise, support, and mentorship have been priceless throughout this process. He has helped me hone my writing skills and given me the independence to pursue my research goals. I would also like to thank my co-supervisor, Noelle Walsh, for her invaluable support and insights. I am grateful for her contributions to my research, and I thoroughly enjoyed working with her on the ICE beamtimes. Her inspiring presence has left an indelible mark on my academic journey. Additionally, I want to thank my other co-supervisor, Per Eng-Johnsson, for his input on my thesis. I owe a great deal to Sylvain Maclot, who helped me with data analysis and manuscript writing and has been an inspiration. I also want to thank Sergio Díaz-Tendero, Patrick Rousseau, Aleksandar Milosavljević, Stacey Sörensen and Darío Barreiro Lage for their contributions to my research.

I want to thank everyone at SLJUS, who has created an incredibly supportive and vibrant community. I couldn't have made it this far without the support and encouragement of my friends. From Zhaojun and our gym and dance classes to Yuhe and our long conversations about anything and everything, to Nazanin, Foqia, and Fatemah for being my emotional rocks through the ups and downs, and to Akash, Rohit, Yi, Zhihua, Annika, and Alex for the unforgettable weekend gatherings and travels.

I am grateful for the love and support of Shaswata, who has been with me every step of the way, cheering me on and helping me stay motivated. I want to thank my bunny roommate Wally, who has been a constant source of warmth and entertainment. He has taught me not to care about unimportant things. Finally, I want to thank my brother and my best friend Samiksha for their unwavering support throughout.

At the end, I would dedicate this thesis to my 17-year-old self, when I did not have enough money to join a bachelor's program. Thank you for not giving up on education, for pursuing your love for physics, and for the determination, perseverance, and hard work that has led me to this point. Without your passion and dedication, I would not be where I am today. I am grateful for your courage and resilience, and I hope that this work honors your spirit and inspires others to follow their dreams.

To all of you who have been a part of this journey, thank you from the bottom of my heart. Your contributions, love, and support have made this experience more meaningful than I could have ever imagined. As I embark on new adventures, I carry with me the memories, lessons, and connections that have made this journey so incredible.

1 Introduction

The fate of light-molecule interaction is decided by the amount of energy deposited by the absorbed photon into the electronic and nuclear degrees of freedom of the molecule. If the energy transferred by the photon is greater than the binding energy of the electrons, the molecule will be *ionized* - a process which instigates fascinating ultrafast dynamics. The study of ultrafast dynamics of ionized systems is a rapidly developing field that holds promise for understanding a wide range of physical and chemical phenomena. For understanding small quantum systems like molecules and clusters, it is vital to study the complex interplay between electronic and nuclear motion.

The research of photoionized quantum systems can be traced back to the discovery of the photoelectric effect by Hertz in 1881 and its interpretation by Einstein in 1905[1]. In the 1960s, Siegbahn and colleagues developed photoelectron spectroscopy[2,3] for chemical analysis of matter based on the photoelectric effect. After a century of research on photoionized systems, today real time imaging of photoelectron emission in the attosecond timescale[4] is possible. The by-product of the photoelectric effect, the ion, also became a topic of research to study the final states of the molecule after a longer timescale of up to a few microseconds. Ion spectroscopy has evolved from measuring only the mass-to-charge ratio to precision measuring of the quantum states and structural geometry of the ions[5]. At present, we can measure the electrons and ions which are the final products of photoionization but the intermediate processes that occur in sub femtosecond timescale and lead to these final products are not completely understood[6].

The ultrafast dynamics of photoionized molecules and clusters can be studied using synchrotron radiation and '*nature's pump-probe scheme*'[7]. Soft X-ray photons from synchrotron act as 'pump' and are used to selectively excite or ionize a core electron from the ground state of the molecule to a highly unstable *core-hole* state with a lifetime of few femtoseconds[8]. The core-hole state relaxes via Auger decay to a final ionic state which can further fragment into multiple ions. These electrons and ions produced in the aftermath of core-hole state creation act as our 'probe'.

In this thesis, the ultrafast dynamics of complex molecules and clusters are studied using synchrotron radiation along with sophisticated spectrometers and detectors to record the momentum and position of the charged particles. 3D momentum imaging of the final products, the electrons and ions is used to reconstruct the complete three-

dimensional map of the ionization process and gain insights into the fragmentation of the ions. Ultrafast processes in core ionized systems such as molecular structural changes, charge transfer, hydrogen loss, bond-breaking and intermolecular chemical reactions are discussed for molecular adamantane and carbon dioxide clusters.

Chapter 2 covers the basic theories about photoionized systems and Chapter 3 describes the principles of coincidence spectroscopy and the experimental setup used. The data analysis routines developed and used in this work are explained in Chapter 4. Chapter 5 summarises the results about the ultrafast dynamics of adamantane and CO_2 clusters.

The reactions studied in this thesis under controlled environments in ultrahigh vacuum chambers are relevant to real life chemistry. Below two possible applications in astrochemistry and atmospheric chemistry are described briefly.

Hydrocarbons in Interstellar medium

Hydrocarbons are ubiquitous in the interstellar medium, the space between stars consisting of gas and dust particles. Interstellar hydrocarbons are believed to form through a variety of chemical processes, such as the photodissociation of larger molecules, the reaction of atomic hydrogen with carbon-containing molecules, and the ion-molecule reactions that take place in the gas phase[9]. These hydrocarbons are detected through their spectral signatures, and their abundances and distributions provide important clues about the physical and chemical conditions of the interstellar medium. Some of the most studied interstellar hydrocarbons are polycyclic aromatic hydrocarbons[10–12] (PAHs), which are complex planar organic molecules that play a role in the formation of interstellar dust grains.
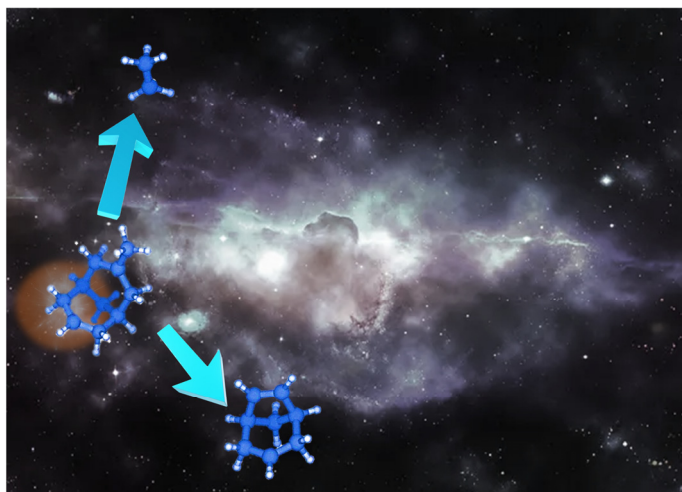
Figure 1. Schematic of dissociating hydrocarbons in the interstellar medium.

Diamondoids are also expected to be present in the interstellar medium[13], but to date no spectral signature diamondoids have been observed[14,15]. The absence of diamondoids is ascribed to the dissociation into smaller hydrocarbons after absorbing ionizing radiation (see Fig. 1). In this thesis, we studied the interaction of adamantane, the smallest diamondoid molecule with ionizing X-rays.

Clusters in atmospheres

In planetary atmospheres, free molecules condensate to form molecular clusters which exist as precursors for larger particle formation[16–19]. When the atmospheric conditions are appropriate, the clusters further coagulate to form fine particles which grow into cloud nuclei as shown in Fig. 2. In the Earth's atmosphere, clusters play a crucial role in the formation of clouds and precipitation, as they can act as nuclei for the condensation of water vapor. Atmospheric particles affect the radiative properties of the atmosphere, as they can scatter and absorb solar radiation, which has important implications for climate and weather patterns.

| Inorganic and organic vapours | Stable clusters | Fine particles | Cloud droplets |
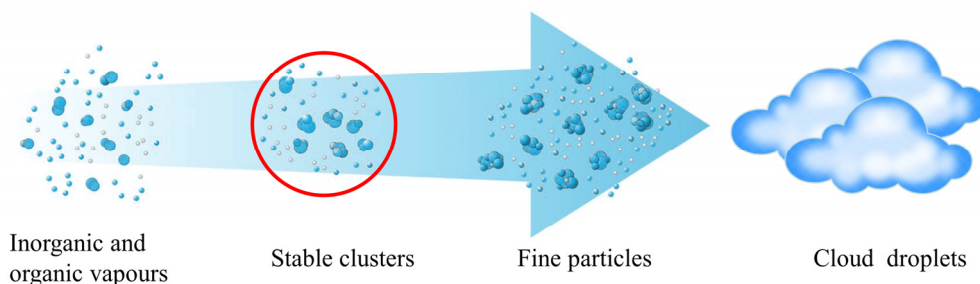
Figure 2. Particle growth in atmospheres adapted from ref[17]. The free molecules nucleate into stable clusters which further grow to form fine particles which eventually form cloud droplets. The growth depends on the atmospheric conditions like vapour pressure, temperature, composition. In this thesis, the chemical reactions of stable clusters (< 2 nm) are explored.

CO_2 ice aerosols[20] and CO_2 ice clouds[21–24] have been detected at various altitudes between 60 and 100 km in CO_2-rich atmospheres such as that of Mars. The composition of these particles is a topic of discussion, as the exact nature of the particles remains unknown. While classical nucleation theories[25] suggest that CO_2 molecules cannot form larger particles in the Martian atmosphere through homogeneous nucleation, recent quantum chemical calculations suggest that pure CO_2 clusters may exist at high altitudes[26]. As the Martian ionosphere at higher altitudes (> 70 km) is significantly affected by solar soft X-rays[27], they can interact with CO_2 particles. In this thesis, the fragmentation of CO_2 clusters is studied using soft X-rays and the size dependence of the induced photochemistry is investigated.

It is worth noting that an alternative approach of studying the real-time dynamics uses pump-probe spectroscopy, which involves using a first laser pulse (the 'pump')

to excite the molecule, followed by a second laser pulse (the 'probe') to measure the resulting changes in the molecule's properties. Femto-chemistry introduced by Zewail uses laser pump-probe spectroscopy to study the ultrafast dynamics of chemical bonding in matter[28,29]. Recently, strong-field attosecond laser sources are used to study the molecular dynamics[30] of diatomic molecules[31–34], small molecules[35–38] and small clusters[39,40]. The development of Free electron lasers (FELs) will also facilitate novel pump-probe schemes like attosecond 3D momentum imaging of core ionized systems[41–43]. During my doctoral studies, I have participated in pump-probe experiments using attosecond laser source and FEL, but they are not presented here since it is not the core of my work.

2 Theory

This chapter presents a detailed overview of the theoretical concepts required to comprehend light-matter interactions of small quantum systems. The first section covers how X-rays can create a core hole state in a molecule or cluster by ionizing an innermost electron. The second section delves into the relaxation of the core hole state, where the ionized system returns to a stable configuration through various decay mechanisms like Auger decay and nuclear relaxation. The third section examines the fragmentation of molecules with multiple charges and the different factors that can affect this process. Lastly, the fourth section investigates the fragmentation of molecular clusters and how the size and structure of the cluster impact this process. This chapter emphasizes the localization and transfer of charge in molecules and clusters and its influence on fragmentation. This thesis is based on experimental work that aims to explore and understand the phenomena discussed here.

2.1 Creating a core hole state

When a small quantum system like a molecule or a cluster absorbs a photon of sufficient energy a highly unstable core-hole is created. The absorbed photon energy is used to overcome (or partly overcome) the binding energy of the core electron and the excess energy is used for electronic relaxation of the core hole state. For a given small quantum system, there is a finite probability of photo-absorption that depends on the photon energy. Consider a two-state system, initially the molecule is in the ground state with wave function $|\psi_i\rangle$ at energy E_i, and after absorbing a single photon it reaches a core-hole state $|\psi_c\rangle$ with energy E_c. Such a photoexcitation shown in Fig 2.1 (a) is called as *resonant core excitation* in this thesis.

The transition rate of resonant core excitation can be estimated using the *Fermi's golden rule*[44–46] which describes the transition rate between two quantum states in a system when an external perturbation like a photon beam is introduced. The Fermi's golden rule states that the transition rate, or the probability per unit time of the system transitioning from an initial state to a final state, is proportional to the intensity of the perturbation, the density of final states available for the system to transition into, and the square of the matrix element that describes the perturbation.

The transition rate between the ground state and the core hole state can be estimated using,

$$\xi(h\nu) = \frac{4\pi^2}{h} |\langle\psi_c|H'|\psi_i\rangle|^2 \, \delta(E_c - E_i - h\nu) \qquad (2.1)$$

where h is the Planck constant, H' is the perturbation Hamiltonian and $\delta(E_c - E_i - h\nu)$ is the energy conservation delta function. The term $|\langle\psi_c|H'|\psi_i\rangle|$ is the matrix element that represents the coupling between the initial and final states of the system. The transition rate ξ depends on the photon energy and is the highest for the resonance case when $h\nu = E_c - E_i$ and at the resonant photon energy the transition rate increases linearly with the photon beam intensity. These highly excited core hole states in the molecule are identified using absorption spectroscopy near the ionization threshold, later referred to as Near edge X-ray absorption spectroscopy (NEXAFS).
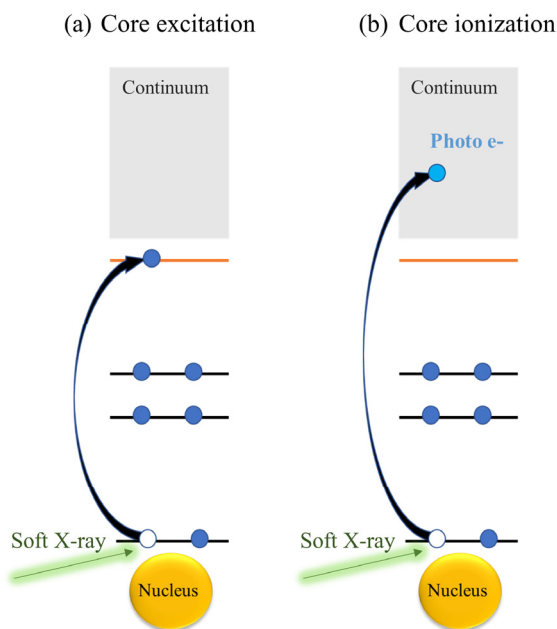
Figure. 2.1 A simplified representation of the photo-absorption process in a molecule leading to resonant excitation of a core electron in (a) and core ionization in (b). When a soft X-ray photon is absorbed, if the photon energy is equal to the energy difference between the binding energy of the core electron and an unoccupied outer orbital near the continuum then the molecule is *resonantly* excited, promoting the core electron to this unoccupied orbital. Whereas, if the photon energy is higher than the binding energy of the core electron, the electron is promoted to the continuum of ionization i.e. a photo electron is emitted and the molecule is ionized. In both the cases a core hole is created in the molecule.

If the photon energy is higher than the core electron ionization threshold (IT_{core}), a photoelectron with kinetic energy e_{pKE} is emitted. In this case, there will be a continuum of core hole states and the transition or photoionization rate will depend on the density of states in the continuum the $\rho(e_{pKE})$. Such a photoexcitation shown in Fig 2.1 (b) is called as *core ionization* in this thesis. The photoionization rate is given by,

$$\xi(h\nu > IT_{core}) = \frac{4\pi^2}{h} |\langle \psi_c | H' | \psi_i \rangle|^2 \, \rho(e_{pKE}) \qquad (2.2)$$

The photoionization rate is the highest near the ionization threshold and then decays rapidly with increasing photon energy as the matrix element $|\langle \psi_c | H' | \psi_i \rangle|$ tends to zero[47].

In a molecule, the wavefunctions of inner-shell core electrons are confined or *localized* near the nuclei and resemble atomic orbitals[48]. The binding energy of these core electrons in a molecule, however, are different from atomic orbitals and are chemically shifted like in the ESCA molecule[2,3]. The core hole state created after core excitation or ionization can be localized on a specific atom or delocalized over chemically equivalent atoms in the molecule[49,50]. Irrespective of charge distribution, the creation of a core hole dramatically changes the Coulomb field in the molecule and leads to rapid electronic and nuclear relaxation of the molecule.

2.2 Relaxation of the core hole state

In a small quantum system after core excitation or ionization, the core hole state typically relaxes via Auger[1] electron emission within the few femtoseconds. During the lifetime of the core hole state, nuclear motion such as geometry change, or even direct dissociation can occur before Auger decay. The excited core hole state's lifetime is proportional to the inverse of the sum of all partial transition rates to various final states. The complex interplay between electronic and nuclear motion during the relaxation of the core hole state is discussed in this section.

2.2.1 Auger decay

The dominant relaxation process in light atoms is Auger decay, in which one valence electron fills the core hole and a second valence electron is ejected into the continuum. Alternatively, in heavy atoms, the core hole state decays to lower-lying states via radiative i.e., X-ray fluorescence processes. In this thesis only light atom

---

[1] Also known as Auger-Meitner decay since the effect was first discovered by Lise Meitner in 1922.

(C, O) containing molecules and clusters are studied therefore only Auger decay is considered here.

Due to the localization of core orbitals in molecules, only the valence electron wave functions that are in proximity to the excited atom will contribute to the Coulomb matrix element that describes the partial decay cross section (known as the one-center approximation)[51]. The partial Auger decay rate strongly depends on the given valence electron density near the core hole. Electronegative ligands are expected to lower the Auger rate, increasing the lifetime of the corresponding core-excited or ionized state.

(a) Participator auger decay   (b) Spectator auger decay   (c) Normal auger decay
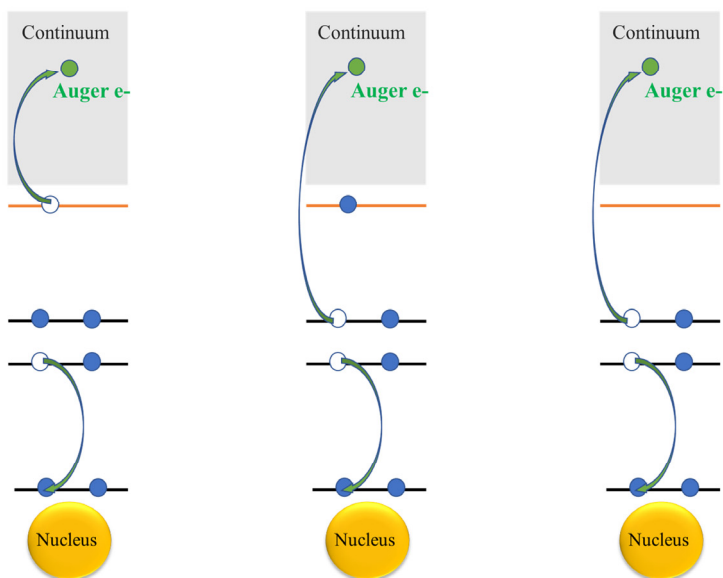
Figure. 2.2 A simplified representation of the electronic relaxation of a core hole via Auger decay in a molecule. After core excitation, the molecule can undergo either participator Auger decay shown in (a) or spectator Auger decay shown in (b). In participator Auger decay, the electron in the previously unoccupied orbital participates in the decay process, while in spectator decay, it does not. In both cases an Auger electron is emitted and the molecule is primarily singly charged. After core ionization, the molecule undergoes normal Auger decay shown in (c), where an electron from the valence shell fills the core hole releasing excess energy that is transferred to the emitted Auger electron and the molecule is doubly charged.

To obtain the total Auger rate, a summation over all possible final states must be performed. After core excitation or ionization, the Auger decay rate[52] from the initial core hole $|\psi_c\rangle$ state to the final state $|\psi_f\rangle$ is calculated by,

$$\Gamma = \left| \sum_{a<b} \langle \psi_f | c_b c_a c_{core}^\dagger | \psi_c \rangle \left\langle \Phi_{core} \Phi_\epsilon \left| \frac{1}{r_{12}} \right| \Phi_a \Phi_b \right\rangle \right|^2 \qquad (2.3)$$

here Φ_a and Φ_b are all possible valence orbital combinations involved in the Auger decay. The first term in (2.3) evaluates the overlap integral of the adapted initial wavefunction $c_b c_a c_{core}^\dagger | \psi_c \rangle$ and the final wavefunction $| \psi_f \rangle$, where c_a and c_b are the annihilation operators of two valence electrons from the orbitals a and b, $c_{core}^\dagger$ is the creation operator of an electron that fills the core hole. The second term in (2.3) represents the electron interaction integral between the two valence orbitals Φ_a and Φ_b with the emitted Auger electron in continuum Φ_ϵ and the core electron Φ_{core}. A larger number of accessible states for Auger decay shortens the lifetime of the core hole, which is the main reason for the decreasing core hole lifetime when moving from a free atom to the same atom in a molecule. However, this trend might be subject to exceptions related to the existence of symmetry-based propensity rules. Typical K-shell core hole lifetimes of light atoms are a few femtoseconds and calculated by measuring linewidth of the Auger electron spectrum[8,53].

The molecule in a core hole state spontaneously undergoes relaxation via Auger decay. Resonant Auger electron spectroscopy (RAES) is used to study the Auger decay of a (neutral) core-excited state. In the case of resonant core excitation, there are two possible deexcitation mechanisms via participator or spectator Auger decay shown in Fig. 2.2 (a) and (b) respectively. Participator-type Auger decay results in one valence hole and one Auger electron is emitted, therefore the final state after the decay is cationic (1h state). Whereas in the case of spectator Auger decay two holes are created and an Auger electron is emitted, the final state after the decay is a cationic (2h-1p state) with two valence holes and an electron in the previously unoccupied outer orbital. While this nomenclature of spectator and participator decay is common in Auger spectroscopy, the final electronic states after Auger decay may also have a mixed 1h and 2h-1p character[54]. The kinetic energy of the Auger electron (e_{KE}) depends on the mechanism of Auger decay, for participator type of decay the value of e_{KE} depends on the excitation photon energy. For spectator type of decay, the value of e_{KE} is independent of the excitation photon energy. RAES data is often presented in terms of binding energy (E_{bin}). The binding energy of the final cation state can be calculated as,

$$E_{bin} = h\nu - e_{KE} \qquad (2.4)$$

Normal Auger electron spectroscopy (AES) is used to study the Auger decay of a core ionized state. After normal Auger decay shown in Fig. 2.2 (c), involving two valence shells a and b, the final state is a dication (2h state) and the kinetic energy of the Auger electron is given by,

$$e_{KE} = E_{core} - E_a - E_b \qquad (2.5)$$

Here E_{core}, E_a and E_b are the binding energies of the K, a and b shells respectively. The value of E_{core} is experimentally measured using X-ray photoelectron spectroscopy (XPS). The value of e_{KE} after normal Auger decay is independent of the excitation photon energy.

After core-hole relaxation, the resulting state of Auger decay may still end up in the continuum of the next higher charge state, leading to subsequent cascade of Auger decays[55]. Alternatively, the Auger populated states can further autoionize via electron shake-off processes[56].

2.2.2 Nuclear motion in the core hole state

Due to their greater mass, nuclear dynamics generally occur at much slower timescales than electron dynamics, leading to the well-established Born-Oppenheimer approximation, where electron and nuclear dynamics are considered decoupled. However, for highly excited systems, nuclear motion on strongly repulsive adiabatic potential energy surfaces can be very fast, causing electron and nuclear dynamics to occur on comparable timescales and become strongly coupled in molecules[57–59] and clusters[60–62].

For molecules and clusters, the symmetry of the stable geometry of the core-excited or core-ionized state often differs from that of the ground state, leading to nuclear motion towards the new stable geometry with different symmetry[63–66]. This nuclear motion causes symmetry breaking and affects the subsequent electronic decay and ionic fragmentation. Classic examples of nuclear motion in core hole states are bending of the core excited CO_2 molecule[66–68] and asymmetric vibrations of core excited or ionized BF_3 molecule[64,69,70].

In some special cases, nuclear motion in the core hole state after resonant excitation can result in *ultrafast dissociation* before Auger decay[71]. If the core hole excited state has antibonding character, then the dissociative nature of the excited state drives rapid nuclear motion, this leads to ultrafast dissociation in the femtosecond timescale. The nuclear dynamics in such a repulsive core hole state competes with Auger decay like in HBr molecule[72]. In such a case the Auger decay can be delayed and occurs in the fragment of the molecule with a characteristic sharp 'atomic' peak[73,74]. After resonant core excitation, if the core electron is excited to a previously vacant antibonding orbital[75,76] (like C $1s \rightarrow \pi^*$ transition) can trigger *ultrafast dissociation* before electronic relaxation. After core ionization, however, removing a core electron has no direct effect on the bonding of the molecule or the cluster, therefore these core hole states are usually bound and do not undergo ultrafast dissociation[77].

2.3 Fragmentation of multiply-charged molecules

After Auger decay and autoionization processes, an unstable multiply charged molecule is formed which subsequently decomposes into fragments along the dissociation path on the potential energy surface of the final Auger-populated state. The fragmentation of the multiply charged molecule depends on the three factors: (i) the excess 'internal energy' left in the molecule, (ii) the core hole site and (iii) the final Auger-populated state of the molecule. The influence of these three factors on fragmentation of the core excited or ionized molecule is explored in this section.

Internal energy dependent fragmentation
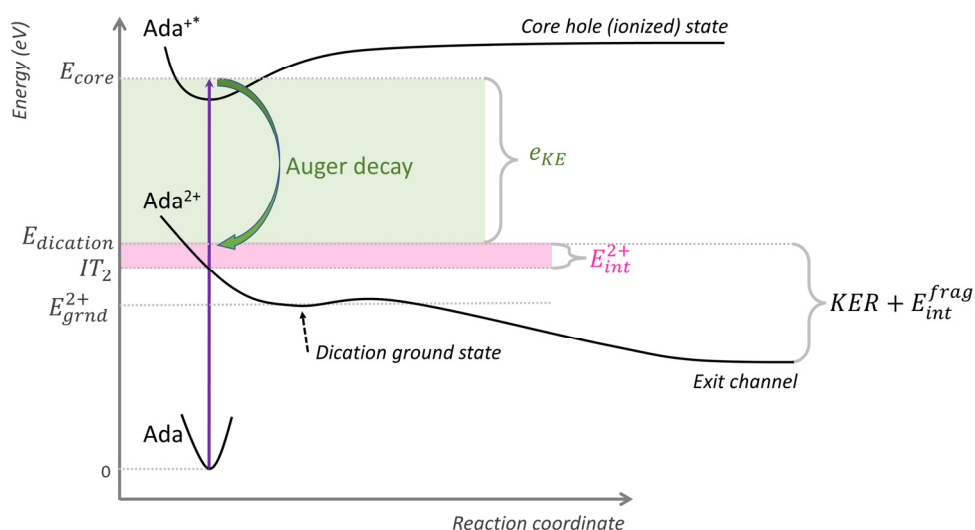
Figure. 2.3 Schematic showing potential energy curves involved in the electronic relaxation and fragmentation of core ionized adamantane dication displaying the different energy quantities involved, adapted from Maclot et al.[78]

Internal energy is the excess energy left in the molecule after Auger decay of the core ionized or excited state. The internal energy of the molecule can be classified into translational, potential, vibrational and rotational energy components. In Figure 2.3, we can see the potential energy curves of the fragmentation dynamics of a core ionized adamantane molecule, discussed in **Paper II**. The figure includes various energy quantities to help understand the process. Initially, adamantane is in its neutral ground state (Ada) and absorbs a photon of energy $h\nu$ (shown as a purple arrow). This causes vertical ionization in the Franck-Condon region, leading to the formation of the core hole ionized state with energy E_{core}. The core hole state then undergoes Auger decay and releases an Auger electron with kinetic energy e_{KE}, and

reaches the potential energy curve of the dication with energy $E_{dication}$. The internal energy (E_{int}^{2+}) of the dication is calculated with respect to the double valence ionization threshold (IT_2). For adamantane, the ground state of the dication has energy (E_{grnd}^{2+}) which is below IT_2. The internal energy of the dication state (E_{int}^{2+}) after core ionization can estimated from the Auger electron spectrum using the relation[79]

$$E_{int}^{2+} = E_{core} - IT_2 - e_{KE} \tag{2.6}$$

After fragmentation, the final ionic products have a total energy is equal to the sum of their internal energy (E_{int}^{frag}) and the kinetic energy released (KER). This total energy depends on the initial internal energy of the dication (E_{int}^{2+}) and the difference between the energy levels of IT_2 and the exit channel.

The excess internal energy in the molecule can be rapidly redistributed in the molecule among the various electronic and nuclear degrees of freedom available, then fragmentation of the molecule depends only on the amount of internal energy and leads to statistical fragmentation[80,81]. In this case, the core hole site or the final Auger-populated state does not influence the fragmentation of the molecule[81]. Typically for high internal energy states, the excess energy is rapidly redistributed and site-selectivity is lost like in $ClCH_2Br$ molecule[82].

Site-selective fragmentation – Core hole memory
Auger decay can preserve the memory of the core hole atomic site in a molecule and create two valence holes i.e., positive charges in the vicinity of the core hole site. Since, the Auger decay rate (see equation (2.3)) depends on the overlap of the core orbital with the valence orbitals involved in the decay, a localized Auger decay is likely to occur. If the excess internal energy is not redistributed, the localization of the charges leads to bond breaking near the core excitation or ionization site. Experimentally, the photon energy is tuned to selectively core excite or ionize a specific atomic site in the molecule to study *site-selective fragmentation*[75,79,83–87]. In this case, the memory of the core hole is retained during the ultrafast dynamics of the core excited or ionized molecule. Site-selective fragmentation of adamantane molecule is investigated in **Paper II** and **Paper III** after core ionization and excitation respectively.

State-specific fragmentation
The fragmentation of the molecule can also depend on the final electronic state reached after Auger decay rather than the core excitation or ionization site i.e., *state-specific*[88,89]. In this case, different electronic states with similar internal energy can still lead to distinct fragmentation patterns. The change in the distribution of charge among different electronic states causes differences in the bonding properties of the

molecule and results in different fragmentation patterns. For example, in core-ionized 5-Bromouracil, the dominant fragmentation channel involves bond breaking of atoms that are not in the vicinity of core ionization site[90].

2.4 Fragmentation of multiply charged molecular clusters

Molecular clusters are groups of molecules that are held together by weak intermolecular forces, such as van der Waals forces or hydrogen bonding. These clusters consist of a few molecules to hundreds of molecules. Due to presence of intermolecular interaction in the molecular clusters, core excitation or ionization results in different fragmentation dynamics compared to the free molecules discussed in previous section. Multiply charged molecular clusters mainly undergo fission due to Coulomb repulsion and produce singly charged small cluster fragments[91]. This is expected because the covalent bonds in the molecule are stronger than the weak forces that bind the molecules together in the cluster. In Paper I, however, the core ionized CO_2 cluster dication undergoes rearrangements to form new covalent bonds before fragmentation, in competition with the fission reaction.

The fragmentation of multiply charged molecular clusters after Auger decay depends on many properties like the cluster size and structure, charge localization, the excess internal energy left in the cluster and the chemical environment in the cluster. The effect of the cluster size, structure, and charge localization on the fragmentation of van der Waals clusters like CO_2 clusters is studied in this thesis.

Size and structure of clusters
Multiply charged van der Waals clusters are intrinsically unstable below a certain *critical size* and spontaneously undergo Coulomb explosion[92]. The mutual Coulomb repulsion between charges in a cluster is limited by the size of the cluster. When the cluster reaches a critical size, the charges can separate to a distance where the cluster remains intact and does not undergo fission. Classically, the critical size can be estimated using the Rayleigh's stability barrier predicts based on the cluster radius, surface tension, permittivity, and number of charges[93]. The critical cluster size of molecular clusters is commonly measured experimentally using mass spectroscopy[94]. Below the critical size, the fragmentation mechanisms of the clusters also on the structure of the cluster[95].

Charge localization in a cluster – Intracluster collisions
In a cluster, we core excite or ionize a single molecule which can undergo the Auger decay and emit an electron, with no interference from the neighbouring molecules.

Such a '*localized Auger decay*' is shown in Fig. 2.4 (a) and it creates localized charges in a single molecule of the cluster, which can dissociate via different intramolecular mechanisms. The fragment ions produced in the cluster can undergo further collision reactions with the neighbouring molecules in the cluster. Such intracluster ion-neutral collision have been studied before for benzene[96,97], ethylene, and acetylene[98] clusters. In this thesis, a simple classical model is developed to simulate such intracluster collision reactions in CO_2 clusters.

Energy transfer in a cluster – ICD
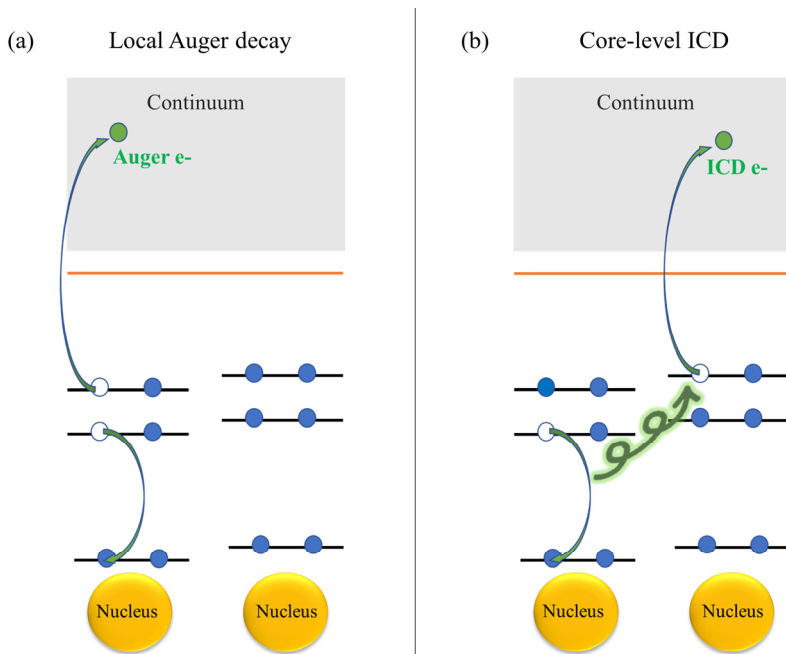
Figure. 2.4 Two possible electronic relaxation mechanisms in core ionized clusters. Local Auger decay is depicted in (a), where the core hole is filled by a valence electron, and another valence electron is emitted from the same atom. Alternatively the cluster can undergo core-level ICD shown in (b), where a valence electron from the same atom fills the core vacancy, releasing energy that is transferred to a neighboring atom, ultimately leading to its ionization. The figure is adapted from Hans et al.[99]

Alternatively, instead of localized Auger decay, the electronic relaxation of core excited or ionized molecule in the cluster can involve energy or electron transfer to a neighbouring molecule. An example of such an electronic relaxation process is Intermolecular Coulombic decay (ICD)[61] shown in Fig. 2.4 (b), in which a valence electron from the excited molecule fills the core hole, the excess energy is transferred to the neighboring molecule which emits a valence electron with small kinetic energy. After ICD both molecules in the cluster involved become singly charged and undergo Coulomb explosion. ICD is favourable because the energy

needed to singly ionize two molecules is less than the energy required to double ionize a single molecule. Consequently, ICD results in a lower final electronic energy overall. ICD has been observed in numerous molecular clusters[100–102] including CO_2 clusters[103].

3 Experimental Methods

In this chapter, we provide an in-depth overview of the experimental methods used in this thesis. The main purpose of this chapter is to give a clear understanding of the experimental setup and procedures that were followed to collect the data presented in the Results chapter. The chapter is divided into several sections. The first section explains synchrotron radiation, which is the light source used to induce the ultrafast dynamics in molecules and clusters. The second section describes Electron-ion coincidence spectroscopy, which is a powerful tool for studying the ionization and fragmentation dynamics using coincidence detection of charged particles. The third section focuses on 3D Momentum imaging technique, which provides detailed information about the momentum and kinetic energy of ions. Finally, the fourth section covers the sources of molecular and cluster beams, including the production and manipulation of these beams for experimental measurements.

3.1 Synchrotron radiation

The fundamental theoretical principles of radiation emitted by relativistic charged particles in circular motion can be traced back to the work of Liénard[104] in 1898. This radiation was first observed[105] and experimentally studied at a General Electric synchrotron in 1947. This discovery led a few decades later to the emergence of many X-ray based spectroscopic techniques to study of core excited systems. The main advantage of synchrotron radiation sources is the high photon energy resolution and tunability. At a synchrotron radiation facility, the three main components are the linear accelerator (LINAC), the storage ring and the beamlines. Free electrons emitted from a cathode are first accelerated to very high kinetic energies of few GeV, these electrons are then injected into a storage ring in the form of electron pulses or *bunches*. The spacing between these bunches are reflected in the temporal profile of the emitted radiation.

In the storage ring, strong magnets are used to bend the electrons and circulate them in a ring. Insertion devices called undulators generate a static magnetic field using arrangement of dipole magnets. The undulators change the electron trajectories into sinusoidal oscillations. The fundamental wavelength of the emitted X-rays depends on the undulator properties mainly the magnetic field. The wavelength can be tuned by changing the magnetic field of the undulator. As the electrons turn in the ring

they decelerate by emitting X-rays along the propagation direction of the electrons. The lost energy of the electrons is replenished by using synchronized radio-frequency (RF) fields in the storage ring. At the beamlines, the X-rays generated in the storage ring are optimized for specific experiments using optics. The synchrotron radiation beam can be further focused, monochromatized, chopped[106] to suit the demands of the research.

To create core-excited or ionized molecular systems high energy photons are required. The atomic number dependence of core shell absorption edges is shown in Fig 3.1. The core shell absorption edges[107] of small atoms ($Z < 20$) lie in the soft X-ray energy range of 0.1 to 5 keV. Therefore, to study the ultrafast dynamics of core ionized molecules and clusters versatile soft X-ray sources are essential. In this thesis, soft X-rays from synchrotrons was used to study fundamental light-matter interactions in carbon containing molecules and clusters.
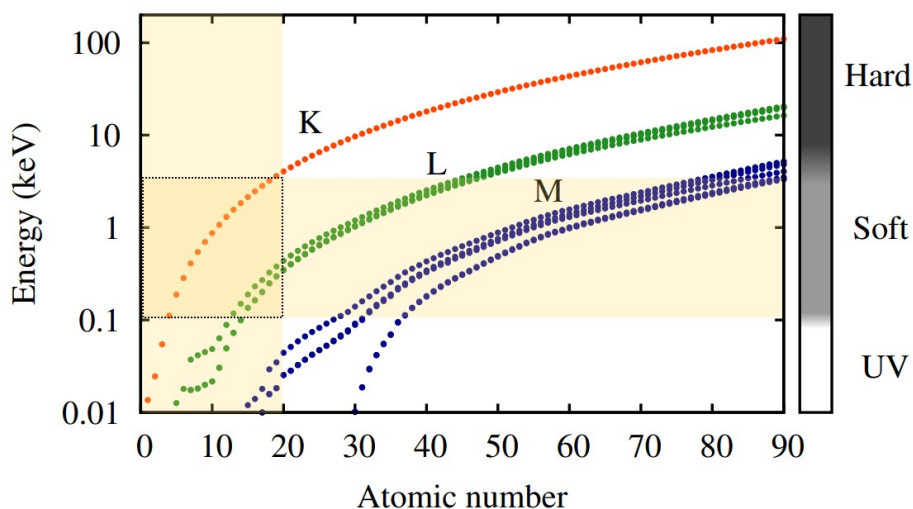
Figure 3.1 The K, L and M core shell X-ray absorption edges of elements as a function of atomic number adapted from Marra[108]. The region of core-shell abosrption for light atoms with atomic number less than 20 corresponds to soft X-ray absorption, is the interest of this thesis and is highlighted in yellow square.

The experiments reported in Paper I have been performed in MAX-Lab synchrotron at the I411 beamline[109], those in Paper II and III have been performed in SOLEIL synchrotron at the PLEIADES[110] beamline and those in Paper IV have been performed in MAX IV Laboratory synchrotron at the FlexPES beamline. The high photon energy resolution (few meV) and monochromaticity of synchrotron radiation has been used for atomic site-selective core excitation/ionization in molecules and clusters.

3.2 Electron-ion coincidence spectroscopy

Coincidence methods[111–113] are essential for complete characterization of physical processes that produce multiple particles, like fragmentation of photoionized molecules and clusters. When a molecular gas target interacts with soft X-rays, each absorption of a soft X-ray photon by a molecule is labelled as an ionization *event*, that inherently produces at least one ion and one electron. As the core-ionized state of the molecule evolves with time, the molecule can eventually emit more particles like electrons, ions, neutral fragments, or photons. Ultrafast dynamics upon ionization can be studied by measuring the physical properties of these final products. Coincidence spectroscopy uses temporal correlation between the final products to distinguish between particles produced in independent events. There are many distinct coincidence experiments possible like Photoelectron-Auger electron coincidence[114], Photoelectron-ICD electron coincidence[102], Photoelectron-Photoion coincidence[115] and Auger electron-Photoion coincidence[116].

Electron-ion coincidence spectroscopy can combine two powerful techniques: high-resolution electron spectroscopy and ion mass spectroscopy. Conventionally, electron spectroscopy is used to probe the dynamics in the femtosecond time scale and ion mass spectroscopy is used for much longer time scales (ps to µs). But electron and nuclear motion in excited molecules and clusters do not evolve independently so electron-ion coincidence spectroscopy is necessary to study the coupled dynamics. Fig. 3.2 shows the principle of an experiment when a photoionized molecule emits multiple electrons and produces ion fragments. The volume in space where the sample beam interacts with the photon beam is referred to as the *interaction volume*. To increase the collection efficiency of the ions and electrons, typically ions and electrons are steered in opposite directions using two independent analyzers with electromagnetic fields. The fields in the spectrometer are designed such that physical properties like the mass, charge, kinetic energy, or emission angle of the particles are dispersed temporally and/or spatially on the detectors of the analyzers. The ions and electrons detected within a certain time window are labelled as particles detected *in coincidence*.

Detectors and acquisition electronics

The charged particles are detected using a Micro-Channel Plate[117] (MCP) in combination with a position sensitive detector (PSD) like Delay-Line Detector[118] (DLD) or hexagonal-delay line detector[118] (HEX). When an electron or ion hits a microscopic channel on the MCP surface, an electron avalanche is initiated which create an electron cloud close to the original hit position. As the electron cloud travels away from the MCP surface towards the PSD, an amplified electronic signal is generated by the MCP due to electron depletion. This signal marks the START of the detected event. The electron cloud is then mostly absorbed by the PSD delay line wires. The delay line wires generate pulses that travel in opposite directions and

the difference in the propagation time of these pulses depends on the impact position. The DLD with two perpendicular delay line wire stacks has spatial resolution of tens of micrometres but cannot measure two impacts close to each other within a short time delay, this time delay is referred to as dead-time usually 10-20 ns. The HEX uses three delay line wire stacks that are rotated by 120˚ and allows for detection of few particles without dead-time.
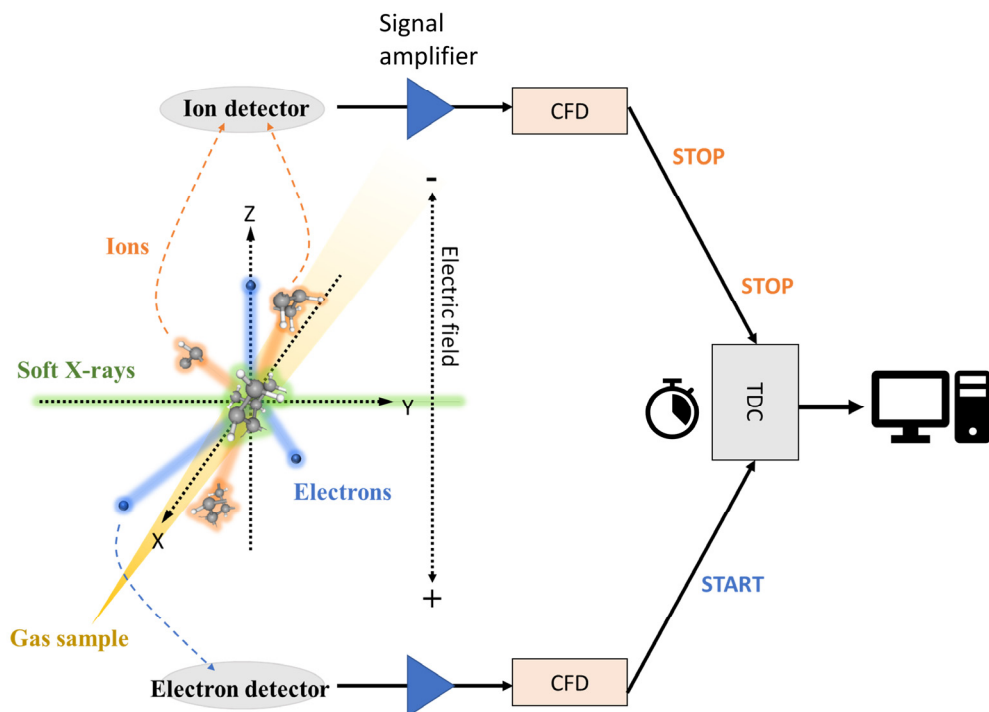
Figure 3.2 The principle of electron-ion coincidence experiments with a data acquisition flowchart. A cross-beam configuration of synchrotron beam with gas phase sample is used in an ultrahigh vacuum chamber. The molecules or clusters in the gas sample are ionized and the resulting electrons and ions are directed using electric fields in the spectrometer towards the respective detectors. The detector signals are supplied to a time-to-digital converter (TDC) card via electronics for amplication and thresholding of the signals. The coincidence of the electrons and ions is calculated by the TDC card, which is connected to the acquisition software in the PC.

The analogue time signals from the MCP and PSD are then amplified and converted to digital signals. The digital conversion can be done using a constant fraction discriminator (CFD) which converts analogue signals of varying amplitudes to digital signals (NIM standard -0.8V). The digital time signals give the time at which the amplitude of the signal reaches a fixed fraction of the maximum amplitude. These signals are then passed through a time-to-digital (TDC) converter that determines the time interval between two signals into digital signal. Typically, the

first particle that reaches the detector acts as a START signal for the TDC and the second particle acts as STOP signal. For electron-ion-ion coincidence experiments, the TDC should be capable of capable to registering multiple STOP signals after a single START. After the last STOP signal, the TDC has a certain latency after which it is RESET and waits for the next START signal.

Note that in our case for the HEX detector, after signal amplification the analogue signal is passed through a fast analogue-to-digital converter (fast ADC) which preserves the peak structure in the digital signal to be analyzed later by peak recognition software. The digital signal from the TDC or fast ADC are then further analyzed by the acquisition software which calculates the (X, Y) impact position of the particles (ions or electrons). The difference between the signal arrival times of the START and the STOP signal is used to calculate the absolute arrival time stamp i.e. time-of-flight (TOF) of the particles.

Criteria for a good coincidence experiment

During the measurement event, there is always a finite probability of measuring ions that do not originate from the same ionization event as the electrons. Such a coincidence event is labelled as a *false* coincidence. Another possible event is when all the ions produced in the ionization event were not measured, such an event is labelled as *aborted* coincidence. Aborted coincidences are still true coincidences and can be used to find information about the ions not measured. For a good coincidence measurement where the number of *true* coincidences are optimized, Eland at al.[113] suggested the following criteria:

1. The part of the interaction volume that the electron and ion analyzers are sensitive to should be the same.

2. The coincidence time window, the time interval after the START trigger for which the TDC card does not recognize a new electron hit should be kept as small as possible.

3. The collection, transmission and detection efficiency of both analyzers should be large.

4. The ion and electron count rates should be adjusted to minimize the *false* coincidences.

In a coincidence experiment, if more than one molecule is ionized within the acquisition time window, it increases the probability of detecting false coincidences. The probability of ionizing k molecules in the interaction volume is given by a Poisson distribution,
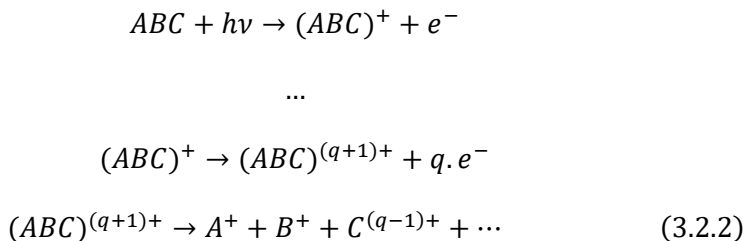
$$P(k) = \frac{rt^k e^{-rt}}{k!} \tag{3.2.1}$$

here t is the coincidence time window (typically 10 μs) and r is the ionization rate. To achieve $P(k = 2) < 0.01$; that is 99% of the time true coincidences can be detected, the ionization rate needs to be $r < 10^4$ Hz. The ionization rate depends on the density of molecules and photons in the interaction volume and ionization cross section at the chosen photon energy. As the ionization rate is also approximately the rate at which electrons are created in the interaction volume, it is usually optimized by keeping the electron count rate less than 10^4 Hz. For some experiments where the coincidence regime cannot be achieved, covariance mapping[119] can be used instead.

In this thesis, two types of electron-ion coincidence spectroscopy techniques are employed, Photoelectron-Photoion-Photoion coincidence (PEPIPICO) in Paper I and IV, and Auger electron-Photoion-Photoion coincidence (AEPIPICO) in Paper II and III.

3.2.1 PEPIPICO

Photo-electron Photo-ion photo-ion coincidence (PEPIPICO) spectroscopy was introduced by Frasinski et al.[120] and Eland et al.[121] in 1986 to study the fragmentation dynamics of dications. The general reaction studied using PEPIPICO is the fragmentation of a multiply charged species. After core-ionization, the molecule undergoes relaxation processes like Auger decay, auto-ionization or neutral fragment evaporation and forms a multiply charged mother ion. The mother ion then breaks into multiple fragment ions and neutrals. Using a spectrometer, the first electron emitted i.e., the photoelectron and the two ions are measured in triple coincidence. An example of such a process is given below.

$$ABC + hv \rightarrow (ABC)^+ + e^-$$

$$...$$

$$(ABC)^+ \rightarrow (ABC)^{(q+1)+} + q.e^-$$

$$(ABC)^{(q+1)+} \rightarrow A^+ + B^+ + C^{(q-1)+} + \cdots \qquad (3.2.2)$$

The spectrometer preferentially detects the light ions, and this may result in aborted coincidences. Therefore, while analyzing PEPIPICO data it is important to verify if the coincidence events are true and complete or true and incomplete (aborted).

In a PEPIPICO experiment, there are two possible START triggers for the TDC: a photoelectron trigger or an external trigger. If the photoelectron is used to set the time-zero for the ion TOF measurements then method is referred to as 'PE-trig PIPICO'[122] in this thesis. In this method, the photoelectron TOF cannot be measured

and therefore 3D momentum imaging of electrons is not possible. However, it is possible to measure the kinetic energy and emission angle of the photoelectron when PE-trig PIPICO method is combined with velocity-map imaging[123,124] or sophisticated energy analyzers[114,125]. In Paper I, the PE-trig PIPICO method is used with a high-resolution 3D momentum imaging ion spectrometer[126,127] to measure the fragmentation kinematics of core-ionized CO_2 clusters. X-ray photon energy of 320 eV was used for C 1s core ionization of the clusters, the photoelectron kinetic energy is expected to be about 20 eV. The photoelectrons were only used for event triggering and the photoelectrons were not energy analyzed. For complex quantum systems like clusters, interesting information about the fragmentation kinetics can obtained by PE-trig PIPICO method without any photoelectron energy analysis.

Alternatively, if an external trigger like a bunch marker from the synchrotron ring is used as the START trigger for the TDC then both electron and ion TOF can be measured with respect to this external trigger, this method is referred to as 'b-trig PEPIPICO' in this thesis. If the photoelectron energy or momentum is measured, it is possible to identify the atomic ionization site in the molecule[79] and study the angular correlation between photoelectron and ions[124,128]. In Paper IV, the development of a new *reaction microscope* (REMI) called ICE for 3D momentum imaging of electrons and ions using b-trig PEPIPICO method is described. The ICE end station is currently installed at the FlexPES beamtime of the 1.5 GeV synchrotron ring at MAX IV Laboratory. The bunch markers from the synchrotron ring are used for triggering the coincidence measurements.

3.2.2 AEPIPICO

Auger-electron photoion-photoion coincidence (AEPIPICO) spectroscopy is a useful technique that combines Auger electron spectroscopy with ion spectroscopy to study the ultrafast dynamics of core excited/ionized molecules. The lifetime of a K-shell (1s) core hole is a few femtoseconds[8,53], within which the atom/molecule spontaneously undergoes relaxation via Auger decay. The final state of the cation/dication after Auger decay depends on the Auger electron energy, therefore by measuring the Auger electrons in coincidence with the fragment ions we can correlate the different ionic states to the fragmentation pathways.

In an AEPIPICO experiment, there are two possible START triggers for the TDC: an Auger electron trigger or a random trigger. Due to the low collection efficiency of Auger electrons in the AEPIPICO technique, a random pulse generator is used for background measurement of false coincidences, which entails statistical filtering of the coincidence data. The AEPIPICO data of adamantane molecule discussed in Paper II and III was measured using the EPICEA (Étude de PhotoIons en Coincidence avec des Électrons Analysés) setup[116,129–132] at the PLEIADES beamline in Soleil Synchrotron. EPICEA can measure the 2D in plane momentum of Auger electrons and 3D momentum of ions in coincidence.

3.3 3D Momentum imaging spectrometers

Complete kinematic information about the dynamics of core-excited or ionized molecules or clusters can be obtained by 3D momentum imaging of the electrons and ionic fragments in combination with coincidence measurements. In a conventional time-of-flight (TOF) spectrometer, the initial position of the ions would affect the TOF of ions, resulting in different TOF for ions with same mass-to-charge (m/q) ratio. When a gas target like cluster or molecular beam is used there is an uncertainty in the position where the ions are created in the interaction volume.
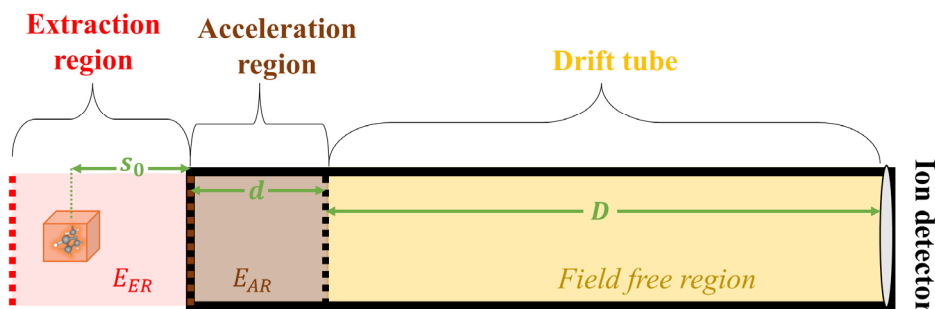
Figure 3.3 Basic geometry of a two-field spectrometer for measuring ion TOF.

Wiley and McLaren designed a two-field spectrometer to minimize the TOF dependence on the initial position of the ions[133]. Consider a two-field spectrometer as shown Fig. 3.3 with fields: extraction field E_{ER} and acceleration field E_{AR}. After the acceleration the ions travel along the field-free drift tube towards the ion detector. The initial position of ions (s_0) is approximated as the distance between the center of the interaction volume (the orange cube) and the entrance to the acceleration region. The length of the acceleration region and the drift tube are d and D respectively. Ideally the ion TOF should be independent of s_0. The *Wiley-McLaren condition* is calculated using the boundary condition $\frac{\delta TOF}{\delta s_0} = 0$, and gives the relationship between the distances in the spectrometer and the applied electric fields. The condition is written as

$$D = 2s_0(k_0)^{\frac{3}{2}}\left(1 - \frac{1}{k_0 + \sqrt{k_0}} \cdot \frac{d}{s_0}\right), \tag{3.3.1}$$

where $k_0 = \frac{s_0 \cdot E_{ER} + d \cdot E_{AR}}{s_0 \cdot E_{ER}}$. This time focusing condition is valid for ions with any kinetic energy. When the Wiley-McLaren condition is used in a spectrometer, the measured TOF depends only on the m/q value and the axial momentum along the spectrometer axis (z axis) of the ions.

3.3.1   3D momentum imaging of ions

During an experiment, with respect to the fixed laboratory frame the *molecular frame* is unique and different for each ionization event and depends on the location of the ionization and fragmentation in space. The reference frames of an ionization event in the interaction volume are shown in Fig. 3.4 (a), as the molecules are in motions in a gas sample the molecular frame is a moving frame. For the case of a molecular or cluster beam the velocity of the molecular frame is defined by the average beam velocity (v_{MB}).
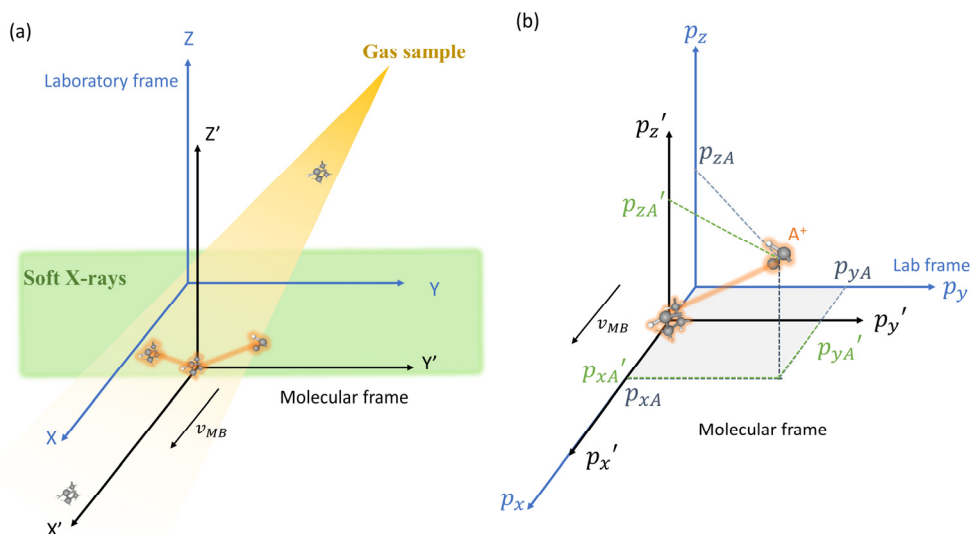
Figure 3.4 The frames of reference relevant to 3D momentum imaging experiment of ions. (a) The ionization and fragmentation of a molecule in the gas sample is shown in the laboratory and molecular frames of reference in Cartesian coordinates. The molecular frame is travelling at a velocity of v_{MB} and the laboratory frame is fixed in space. (b) The fragmentation of an ionized molecule into ion A^+ in the moving molecular frame and the fixed laboratory frame in 3D momentum coordinates.

The basic idea of 3D momentum imaging technique is to calculate the initial momentum vector (p_x', p_y', p_z') of the ions in the molecular frame, by measuring the momentum vector (p_x, p_y, p_z) of the ions in the laboratory frame. These momentum vectors of the ions are visualized in Fig 3.4 (b) before they are accelerated through the spectrometer. The transverse momentum (p_x, p_y) in the laboratory frame is projected on the 2D surface of the position sensitive detector and the axial momentum (p_z) is reflected in the time-of-flight (TOF) of the ions. The Wiley-McLaren condition ensures that the measured momentum $p_z = p_z'$. Therefore, it is possible to measure the axial momentum (p_z') of the ions in the molecular frame regardless of the position along z in the interaction volume. With

the introduction of position sensitive detectors, spectrometers were developed to also measure the transverse momentum (p_x', p_y') of the ions[122,134]. From the 3D momentum imaging data, we can also calculate the kinetic energy of the ions and the total ion kinetic energy released (KER) in an ionization event.

The schematic of the spectrometer used for 3D momentum imaging of ions in Paper I is shown in Fig. 3.5. The spectrometer (like Fig. 3.3) consists of three regions: the extraction region, the acceleration region, and the drift region. Clusters are produced by adiabatic expansion using a conical nozzle, and the cluster beam intersects the X-ray beam in the extraction region. Two grids are used in the extraction region to drive the ions towards the ion detector: the first grid called the pusher (shown in red) is kept at a high positive potential and second grid (shown in brown) is grounded to create a net potential ($V_{ext} \sim 400 \, V cm^{-1}$) that extracts the ions. The applied potentials and the design of the spectrometer satisfies the Wiley-McLaren condition. The photoelectrons are repelled by the grounded grid and are attracted towards the ion pusher, driving them to travel towards the electron MCP detector. Here, only the detection time of the electron is obtained, and electron energy is not analyzed. The detection of a photoelectron acts as the trigger for a PEPIPICO measurement.

After the extraction, the ions are accelerated using 17 evenly spaced electrodes interconnected by 1 MΩ resistors. The accelerated ions are then focussed using electrostatic lens to fine tune the ion trajectories. After this the ions enter the field free drift tube where they are separated in time according to their mass-to-charge ratio. At the end of the drift tube, the ions hit the MCP coupled with a position sensitive detector (Roentdek DLD-80). The measured TOF, X and Y positions on the detector are converted to the 3D momentum vectors of the ions. The data conversion is described in detail in the next chapter.

The spectrometer is designed to optimize the TOF and momentum resolution of the ions by maintaining 4π collection efficiency. If very high fields are used in the extraction region, heavier and faster ions can be measured but the high fields also reduce the momentum resolution.
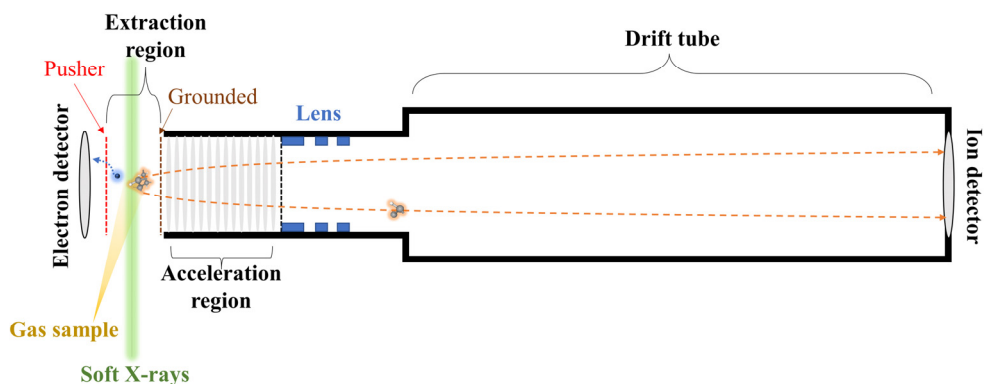
Figure 3.5 The schematic of the 3D momentum ion imaging spectrometer adapted from ref[126] used for e-trig PEPIPICO measurements in Paper I. The spectrometer consists of three main regions: extraction, acceleration and the drift regions. Electrostatic lenses are used for focussing the ion trajectories on the detector.

3.3.2   Momentum imaging of electrons and ions

In analogy to the ions, the 3D momentum of the electrons can also be obtained in the molecular frame using electromagnetic fields. In this thesis, three different detection schemes have been used for 3D momentum imaging of ions in coincidence with electrons. The ICE end station (Paper IV) at MAX IV Laboratory was used in high field mode with electrostatic lenses to measure low energy electrons with kinetic energy less than 15 eV. A combination of electric and magnetic fields was applied to record higher energy electrons with kinetic energy less than 100 eV using the ICE end station. The REaction MIcroscope (REMI) mode of operation is also referred to as COLd Target Recoil Ion Momentum Spectroscopy (COLTRIMS). Auger electrons with kinetic energy more than 100 eV were recorded using Double Toroidal Analyzer (TDA) of the EPICEA endstation[131] at SOLEIL Synchrotron. In addition to these detection schemes, Velocity-map imaging (VMI)[123] is also commonly used for 2D momentum imaging of electrons and ions using strong electric fields, and requires Abel transformation to obtain 3D momentum image.

3.3.3 ICE end station for PEPIPICO spectroscopy

The Ions in Coincidence with Electrons (ICE) end station is installed at the FlexPES beamline in MAX IV laboratory. The ICE spectrometer consists of 150 copper electrode plates (rings) mounted 5 mm apart and connected via 1 MΩ resistors except for the lens electrodes (C, D, E and F in Fig. 3.6 and Fig. 3.7) which have four ultra-high vacuum feedthroughs to change the electrostatic fields for switching between the two operational modes of electrostatic lensing and REMI without breaking the vacuum. The electron side of the spectrometer has 55 plates while the ion side has 94 plates. The total length of the spectrometer is 800 mm. Fine meshes are used at the end of the electron and ion side with external feedthrough to create a uniform electrostatic field along the spectrometer axis. MCPs with hexagonal delay-line detectors (HEX 100-75 RoentDek) are mounted after the meshes to detect the ions and electrons. The spectrometer is kept under high vacuum of the order of 10^{-8} mbar.

High-field mode with electrostatic lensing
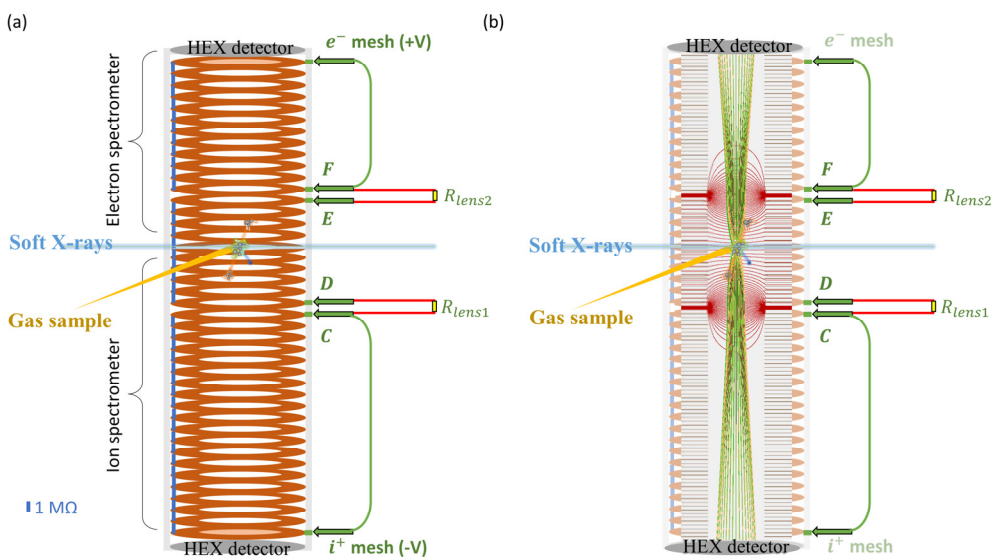
Figure. 3.6 The schematic of the High-field mode configuration of the ICE spectrometer described in detail in Paper IV. (a) The electronic connections used in this mode to achieve the lensing effect in the ion and electron side of the spectrometer. (b) The simulated electric fields (in red) in the spectrometer using SIMION software at electron lens voltage of 2028 V and ion lens voltage of 2184 V and the electric field in the interaction region is 110 V/cm. The simulated particle trajectories of protons with maximum kinetic energy of 10 eV and electrons with maximum kinetic energy of 15 eV are also shown in green lines.

The schematic of the high-field operation mode of ICE is shown in Fig. 3.6 (a). In this operation mode, the lens electrodes C and F are kept at the same potential as the ion and electron meshes respectively. The lens electrodes D and E are connected to C and F via suitable resistors R_{lens1} and R_{lens2} respectively, to get a potential difference between them. Due to the potential difference, electrostatic lenses are created between electrodes C and D in the ion side and the electrodes E and F in the electron side. No external magnetic fields are applied in the spectrometer in this mode. The simulated electric field lines of the electrostatic lenses in this operation mode are shown in Fig. 3.6 (b) in red lines, the lens electrodes D is kept at -2184 V and E is kept at +2028 V. The interaction volume is kept at constant electric field of ~ 100 V/cm.

The particles are accelerated from the interaction region due to the applied potentials. After extraction, the electrostatic lenses focus the particle trajectories spatially according to their initial momentum vectors. The region between electrodes C and ion mesh in the ion side and electrodes F and electron mesh are kept at the same potential and act as the drift region. In the drift region, the ion and electron trajectories are further separated spatially and temporally until they hit the respective detectors. Using the electrostatic lenses, 4π collection efficiency is obtained for ions with kinetic energy less than 10 eV and electrons with kinetic energy less than 15 eV. The simulated particle trajectories for protons with maximum kinetic energy of 10 eV and electrons with maximum kinetic energy of 15 eV are also shown in green in Fig. 3.6 (b).

The PEPIPICO measurements in ICE are triggered by the bunch markers from the synchrotron ring. The bunch marker sets the time zero of the coincidence event. When an electron hits the MCP, the electron TOF and X, Y positions on the HEX detector is recorded. When ions hit the MCP in the ion side of the spectrometer within the coincidence time window, then the ion TOF is calculated with respect to the bunch marker. The ion HEX detector also records the X, Y positions of the ion hit. The signals from the bunch marker, ion, and electron MCPs and HEX detectors are analyzed by the COBOLD PC data acquisition software[2].

The initial momentum vectors (p_x', p_y', p_z') of the ions and electrons in the molecular frame are calculated from the TOF and X, Y positions on the 2D surface of the HEX detectors. The electrostatic fields in this mode of the ICE spectrometer are optimized to keep the first electron TOF to be less than 10 ns, because the minimum bunch spacing of the synchrotron 1.5 GeV ring at MAX IV Laboratory is 10 ns.

---

[2] COBOLD PC software is available at https://www.roentdek.com/software/CoboldPC/

REMI mode with magnetic field

The REMI mode of operation combines a magnetic field with a weak electric field. The schematic of the REMI operation mode of ICE is shown in Fig. 3.7 (a). In this mode, lower electrostatic fields are used compared to the high-field mode, but Helmholtz coils are used to generate a uniform magnetic field in the spectrometer. The magnetic field is typically applied perpendicular to the plane of detection and is used to deflect the motion of electrons. In this mode the electrodes C and D on the ion side and the electrodes E and F on the electron side are connected via 1 MΩ resistors. External feedthroughs to the electron and ion meshes are used to create a linear electric field along the length of the spectrometer with no electrostatic lensing. This mode of operation is similar to COLTRIMS[135] spectroscopy which studies *cold targets*. The cold target is prepared by cooling the gas sample using supersonic expansion. This reduces the thermal motions of the molecules in the gas which deteriorates the momentum resolution of the ions.
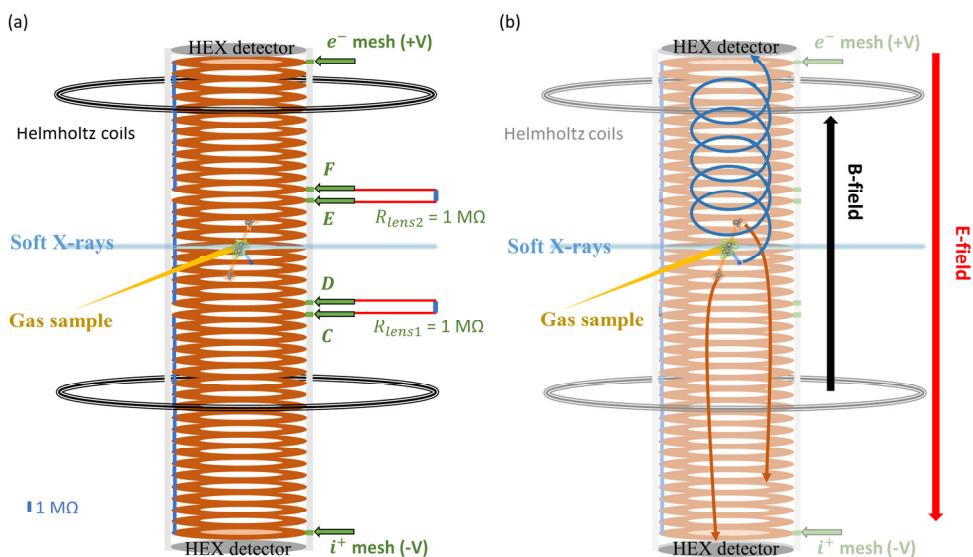
Figure. 3.7 The schematic of the REMI mode configuration of the ICE spectrometer described in detail in Paper IV. (a) The electronic connections are used in this mode to achieve a uniformly changing electric field along the ion and electron side of the spectrometer without any electrostatic lenses. An uniform magnetic field is also applied along the axis of the spectrometer using two Helmholtz coils. (b) The helical trajectory of the electrons (in blue) and approximated linear trajectory of the heavy ions (in orange) through the spectrometer in REMI mode.

The electron motion in the spectrometer depends on the applied electromagnetic fields and effective Lorentz force acting on the electron,

$$\vec{F} = q(\vec{E} + \vec{v} \times \vec{B}) \qquad (3.3.2)$$

Here $q = -e$ is the charge of the electron, $\vec{v}$ is the velocity of the electron, $\vec{E}$ and $\vec{B}$ are the applied electric and magnetic fields in the spectrometer. In ICE, both the electric and magnetic fields are applied along the spectrometer axis in negative z direction as shown in Fig 3.7 (b). Therefore, the applied fields are $\vec{E} = -E\hat{z}$ and $\vec{B} = B\hat{z}$. Now, the longitudinal force $(\vec{F_\parallel})$ parallel to the spectrometer axis and the transverse force $(\vec{F_\perp})$ perpendicular to the spectrometer axis are

$$\vec{F_\parallel} = eE\hat{z}$$

$$\vec{F_\perp} = -e(\vec{v_\perp} \times B\hat{z}) \tag{3.3.3}$$

here $\vec{v_\perp}$ is the velocity component of the electron perpendicular to the spectrometer axis. The change in momentum due to the Lorentz force components needs to be calculated to obtain the initial momentum vectors (p_x', p_y', p_z') of the electrons. The treatment for ion momentum calculation is like for the electrons but using the charge and mass of the ions.

The transverse motion of the electron exclusively depends on the magnetic field, resulting a circular path of the electron commonly referred to as cyclotron motion. The cyclotron frequency and period are calculated as

$$\omega = \frac{eB}{m}, T = \frac{2\pi m}{eB} \tag{3.3.4}$$

If a magnetic field of 10 Gauss is used, then the cyclotron period for an electron is 36 ns, whereas for a proton it is 65 μs. The number of turns in the spectrometer before the electron reaches the detector is the ratio between the electron TOF and the cyclotron period. For larger ions, the cyclotron period will much larger than the ion TOF and therefore for the larger ions only the longitudinal motion in the electric field can be considered.

The radius of the circular path is inversely proportional to the magnitude of the magnetic field and is given by

$$R = \frac{|\vec{p_\perp}|}{eB} \tag{3.3.5}$$

Therefore, by using strong magnetic fields the high kinetic energy electron trajectories can be spatially compressed to hit the detector surface. However, the transverse momentum resolution will be compromised if very strong fields are used.

The initial transverse momentum components of the electron or ions are calculated from the impact position (X, Y) on the HEX detectors. Given that magnetic field

$\vec{B} = B\hat{z}$ and the cyclotron frequency is rotating in anti-clockwise direction, the initial momentum components are calculated as[136],

$$p_x' = \frac{m\omega}{2}\left(X\cot\left(\frac{\omega \cdot TOF}{2}\right) - Y\right) \qquad (3.3.6)$$

$$p_y' = \frac{m\omega}{2}\left(Y\cot\left(\frac{\omega \cdot TOF}{2}\right) + X\right) \qquad (3.3.7)$$

The longitudinal motion of the electron depends only on the applied electric field, as in ICE-REMI a single homogeneous electric field is used. The initial longitudinal momentum p_z' is calculated from the measured electron TOF as

$$p_z' = e \cdot E \cdot \left(TOF_{p_{z'}=0} - TOF\right) \qquad (3.3.8)$$

Here $TOF_{\vec{p}=0}$ is the TOF of electrons with zero longitudinal momentum and the value of $TOF_{\vec{p}=0} = \sqrt{\frac{2md}{eE}}$. Here d is the length of the spectrometer on the electron side, for ICE we know that $d = 294\ mm$ and for the ion side $d = 497\ mm$. The resolution of the electron and ion TOF depends on magnitude of the electric field and higher resolution can be obtained by using lower electric fields. Due to the combination of the longitudinal linear motion and the transverse circular motion, the resultant electron ion trajectories are helical as shown in Fig. 3.7 (b). As the effect of the magnetic fields on the ions can be neglected, they have linear trajectories.

As the electrons follow this helical path because the cyclotron frequency is independent of the electron kinetic energy, electrons of all kinetic energies periodically align in the transverse plane at the *magnetic nodes* in the electron TOF. At these magnetic nodes, the transverse momentum of the electrons is ambiguous. Therefore, to resolve the transverse momentum of all electrons the fields in the spectrometer are adjusted such that TOF of most electrons falls between two adjacent magnetic nodes.

By combining the electromagnetic fields, REMI can measure higher energy electrons than electrostatic lensing. In the ICE-REMI mode, 4π collection efficiency of electrons with kinetic energy less than 40 eV and ions with kinetic energy less than 10 eV is obtained. The ICE-REMI can only be used during single-bunch delivery mode of the synchrotron ring because the electron TOF in this mode is more than 10 ns. Each single bunch marker acts as the START trigger for the PEPIPICO coincidence measurement, followed by the measurement of electron and ions TOF, X and Y positions on the detectors.

3.3.4 EPICEA end station for AEPIPICO spectroscopy
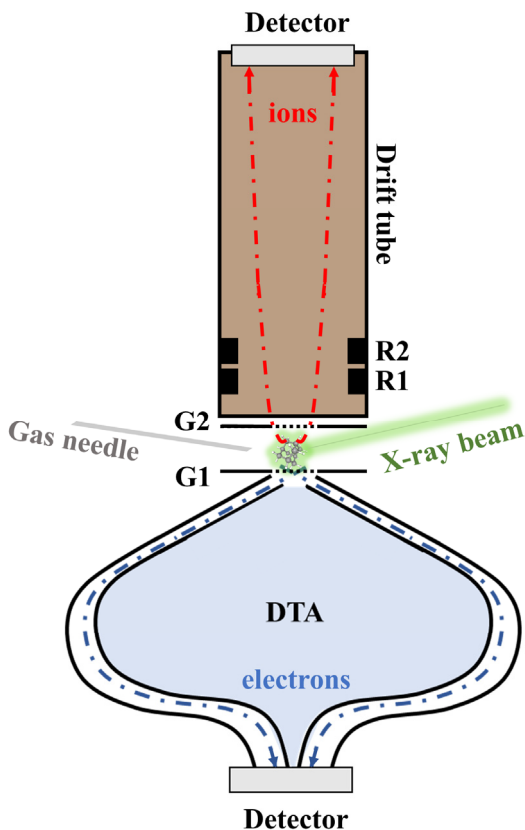
Figure. 3.7 The schematic of the EPICEA endstation used for AEPIPICO measurements in Paper II and III. The endstation consists of a double toroidal analyzer for high electron kinetic energies and an ion 3D momentum imaging spectrometer using electrostatic lenses. The sample is injected close to the interaction volume using a gas needle to produce an effusive beam. The effusive beam interacts with the synchrotron beam to produce electrons and ions.

The EPICEA setup couples a double toroidal analyzer (DTA)[130] with a 3D momentum imaging ion spectrometer; the schematic is shown in Fig 3.7. The sample is injected into the high vacuum through a heated gas needle with an inner diameter of 200 μm producing an effusive gas beam that is perpendicular to the X-ray beam. The interaction volume is placed in a zero-electric-field space between two extraction grids (G1 and G2). The DTA measures electrons emitted at the magic angle of 54.7° with respect to the horizontal polarization axis and it has a collection efficiency of 4.2% of 4π sr. During an experiment, first the pass energy (Ep) is selected in the energy window of the interested electrons. Electrons with kinetic

energy within 12% of Ep are measured with an energy resolution of 1% of Ep. For example, when a pass energy of 250 eV is used the electron energy resolution is about 2.5 eV and the detection range is 250±15 eV.

After entering the analyzer, the high energy electrons are collimated and retarded to the pass energy Ep using electrostatic lenses then they enter the region between the double toroidal deflector plates. These plates spatially disperse the electron trajectories according to their kinetic energies[137] and focus them on the plane of the delay-line position sensitive detector (DLD40, Roentdek GmbH). On the detector, the radius of the electron position is inversely proportional to its kinetic energy and the azimuthal angle on the plane of detector depends on the emission angle of the electron.

The detection of an electron by the DTA triggers a pulsed extraction field on G1 and G2 that accelerate all ions in the interaction volume towards the drift tube of the ion TOF spectrometer. At the entrance of the drift tube two focussing lenses R1 and R2 are installed for 3D focussing of the ions. At the end of the drift tube the ions are detected using a hexagonal delay-line detector (HEX75, Roentdek GmbH). For the ion TOF spectrometer the collection efficiency is 100% of 4π sr. The detector records ion TOF, the radius and the azimuthal angle on the plane of detector, which are used to calculate the 3D momentum of the ions in the molecular frame. These coincidence measurement events are categorized as electron-triggered events.

A *true* coincidence event measures ions and electrons in coincidence produced from the same photoionization event in the interaction region. Due to the low collection efficiency of electrons in EPICEA, most of the electrons created from the photoionization event are not measured. This results in many stray (background) ions in the interaction region, 'waiting' for an electron trigger to occur. When eventually an electron is measured, and the ion detector is triggered. The detector measures the true ions along with the stray ions from previous photoionization events. Such an event is called *false* coincidence event. Experimentally there is no way to distinguish between electron triggered *true* and *false* coincidence events. Using low ion count rates or using high voltage sweeping pulses we can reduce the contribution of false coincidences, but both the experimental methods have setbacks.

An alternative method is to measure ions without electron trigger using random triggers to the ion detector along with measuring the ions with electron triggers. This provides us with unique random background of ions not generated in same ionization event and specific to the experimental conditions. Therefore, in EPICEA a pulse generator is used to produce random triggers which act as a pseudo electron trigger and extracts all the ions in the interaction region. These measurement events are categorized as random-triggered events. The use of these events to remove false coincidences is discussed in detail in the next chapter.

As the electron energy resolution of the TDA in EPICEA is limited, the Resonant Auger electron spectrum (RAES) and Normal Auger electron spectrum (AES) of adamantane molecule was also recorded using VG-Scienta R4000 electron energy analyzer[125] which has a better electron energy resolution. The VG-Scienta R4000 is a hemispherical electron energy analyzer (HSA) with energy resolution of 150 meV at pass energy of 200 eV. The HSA is not used for coincidence measurements due its lower electron collection efficiency than the TDA in EPICEA. The RAES and AES spectrum shown in Papers II and III are recorded using the HSA and compared to coincidence data recorded using EPICEA.

The schematic of Auger electron spectroscopy experiment is shown in Fig. 3.9. The HSA consists of a wide-angle lens, several slit pairs and the hemispherical dispersive analyzer. The acceptance solid angle of the HSA depends on the lens and the size of the slits. After entering the HSA, the electrons are retarded to the preselected pass energy Ep using the lenses and slits to improve the energy resolution. In the hemispherical dispersive analyzer, the electron trajectories are spatially dispersed according to their kinetic energy and projected onto position sensitive detector[138].
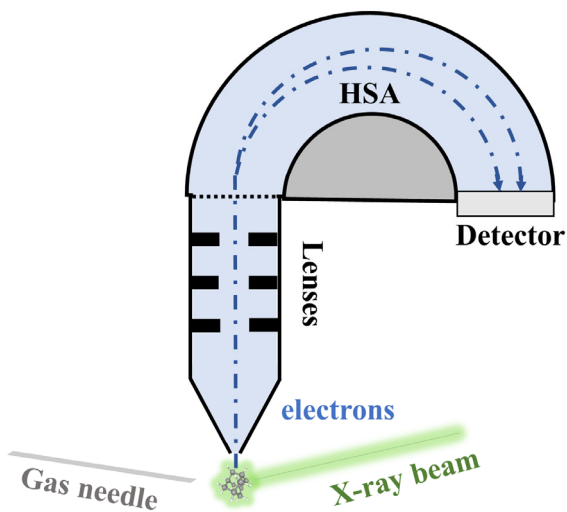

Figure. 3.9 The schematic of the VG-Scienta R4000 electron spectrometer used for Auger spectroscopy measurements in Papers II and III. The electron spectrometer consists of electrostatic lenses and a hemispherical analyzer and is suitable for measuring high energy electrons with superior energy resolution than EPICEA.

3.4 Molecular and cluster sources

In this thesis, the interaction of gas phase targets like molecules and clusters with soft X-rays is studied using 3D momentum imaging of ions and electrons in coincidence. The spectrometers discussed in this thesis are kept in ultra high vacuum pressures, therefore sample delivery into the chamber without disturbing the vacuum is a challenge. Gas phase targets are useful for studying the fundamental light-matter interactions as the molecules and clusters are isolated and the thermal motion can be controlled. Also, for coincidence experiments, the continuous flow of gas in the interaction volume ensures that the sample is continuously replenished, and each ionization event originates from a new molecule or cluster.

Conventionally in mass spectrometry experiments, a thin needle is used to supply the gas sample very close to the photon beam[139]. As a gas flows through the needle orifice into the vacuum chamber, an effusive gas jet is created which has high sample density. Ideally, for effusive flow[140,141] of gas, the number density along the needle should drop linearly with distance (x). For a gas flow rate of dN/dt from the gas reservoir to vacuum,

$$\frac{dN}{dt} = -K\frac{dN}{dx} \qquad (3.4.1)$$

Here K is a constant which depends on the cross-section area of the needle, gas temperature and velocity. The diameter D of the orifice is kept smaller than the mean free path λ_0 of the molecules in the gas reservoir at pressure P_0,

$$D \ll \lambda_0 \qquad (3.4.2)$$

As the gas flows through the orifice, no collisions occur between the molecules therefore the velocity and internal molecular states distribution of the effusive beam is identical to that in the reservoir and depends on the reservoir temperature. The gas jet formed in this way is divergent and the molecules in the jet are not 'cooled'. Therefore, effusive gas sources are not suitable for cold-target spectroscopy like COLTRIMS. Because of the effusive nature, the overlap between the gas beam and the photon beam forms a large interaction volume which reduces the resolution of the spectrometer. However, the convenience of being able to evaporate a solid or liquid sample and flowing it through a heated hypodermic needle into the vacuum chamber makes them still popular. Also, due to the high density of molecules in the interaction volume it is easier to obtain good statistics for coincidence measurements even if the collection efficiency of the spectrometer is not high. In Paper II and III, effusive jet of evaporated adamantane was used to achieve high sample density in the interaction volume.

In this section, a brief review of molecular and cluster beams source used for coincidence spectroscopy in this thesis are described.

3.4.1 Molecular beam by adiabatic expansion

Molecular beam is a steady stream of molecules that is typically produced by passing a gas or vapor through a small nozzle under high pressure conditions into ultra-high vacuum. The stream of molecules that emerges from the nozzle is typically characterized by its high directionality, high velocity, low temperature, and low density. To create a molecular beam, the reservoir or stagnation pressure (P_0) is increased to satisfy the condition[142],

$$D \gg \lambda_0 \tag{3.4.3}$$

As the gas flows through the nozzle orifice and downstream of the orifice the molecules in the gas undergo many collisions. Due to the collisions, the random motion of the molecules is converted to directed molecular flow[143] resulting in increased mass flow velocity. As there is no energy exchange with the surrounding this type of free jet flow is called *adiabatic expansion* through a nozzle. The Mach number M is the ratio of the mass flow velocity to the sound velocity. As the expansion evolves the Mach number increases to M > 1.3, i.e., supersonic flow is achieved. At large distances from the nozzle, as the temperature decreases, and the collision frequency decreases[144] there is a transition from continuum flow to *free molecular flow*. The velocity distribution of the molecular beam and the increase in M at larger distances is limited by this transition[145]. The isentropic region near the nozzle, where M > 1 is called *zone of silence* (ZOS)[146] and the flow here is unaffected by the surroundings. Beyond this region M < 1 and shock waves are created due interaction with the background molecules in the expansion chamber. The length of ZOS is related to the pressure difference between the gas reservoir and the expansion chamber (P_b) by the empirical relation[147],

$$L_{ZOS} = D.\frac{2}{3}\sqrt{\frac{P_0}{P_b}} \tag{3.4.4}$$

Monte Carlo simulations

The effect of nozzle geometry[148,149] on the flow of gas was simulated using direct simulation Monte Carlo program[150] developed by G. Bird[3]. Fig. 3.10 shows the number density of helium with backing pressure of 0.1 bar kept at room temperature expanding through a nozzle with diameter of 0.2 mm into perfect vacuum. The simulation is repeated for different nozzle opening angles of 180° sonic nozzle (a), 40° conical nozzle (b) and 70° conical nozzle (c). The simulation distance is 5 mm from the nozzle opening. For the simple sonic nozzle also known as a pinhole nozzle, the expansion of gas is not confined by the nozzle walls, which therefore results in rapid decrease in number density and cooling of the beam. By using a

---

[3] http://www.gab.com.au/

conical nozzle, the rapid fall in number density due to adiabatic expansion can be reduced and a larger working distance can be obtained.
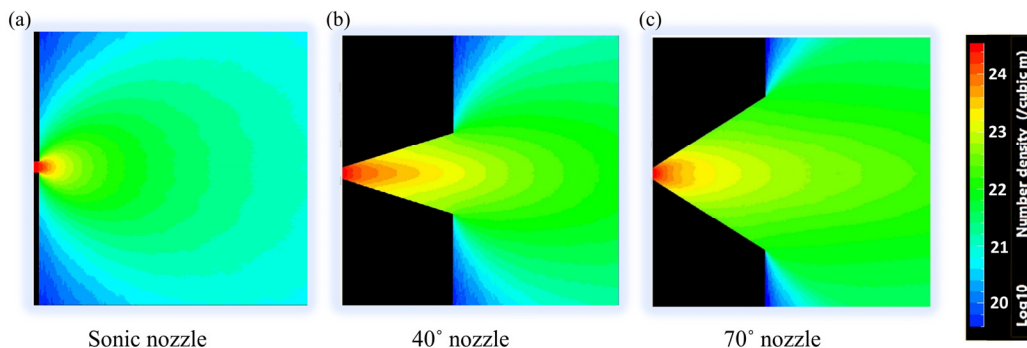
Figure. 3.10 Direct simulation Monte Carlo (DSMC) results for adiabatic expansion of helium gas with stagnation pressure of 0.1 bar at room temperature into perfect vacuum. The nozzle diameter is fixed at 0.2 mm and the nozzle opening angle is 180˚ sonic or pinhole nozzle in (a), 40˚ conical nozzle in (b) and 70˚ conical nozzle in (c). The number density of atoms is plotted in logarithmic colormap as a function of distance from the nozzle. The total simulated distance is 5 mm.
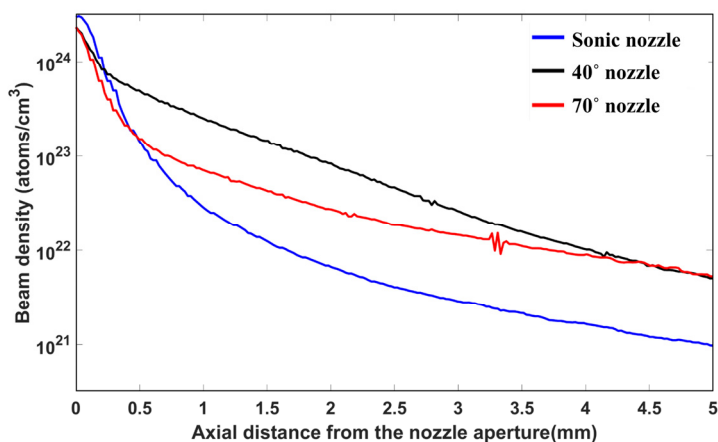
Figure. 3.11 Direct simulation Monte Carlo (DSMC) results of adiabatically expansing helium gas showing the decrease in beam number density as function of axial distance from the nozzle aperture for sonic nozzle, 40˚ and 70˚ conical nozzles. The simulation conditions are kept the same as in Fig 3.10.

For coincidence experiments, the interaction region must be kept at very high vacuum therefore the adiabatic expansion chamber is usually separated from the interaction region by using differential pumping and skimmers. Therefore, it is desirable to have high number density at larger distances from the nozzle to install

skimmers and still maintain enough density of the sample in the interaction region. Two opening angles of conical nozzles were tested, the fall of number density of the beam as a function of increasing distance is shown in Fig. 3.11. For the sonic nozzle the beam density falls rapidly with distance, for the 70° conical nozzle the density drop is more controlled, but the best results are obtained for the 40° conical nozzle. Therefore, for higher beam density the optimal opening angle for a conical nozzle is 40° and it produces densities higher by one order of magnitude compared to a pinhole sonic nozzle[151].

A typical molecular beam arrangement used for coincidence experiments is shown in Fig. 3.12. The gas from a high-pressure reservoir flows through a conical nozzle and undergoes adiabatic expansion. The other side of the nozzle is kept at lower pressure of about 10^{-5} bar. The first skimmer is kept at a distance of about 1000 nozzle diameters to avoid skimmer clogging[151] and within the zone of silence[152] to skim only the part of the beam which has laminar flow and lowest temperature. The second skimmer further reduces the beam dimensions and acts as pressure barrier between the interaction region and the molecular beam source. Conical skimmers with apertures 0.5-1 mm are used to reduce skimmer interference[153]. The alignment between the nozzle and skinner apertures is crucial to obtain a collimated molecular beam of adiabatically cooled molecules.
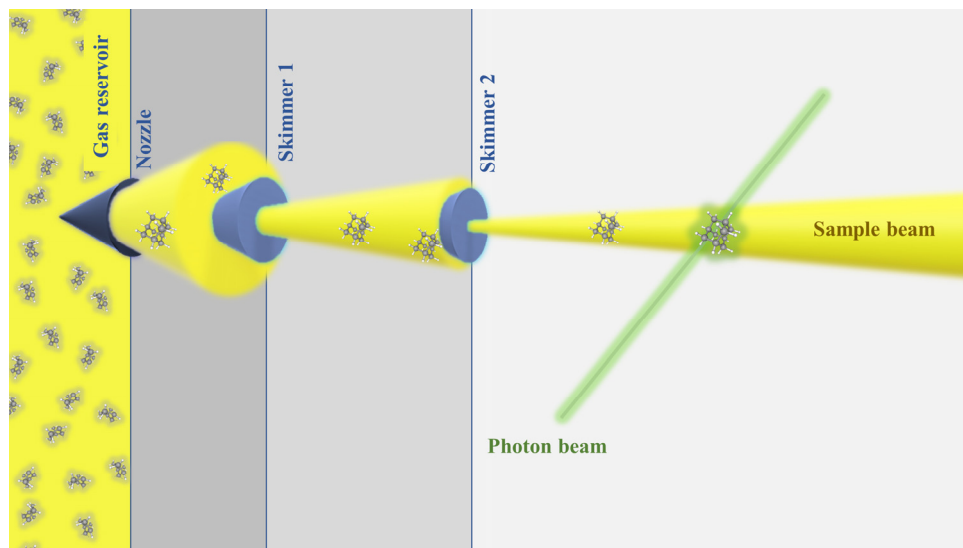
Figure. 3.12 A typical molecular beam source arrangement with a conical nozzle and two skimmers with differential pumping. The gas reservoir is kept at a high pressure to create a cooled molecular beam by adiabatic expansion through the nozzle. The distance between the frist skimmer and the nozzle is less than L_{zos} to extract the cooled and laminar flow part of the molecular beam. The final narrow skimmed sample beam interacts with the photon beam in the ultra-high vacuum chamber.

3.4.2 Cluster beam sources

Clusters are aggregates of a small number of atoms or molecules that are held together by weak intermolecular forces, such as van der Waals or hydrogen bonding. Clusters have different properties and reactivity than individual atoms or molecules, they can provide valuable insights into the behavior of materials at the nanoscale. Cluster beams can be produced from a variety of molecular sources, including gases, liquids, and solids. In gas-phase cluster beam experiments, a gas is typically adiabatically expanded through a small aperture or nozzle, producing a collimated beam of clusters. In contrast, in laser ablation experiments, a solid material is vaporized using a laser, producing a beam of clusters that can be analyzed using mass spectrometry or other techniques. The properties of the cluster beam, such as its size and composition, can be varied and controlled to study a wide range of phenomena, from chemical reactions to materials growth and properties.

The cooling process in the molecular beam decreases the internal energy of the molecules which can result in condensation into molecular clusters. The internal energy of the molecules must be cooled down to the order of sub eV (~0.1 eV), less than the binding energy of the cluster aggregates. As the cooling effect is maximum in the ZOS, clusters are mainly formed in this region. The molecules nucleate via three-body or multi-body collisions, the condensed molecules are held together via Van der Waals interactions or hydrogen bonding. The condensation process depends on the stagnation pressure, the nozzle geometry[154] and temperature, the skimmer temperature[155] and the properties of the molecular gas.

Due to the randomness of condensation via adiabatic expansion, the number of molecules in the cluster i.e., the cluster size is a broad distribution that can be described by a log-normal distribution. Hagena[156] proposed a scaling law to calculate the mean cluster size using classical theory of gases, but for very small clusters the classical scaling laws are not always valid and complex quantum chemical calculations can be required[26].

In Paper I, CO_2 clusters were produced by adiabatically expanding CO_2 gas through a small aperture conical nozzle. The estimated cluster size distribution as a function of the stagnation pressure is shown in Fig. 3.13. The mean cluster sizes are calculated using the empirical relation[157] shown in equation (3.4.5) for CO_2 clusters characterized by photoelectron spectroscopy.

$$N_{mean} = (99 \pm 10) \left(\frac{\Gamma *}{1000} \right)^{(2.23 \pm 0.15)} \tag{3.4.5}$$

Here, $\Gamma *$ is the Hagena's scaling parameter[156] for condensation of gases via adiabatic expansion.
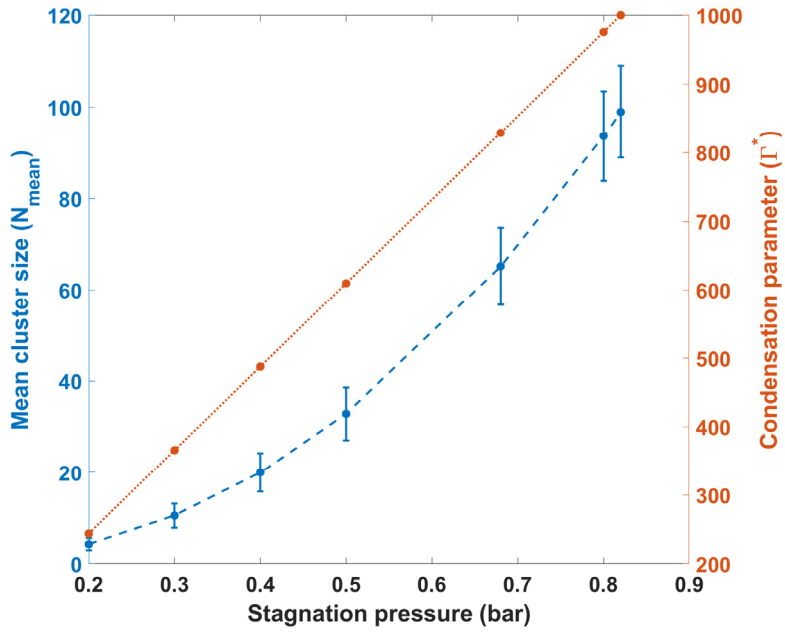
Figure. 3.13 The estimated mean cluster size N_{mean} and condensation parameter $\Gamma*$ of CO_2 clusters as a function of increasing stagnation pressures used in the experiments of Paper I.

4 Data Analysis

The acquisition of experimental data is just the beginning of the scientific process. The real challenge lies in analyzing and interpreting the data to extract meaningful insights and draw accurate conclusions. This is particularly true when sophisticated techniques such as 3D momentum imaging of ions, multiparticle coincidence spectroscopy and high-resolution electron spectroscopy are used to probe the ultrafast dynamics of small quantum systems. In this chapter, we will explore the process of data analysis for the different experimental techniques discussed in previous chapter. We will begin by discussing the general data treatment of ion data from Photoelectron-Photoion-Photoion Coincidence (PEPIPICO) experiment for 3D momentum imaging, followed by data correction and calibration procedure for Auger electron spectroscopy. Finally, we will address the issue of false coincidences that can arise in an Auger electron-Photoion-Photoion Coincidence (AEPIPICO) experiment and present methods for removing them from the data.

4.1 3D momentum imaging of ions

The raw experimental data of ions from a 3D momentum imaging spectrometer contains the (X, Y) positions on the PSD, the TOF in the spectrometer and the event time stamps that correlate the ions measured in coincidence. Fig. 4.1 shows the ion TOF of CO_2 clusters measured at 320 eV photon energy and the inset shows the ion detector image. To identify the ions the TOF is converted to mass-to-charge (m/q) ratios using the relation,

$$\frac{m}{q} = \left(\frac{TOF - b}{a}\right)^2 \tag{4.1.1}$$

Here a and b are constants depend on the fields in the spectrometer and that can be calculated by using reference ions in the TOF spectrum. In a simple ion mass spectrometer, with a single extraction field the constant $a = \sqrt{\frac{2d}{E_{ext}}}$ where d is the total distance travelled by the ion and E_{ext} is the electric field applied across the spectrometer i.e., the extraction field. The calculated m/q values of the ion fragments of CO_2 clusters are shown in the top axis of Fig. 4.1 and we can identify ions C^+, $O^+, CO^+, O_2^+, (CO_2)_n^+$ (n is the cluster size) and CO_2^{2+}.

The width of each TOF peaks of the ions depends on axial initial momentum p_z of the ions along the spectrometer axis, their charge q and the extraction field E_{ext}. From the ion TOF data we can calculate p_z as,

$$p_z = q \cdot E_{ext} \cdot \left(TOF_{\vec{p}=0} - TOF \right) \tag{4.1.2}$$

Here $TOF_{\vec{p}=0}$ is the time-of-flight of the ion if it has zero initial momentum. When the extraction field is increased the width of the peaks reduces and p_z resolution is decreased. In case of inhomogeneities of the electrostatic fields due to the lenses in the spectrometer or near the detector, the raw data are corrected before converting to 3D momentum following the correction procedure described in ref[158].
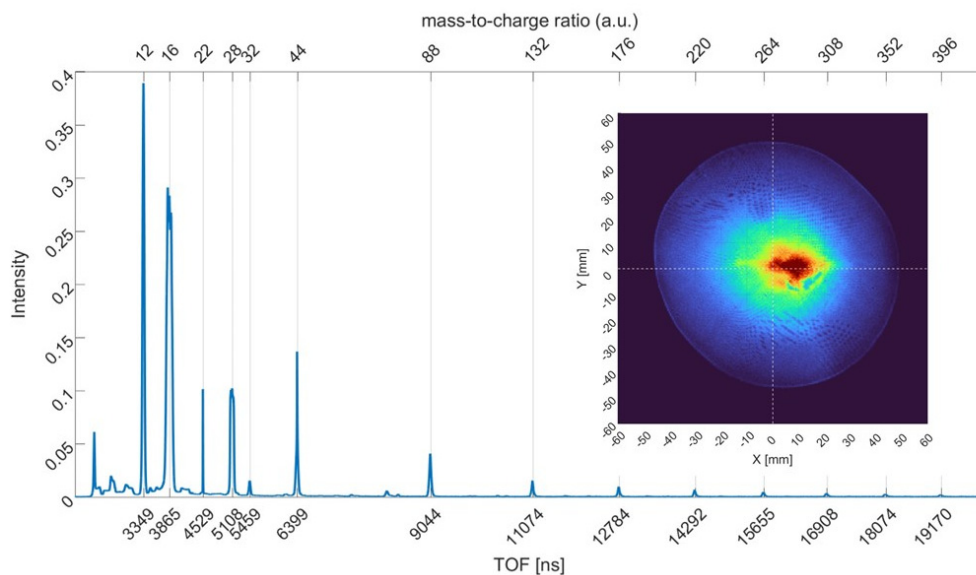
Figure. 4.1 The time-of-flight (TOF) spectrum of fragments ions produced by core-ionized CO_2 clusters of mean cluster size of about 20 molecules at photon energy of 320 eV. The TOF is converted to mass-to-charge ratio to identify the ions, these mass-to-charge ratios are shown on top axis. The inset shows the 2D detector image of the ions recorded under same conditions as the TOF.

The measured position on the detector depends on the initial transverse momentum (p_x, p_y) of the ions in the laboratory frame. If the transverse axis of the laboratory frame is not aligned with the detector center, then the detector positions (X, Y) of all ions must be translated by (dX, dY) to the detector center. Additionally, if the cluster/molecular beam has high velocity, in the laboratory frame the mother ion before fragmentation is travelling in the direction of the beam. Therefore, the fragment ions will also gain momentum in the direction of the molecular beam. The relation between the molecular ($p'_{x,y,z}$) and lab frame ($p_{x,y,z}$) vectors are,

$$p_{x,y,z} = p'_{x,y,z} + m \cdot v_{MB}(x,y,z) \qquad (4.1.3)$$

Here m is the mass of the ion and v_{MB} is the velocity of the molecular beam. Therefore, the effect of the moving molecular frame will be more pronounced for heavy ions. Fig. 4.2 (a) shows the raw experimental data of X vs TOF, the straight lines appearing at different TOF positions are different ion species. We observe that for the larger TOF i.e., the heavy ions the distribution in X is not centered around X = 0 and is shifted towards the positive X-direction, here the direction of the cluster beam is along the X axis. As we are only interested in the momentum component of the ions that is inherited from the fragmentation reaction i.e. (p_x', p_y'), the momentum component from the cluster beam is subtracted from the measured laboratory frame vectors using the relation,

$$X = X_{measured} - v_{MB}(x) \cdot TOF \qquad (4.1.4)$$
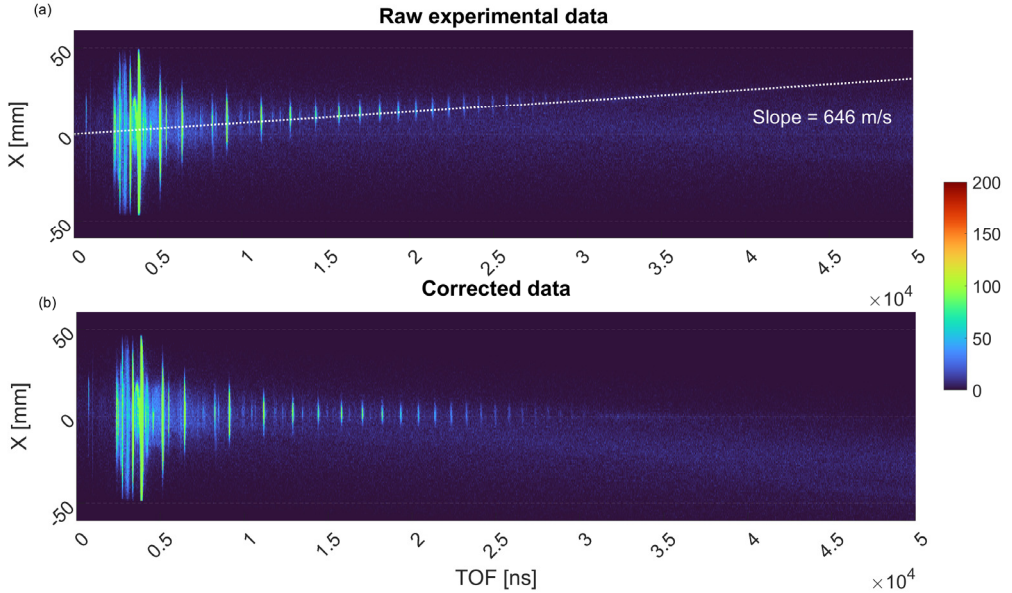
Figure. 4.2 The effect of molecular beam velocity on the measured X positions on the ion detector as a function of TOF. The ions are produced by core-ionized CO_2 clusters of mean cluster size of about 20 molecules at photon energy of 320 eV. (a) The raw experimental data showing the shift in X positions of the ion detector images for ions with increasing TOF. The center of the X distributions for the ions as a function of TOF are fitted to a linear of the form X = Slope.TOF, here the slope is the velocity of the molecular beam. (a) the corrected data after subtracting the shift due to the molecular beam velocity.

The value of $v_{MB}(x)$ is found be fitting the center of $X_{measured}$ distribution for each ion TOF, the slope of the linear fit gives $v_{MB}(x)$. Fig. 4.2 (b) shows the X vs

TOF distribution for the cluster ions after subtraction, the distribution along X is now centered around X = 0 for all ions. Like X, the Y values must also be corrected and centered around Y = 0.

The corrected (X, Y) values are then converted to 3D momentum vectors (p_x, p_y), using the following relations,

$$p_x = \frac{m.X}{TOF}$$

$$p_y = \frac{m.Y}{TOF} \qquad (4.1.5)$$

After conversion, the 3D momentum must be calibrated to match a selected reference ion or ion pair from the literature. For example, for the CO_2 cluster data set the well-studied two-body Coulomb explosion of CO_2 into O^+/CO^+ ion pair was used as reference. The data was calibrated to obtain the sum of momentum vectors of the ion pair to be zero and angular correlation between the vectors to be 180° for each O^+/CO^+ coincidence event.
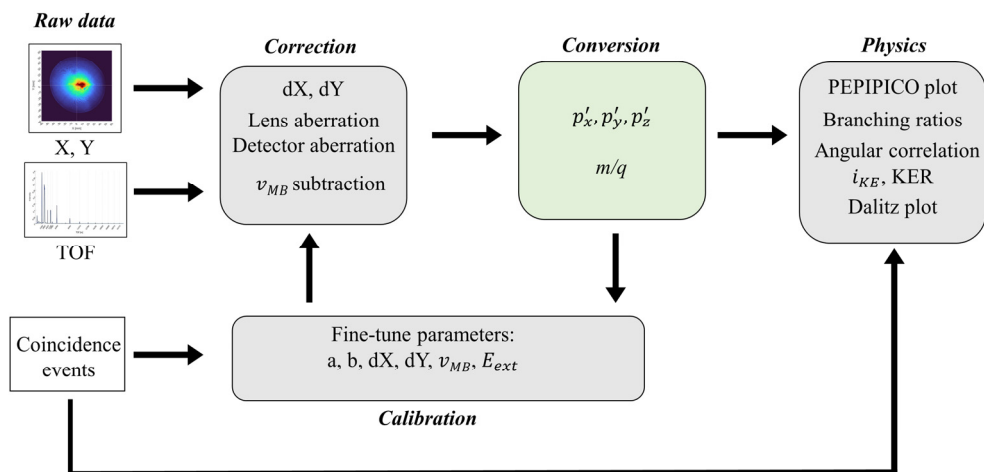
Figure. 4.3 The data analysis flowchart used in this thesis for treating 3D momentum imaging ion data.

During the calibration, the conversion parameters a, b, dX, dY, v_{MB} and E_{ext} are fine-tuned using iterative procedure. The (X, Y, TOF) ion data can be auto-calibrated using Python package MOCCA[4] (MOmentum Calibration in Coincidence data Analysis) written as a part of this thesis work. The package MOCCA is written

---

[4] MOCCA package available at https://doi.org/10.5281/zenodo.7630311

to work together with the ANACONDA_2[5] (ANAlyzing COincidence DAta 2) a MATLAB package used in this thesis for coincidence data analysis and plotting. The complete flow chart for data correction, conversion and calibration of 3D momentum imaging data is shown in Fig. 4.3. From the 3D momentum imaging of ions, we get information about the ion kinetic energy (i_{KE}), the total kinetic energy released (KER) in the fragmentation, the angular correlation and momentum correlation (Dalitz plot) between the ions and the branching ratios of fragmentation.

Ion-ion coincidence plot

The characteristic plot of a PEPIPICO experiment is the ion-ion correlation plot shown in Fig. 4.4. For double ion coincidence events, the TOF or m/q ratio of the second ion is plotted against the first ion. From the PEPIPICO plot we can visualize which ion pairs are created in the experiment and the relative abundance of the ion pairs. In Fig. 4.4 (a) the m/q ratio of the first and second ions are plotted for core ionized CO_2 clusters discussed in Paper I. We observe cluster fragments of the form $(CO_2)_m^+/(CO_2)_n^+$ and $O_2^+/(CO_2)_n^+$ (highlighted in red), where m and n are integers. The ion pairs $O_2^+/(CO_2)_n^+$ are the subject of interest in Paper I and are discussed later in the results section. There is also a dominant background of molecular fragmentation coming from the uncondensed CO_2 molecules in the cluster beam.

The PEPIPICO plot for the smaller fragments of CO_2 cluster beam are shown in Fig. 4.4 (b). The advantage of the TOF representation is that the slopes of the ion-ion correlation islands are directly related to the axial momentum component of the two ions (see equation (4.1.2)). Two-body Coulomb explosions result in PEPIPICO islands with slope of -1 because of correlated ions with equal and opposite momentum vectors, one of them is emitted towards the detector while the other in the opposite direction. For example, the ion pairs O^+/O^{2+}, CO^+/O^{2+} have definite slopes of -1, indicating two-body Coulombic explosion of triply charged CO_2. For the O^+/CO^+ ion pair island has a definite slope of -1 with a tail extending up to CO_2^{2+}. This feature is signature of a *metastable dication* dissociating outside the extraction region, which is known for CO_2^{2+} to have a lifetime of few μs[159] to even few seconds[160] for some electronic states. In the inset of Fig 4.12 (b) the zoomed in island of C^+/O^+, the ion pairs are formed by multiple fragmentation pathways and the resulting distributions are overlapped[67]. For multi-body or multi-step fragmentation pathways the islands can have no definite slope like the cluster islands.

---

[5] ANACONDA_2 package available at https://doi.org/10.5281/zenodo.5717994
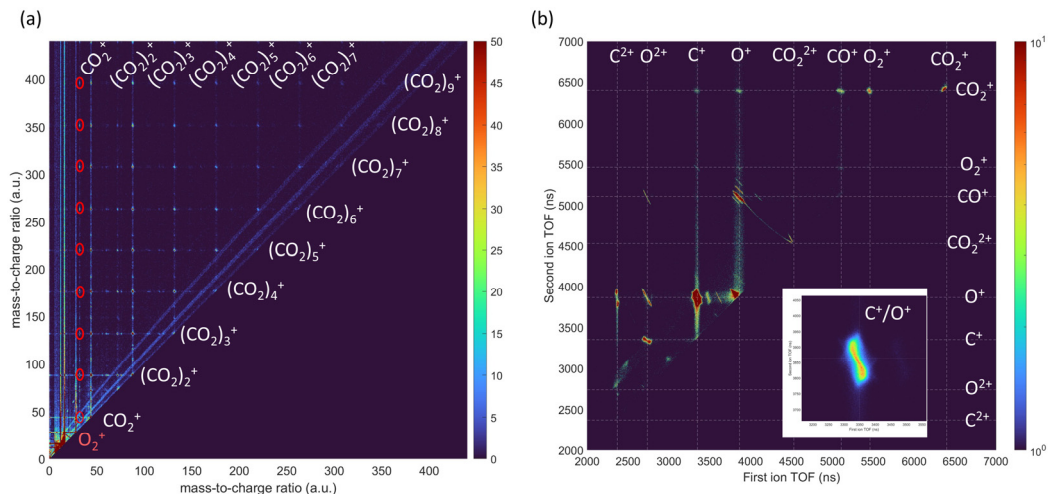
Figure. 4.4 Ion-ion correlation (PEPIPICO) plot showing the ion pairs produced by core-ionized CO_2 clusters of mean cluster size of about 20 molecules at photon energy of 320 eV. (a) PEPIPICO plot showing all the ion pairs recorded in coincidence, the color scale is chosen to emphasise false coincidences discussed in the text. The $O_2^+/(CO_2)_n^+$ are highlighted in red circles are discussed in Paper I. (b) PEPIPICO plot showing the smaller ion pairs coming from the molecular CO_2, these ion pair islands have well defined slopes which are discussed in text. The inset shows the C^+/O^+ ion pair island, the most dominant island in the PEPIPICO plot.

Additionally, false coincidences are also visible in a PEPIPICO plot as horizontal, vertical and diagonal continuous lines in Fig. 4.4 (a). Note the colormap in Fig. 4.4 (a) is scaled abnormally to make the false coincidences visible; the data is dominated by true coincidences. In a PEPIPICO experiment, the false coincidences arise when (i) three uncorrelated particles are detected in coincidence which creates a usually weak flat uniform distribution; (ii) the photoelectron and one ion are correlated whereas the other ion is not, which creates vertical and horizontal lines in the PEPIPICO; (iii) the two ions are correlated but the photoelectron is not, therefore the measured ion TOF values are inaccurate and this creates diagonal lines in the PEPIPICO. These false coincidences can be eliminated using different filters[161].

From the PEPIPICO plot, we can also calculate the branching ratios of the ion pairs by defining appropriate islands and removing false coincidences. For an ion pair A^+/B^+ is calculated as,

$$BR(A^+/B^+) = \frac{Counts\ in\ island\ A^+/B^+}{Total\ counts\ in\ PEPIPICO} \tag{4.1.6}$$

Dalitz plot

The momentum correlation between the ions in a coincidence event is investigated to find sequence of fragmentation[162–164]. The momentum correlation between two or three ions can be visualized using a type of ternary plot called Dalitz plot[165]. Each point on the Dalitz plot represents three variables which sum to a constant. For any ionization event with α ions we can calculate the residual momentum (p_{res}) of the event,

$$\overrightarrow{p_{res}} = -\overrightarrow{p_{sum}} = -\sum_\alpha \overrightarrow{p_\alpha} \tag{4.1.7}$$
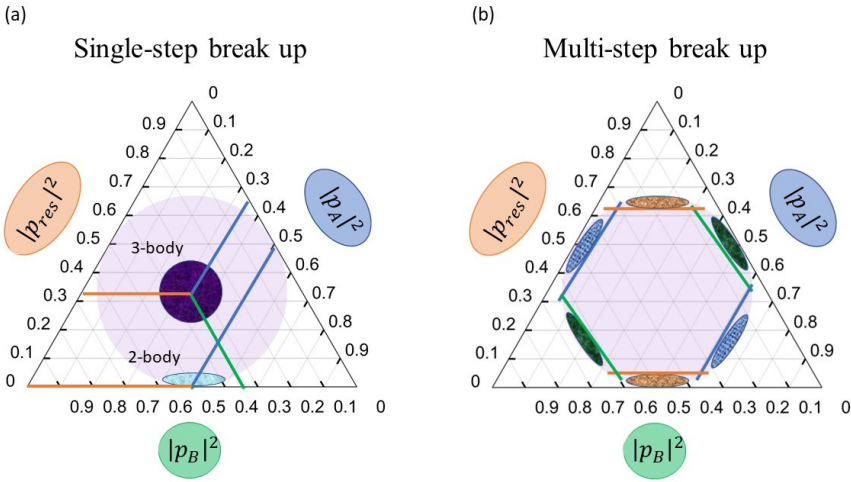
Figure. 4.5 Dalitz plot for a PEPIPICO event where two ions A⁺ and B⁺ are measured. (a) Typical Dalitz plot showing concerted or single-step fragmentation distribution for two-body and three-body breakup. The blue line shows the guide to read f_A, the green line shows f_B and the orange line shows f_{res}. (b) Typical Dalitz plot showing the six possible distrbutions for sequential or multi-step fragmentation into A⁺ and B⁺. Here the blue, green and orange line indicate which fragment was created first and thus has uncorrelated momentum.

For a PEPIPICO event, we have two ions A⁺ and B⁺ so we use the Dalitz plot to visualize the correlation between the momentum of A⁺, B⁺ and the p_{res}. The relative momentum fraction can be calculated as,

$$f_\alpha = \frac{|\overrightarrow{p_\alpha}|^2}{\sum_\alpha |\overrightarrow{p_\alpha}|^2} \tag{4.1.8}$$

Therefore, for each point on the Dalitz plot the value of the three variables (f_A, f_B, f_{res}) will add to a constant sum of 1.

The ternary coordinates[166] of the Dalitz plot are calculated as

$$x_{tern} = \frac{1}{2}(1 + f_A - f_B)$$

$$y_{tern} = \frac{\sqrt{3}}{2}(1 - f_A - f_B) = \frac{\sqrt{3}}{2}f_{res} \qquad (4.1.9)$$

Additionally, we have a constraint of conservation of total momentum,

$$\overrightarrow{p_A} + \overrightarrow{p_B} + \overrightarrow{p_{res}} = 0 \qquad (4.1.10)$$

This limits the ternary coordinates (x_{tern}, y_{tern}) to lie inside a circle[165]. Typical Dalitz plot and guided lines to read values (f_A, f_B, f_{res}) of the points are shown in Fig 4.13. We can now discuss the interpretation of a Dalitz plot for the PEPIPICO data.

Consider a single step or concerted fragmentation pathway in which the mother ion breaks up into two ions A^+ and B^+, using conservation of momentum we get,

$$\overrightarrow{p_A} = -\overrightarrow{p_B} \qquad (4.1.11)$$

For the case of a two-body breakup the residual momentum $p_{res} = 0$, so $f_{res} = 0$ and $f_A = f_B = 0.5$. Therefore, we get $x_{tern} = 0.5$ and $y_{tern} = 0$. For, a single step breakup of the mother ion into three fragments A^+, B^+ and C using conservation of momentum we get, $f_A = f_B = f_C = 0.33$ and the ternary coordinates are $x_{tern} = 0.5$ and $y_{tern} = 0.288$. The signature of two-body and three-body concerted breakup is shown in Fig. 4.5 (a) at $(x_{tern} = 0.5, y_{tern} = 0)$ and $(x_{tern} = 0.5, y_{tern} = 0.288)$ respectively.

The signature for sequential or multi-step breakup is shown in Fig. 4.5 (b). For complex molecules or clusters often more than three fragments are created so by using the Dalitz plot representation the multi-body problem can be reduced to a three-body one. We look at the momentum correlation between the two detected ions and the *missing fragment(s)* attributed to the residual momentum. The momentum of the fragment which is created first is uncorrelated to the distribution of other two fragments while the other two fragments are anticorrelated. For the green distributions in Dalitz plot of Fig. 4.5 (b) the fragment A^+ is created first and for the blue distributions the fragment B^+ is created first. When the residual missing fragment is created first, if it takes a share of the total momentum then the brown distribution appears at the top of the circle whereas if the residual fragment has no momentum the distribution appears at the bottom of the circle, identical to the 2-body breakup signature. Therefore, from the momentum correlation in the Dalitz plot we can infer which fragment was created first during the sequential breakup.

In Paper I, we used the Dalitz plot representation to disentangle sequential fragmentation channels of CO_2 clusters, which cannot be identified using the simple PEPIPICO plot due undefined slopes.

4.2 Kinetic energy measurement of Auger electrons

In this thesis the Auger electrons were measured using the EPICEA spectrometer with a double toroidal analyzer (DTA) and the VG Scienta R4000 with hemispherical analyzer (HSA). Here the data treatment techniques developed to get the Auger electron kinetic energy from these two analyzers are discussed.

4.2.1 Electron detector aberration (wiggles) correction

Local distortion of the electrostatic fields in a spectrometer leads to experimental artifacts that make it difficult to interpret the data. The DTA in EPICEA disperses the photo/Auger electrons as function their kinetic energy on the electron detector. On the 2D surface of the detector, the radial position of electrons with same kinetic energy should not depend on the azimuthal angle θ parallel to the plane of the detector. The experimental data from EPICEA however shows wiggles in the radius-θ plot because of the non-uniformities in the field likely to be due to the spectrometer holders. This angular dependence of the electron radius on the detector is shown in Fig. 4.6 (a). This causes broadening of the peaks in the electron energy spectrum and reduces the resolving power of the spectrometer, which is corrected by calculating the response function of the analyzer. For calibration, we used Xe 5s and 5p photoelectron spectra at the photon energies 255 eV, 260 eV, 265 eV, 275 eV and 282 eV such that the photoelectron lines span over the entire surface of the detector. Fig. 4.6 (a) shows that the wiggles of the photoelectron lines are a function of both the radius and θ. For outer part of the electron detector (low kinetic energy), the distortion of the photoelectron lines is more pronounced.

We start by identifying the radial values with maximum intensity (R_{max}) as a function of θ along the individual photoelectron lines, Fig. 4.6 (b) shows the identified maximum intensity points (coloured dots) for the selected 5 photoelectron lines. For the 5p doublet lines, one must be careful that the maximum intensity point belongs to the same line. After the maximum intensity points are identified, for each photoelectron line the average value (R_{avg}) is calculated. Then a calibration data set containing the R_{max}, θ and R_{avg} values of each photoelectron line is generated. This calibration data can be used to interpolate any given data set recorded under the same experimental condition to remove the angular dependence of the photoelectrons. Here, we used the calibration data for interpolating our reference data in Fig. 4.6 (a), the results are shown in Fig. 4.7 (a). The R_{max} values calculated

from the interpolated data are shown in Fig. 4.7 (b) and they appear to be straight lines with small deviations. Compared to Fig. 4.6, there is a significant improvement in the angular dependence of the photoelectron lines and the wiggles are corrected.
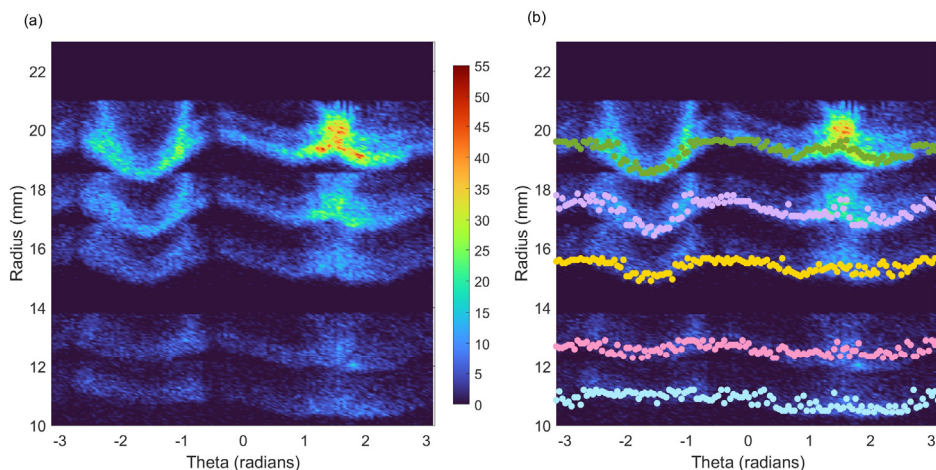
Figure. 4.6 The angular dependence of radial position of the photoelectron lines of Xe 5s and 5p recorded using the EPICEA setup at photon energies 255 eV to 282 eV. The raw experimental data of the wiggles is shown in (a) and the calculated maximum intensity points at fixed theta values for the selected photoelectron lines are shown in (b). These points are used for the electron detector aberration corrections.
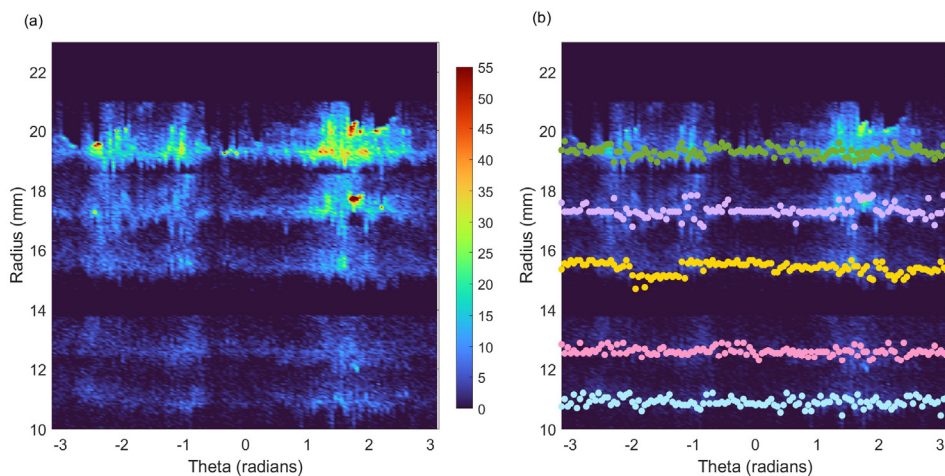
Figure. 4.7 The corrected data from Fig. 4.6 after electron detector aberration correction is shown in (a) and the calculated maximum intensity points at fixed theta values for the selected photoelectron lines are shown in (b). Compared to Fig. 4.6 the wiggles in the radial positions have been removed.

Integrating over all the θ values, we can plot the photoelectron lines of Xe as a function of the electron detector radius. In Fig. 4.8 (a) the reference data for Xe from Fig. 4.6 (a) is shown in blue and the corrected Xe data from Fig. 4.7 (a) is shown in yellow. Due to the wiggles of the photoelectron lines the peaks are broadened and the Xe 5p doublet peaks are not resolved. After the correction, the photoelectron peaks are narrower, and we can resolve $5p_{3/2}$ and $5p_{1/2}$ doublet peaks. Therefore, the wiggle correction procedure described above improved the resolution of the photoelectron spectrum. Next, we used the calibration data generated from Xe, to correct the wiggles in the Auger electron spectrum of adamantane recorded at 287.1 eV (used in Paper III). The Auger electron spectrum of adamantane is shown before and after correction in Fig. 4.8 (b). After correction, the peaks are narrower, and the sharp peak created around 19 mm radius can be an artifact from the wiggle correction.
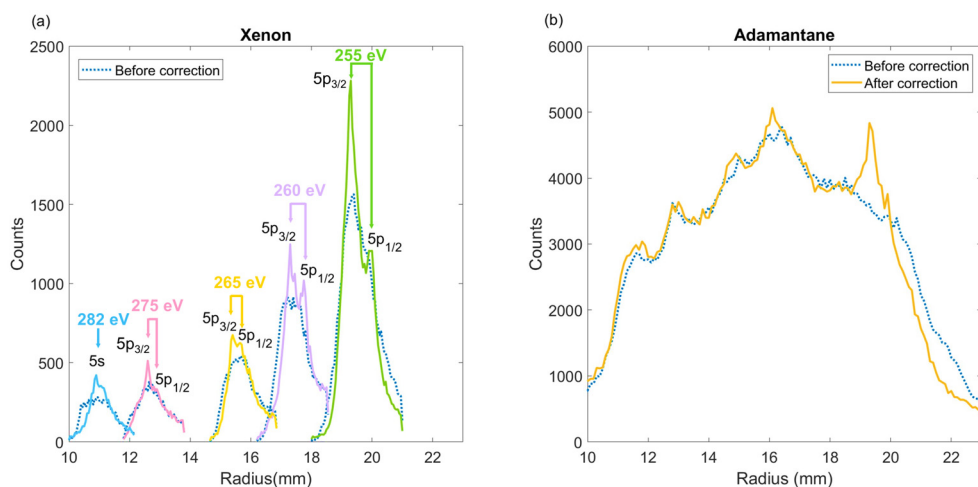

Figure. 4.8 Photoelectron spectrum recorded using EPICEA before and after electron detector aberration correction. (a) shows the photoelectron lines of Xe 5s and 5p at photon energies 255 eV, 260 eV, 265 eV, 275 eV and 282 eV. (b) shows the Auger electron spectrum of adamantane at 287.1 eV photon energy. After correction the resolution is improved for the photoelectron lines.

After the detector aberration correction, we calibrate the electron radial data measured using EPICEA to get the kinetic energy of the electrons. The relation between the electron radius (r) on the detector and the kinetic energy (e_{KE}) of the electrons is given by the empirical formula[167],

$$(e_{KE} - e_{KE0}) = a(r - r_0) + b\left(\frac{1}{r} - \frac{1}{r_0}\right) \qquad (4.2.1)$$

Here, a and b are dispersive coefficients for the selected pass energy of the DTA in EPICEA and the reference value r_0 is the radius of electrons retarded to a defined kinetic energy e_{KE0} measured at the selected pass energy. The pass energy of the DTA in EPICEA was set to 250 eV for all the electron measurements discussed in this thesis.

For calibrating the adamantane data used in Paper II and III, we recorded the photoelectron spectrum of Xe 5s and 5p states by changing the photon energy from 255 eV to 282 eV using EPICEA. The binding energies (E_b) of Xe 5s electron is 23.3 eV and the Xe 5p doublet $5p_{3/2}$ and $5p_{1/2}$ is 12.13 and 13.43 eV respectively. Using the equation, $e_{KE} = hv - E_b$ we can calculate the values of e_{KE} for the measured photoelectrons. The $5p_{1/2}$ photoelectron line measured at 260 eV photon energy was set as the reference, $r_0 = 17.76\ mm$ and $e_{KE0} = 246.57\ eV$. To find the dispersive coefficients, we plot the calculated $e_{KE} - e_{KE0}$ values as a function of measured r values and fitted the equation (4.2.1). The result of the fitting for the Xe 5s and 5p states are shown in Fig. 4.9, from the fit we get, $a = -1.075$ and $b = 430.2$. The measured Auger electron radius of adamantane is then converted to kinetic energy using the equation (4.2.1), using $r_0 = 17.76\ mm$, $e_{KE0} = 246.57\ eV$, $a = -1.075$ and $b = 430.2$ for the pass energy of 250 eV.
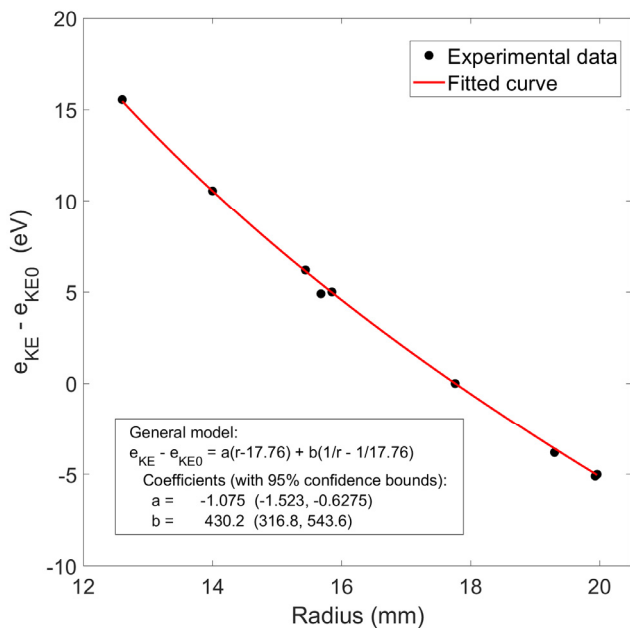

Figure. 4.9 The electron kinetic energy calibration curve for electron detector radius recorded using the EPICEA setup. The photoelectron lines of Xe 5s and 5p at photon energies 255 eV to 282 eV are used for calibration, the experimental data is fitted to the empirical model shown in the figure to find the parameteers a and b.

68

4.2.2   Background correction of Auger-yield NEXAFS

Auger-yield Near edge X-ray absorption spectrum (NEXAFS) of adamantane molecule (discussed in paper II and III) was measured as a function of photon energy near the C 1s ionization threshold (~ 289.7 eV) using the wide-angle lens VG-Scienta R4000 hemispherical electron energy. Fig. 4.10 (a) shows the experimental data after energy calibration (CO_2 used for reference) and second harmonic correction for the photon flux at the beamline. The measured Auger electron spectra contain diagonal lines coming from the valence photoelectron background. To remove the photoelectron background, the 'pure' valence photoelectron spectrum (val_{PES}) at $hv_{0\,=}285$ eV is extrapolated to the measured photon energy range using the relation

$$val_{PES}(hv) = \ val_{PES}(hv_0) + (hv - hv_0) \qquad (4.2.2)$$

The generated background is then passed through an averaging filter to remove any harsh features due to extrapolation. The created photoelectron background is shown in Fig. 4.10 (b), here the intensity of the photoelectron spectrum is assumed to be independent of the photon energy range 285-300 eV. The background is then subtracted from the experimental data to get the corrected data shown in Fig. 4.10 (c). This correction procedure is important to interpret the high Auger electron kinetic energies correctly. The procedure described here is like the one reported by Lytken et al. where they applied an iterative loop for background correction[168]. Both the corrections procedures assume that the val_{PES} cross section is constant in the small photon energy range near the C 1s ionization edge. The corrected data is then used to get the resonant Auger spectrum (RAES) discussed later in Chapter 4. Alternatively, one can measure the NEXAFS using total ion yield (TIY) method and to get information about near edge features as function of photon energy.
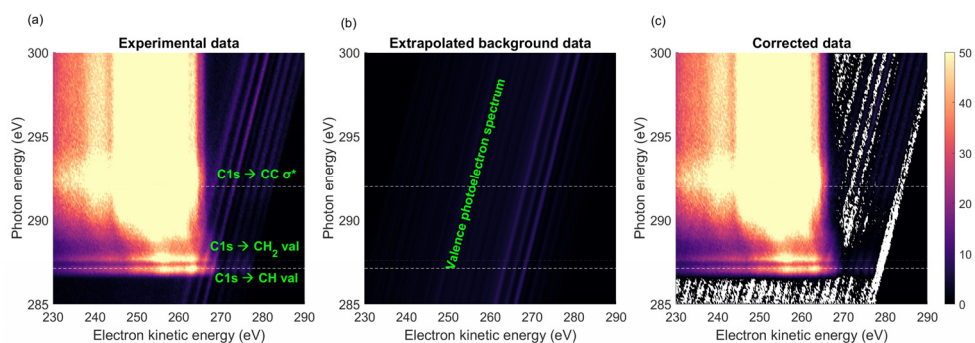

Figure. 4.10 Cleaning procedure of the photon energy scan of the Auger electron spectrum for adamantane near the C-1s ionization edge, (a) shows the experimental data, (b) the generated valence photoelectron background and (c) shows the intensity corrected data calculated by subtracting (b) from (a).

4.3 Removal of false coincidences

In this section, the use of random pulse-triggered events for false coincidence removal in electron-ion coincidence data recorded using EPICEA is described. EPICEA uses a pulse generator to produce random triggers to extract the ions present in the interaction region. In this thesis, the statistical treatment for removal of false coincidences developed by Prumper and Ueda[169] is applied and extended for new applications. Similar notations are used here for easy comparison with the paper. Multiparticle coincidence data is treated to generate Auger electron spectrum (AES), ion TOF or mass spectrum, Auger electron-Photoion coincidence (AEPICO) plot, Auger electron-Photoion-Photoion coincidence (AEPIPICO) plot, ion pair specific AES and Auger electron specific AEPIPICO plot. The benefits of the statistical methods are demonstrated using experimental data of adamantane. The data treatment discussed in this section was essential to obtain the results reported in Paper II and III.

General formalism
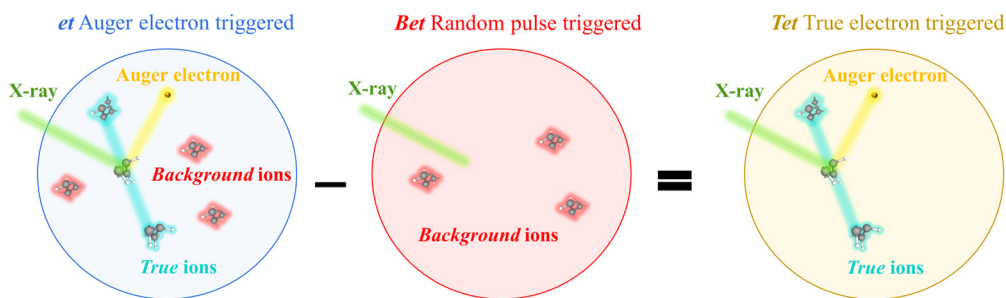
Figure. 4.11 Schematic showing the procedure for removing false coincidences from the experimental Auger electron-ion coincidence data. The Auger electron is shown in yellow, the background (false) ions in red and the true ions in blue.

The events triggered by Auger electrons (*et* events) include *true* ions formed from the fragmentation of the same molecule that emitted the Auger electron, as well as *background* ions, which are not correlated to the Auger electron. Our objective is to identify the events containing only true ions (*Tet*) and eliminate any contributions from events that involve false coincidences with the background ions, as shown in Fig. 4.11. To remove the false coincidences, we calculate the background contribution (*Bet*) using the events triggered by the random pulse trigger (*rt* events), which consist exclusively of background ions. This section aims to calculate the background contribution (*Bet*) for different multiparticle coincidence data.

We calculate the true coincidences (*Tet*) by subtracting the background contribution (*Bet*) from the Auger electron-triggered (*et*) experimental data, i.e.,

$$Tet = et - Bet \qquad (4.3.1)$$

In the data file, we should first distinguish between the ionization events triggered by electrons (N_e) and events triggered by random triggers (N_{RND}). The probability of detecting x ions in the experiment via electron trigger (et) or random trigger (rt) in the data set is calculated as,

$$etP_x = \frac{etN_x}{N_e} \qquad (4.3.2)$$

$$rtP_x = \frac{rtN_x}{N_{RND}} \qquad (4.3.3)$$

In equation (4.3.2), etN_x is the actual number of electron-triggered events containing x ions and in equation (4.3.3), rtN_x is the actual number of random-triggered events containing x ions. Here, we assume that the probability of detecting false ions is not affected by the presence of true ions. Therefore, the probability of detecting x false ions in electron-triggered events is also rtP_x.

The true coincidence data (*Tet*) can also be expressed in terms of a hypothetical coincidence data (*Het*), which consists solely of true ions. The probability of detecting true coincidence events is equal to the probability of detecting zero background ions (rtP_0). This can be expressed mathematically as,

$$Tet = rtP_0 . Het \qquad (4.3.4)$$

The hypothetical coincidence data (*Het*) can be related to the electron-triggered using the following set of equations. The probability of detecting j true ions in an event with total x ions is labelled as TP_j. For instance, if no ion is detected in an electron-triggered event (etP_0), it means that neither a true (TP_0) nor a false ion (rtP_0) was detected.

$$etP_0 = rtP_0 . TP_0 \qquad (4.3.5)$$

Similarly, for $x = 1, 2$ we can write the probabilities as,

$$etP_1 = rtP_0 . TP_1 + rtP_1 . TP_0 \qquad (4.3.6)$$

$$etP_2 = rtP_2 . TP_0 + rtP_1 . TP_1 + rtP_0 . TP_2 \qquad (4.3.7)$$
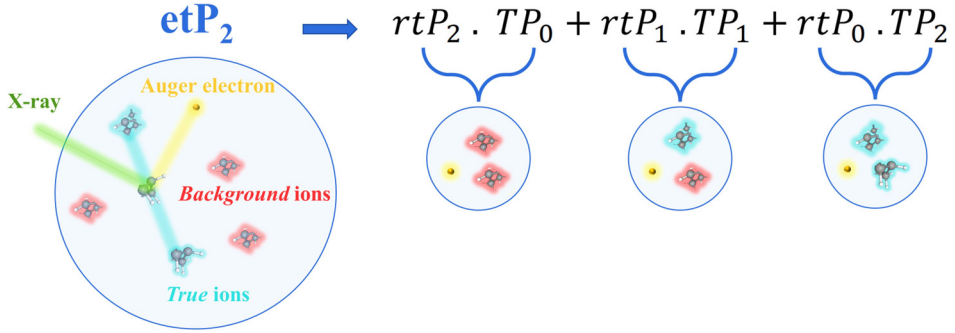
Figure. 4.12 The probability of detecting two ions in an electron-triggered event is explained visually. The ions in red are the background (false) ions and the ions in blue are the true ions. An electron-triggered event with two ions can consists of Auger electron in coincidence with two background ions, or Auger electron in coincidence with one background ion and a true ion, or Auger electron in coincidence with two true ions.

The visual representation of etP_2 is shown in Fig. 4.12, the two-ion event can consist of three possibilities, two false ions, or one true and one false ion, or two true ions. In terms of probability, we should consider all the possible cases of detecting electron-triggered x ions, because of i false ions and j true ions where $i + j = x$. In general, for event with x ions we can write as,

$$etP_x = \sum_{i+j=x}^{i,j} rtP_i . TP_j \tag{4.3.8}$$

The above equation can be rewritten by replacing TP_j with the hypothetical coincidence data Het_j and etP_x with the electron-triggered coincidence data et_x.

$$\frac{et_x}{N_e} = \sum_{i+j=x}^{i,j} rtP_i . \frac{Het_j}{N_e} \tag{4.3.9}$$

Using the relation between Tet and Het in (4.3.4), we can rewrite the above equation as,

$$\frac{et_x}{N_e} = \sum_{i+j=x}^{i,j} rtP_i . \frac{Tet_j}{rtP_0 . N_e} \tag{4.3.10}$$

72

This equation is solved to achieve the general form $Tet = et - Bet$ and Bet is calculated as a function of random-triggered (rt) coincidence data. Before removing random coincidences, the data must be calibrated using the procedures discussed in previous sections. Random coincidence removal is the last step in the data analysis giving us true coincidence histograms of the experimental observables.

Auger electron spectrum (AES)
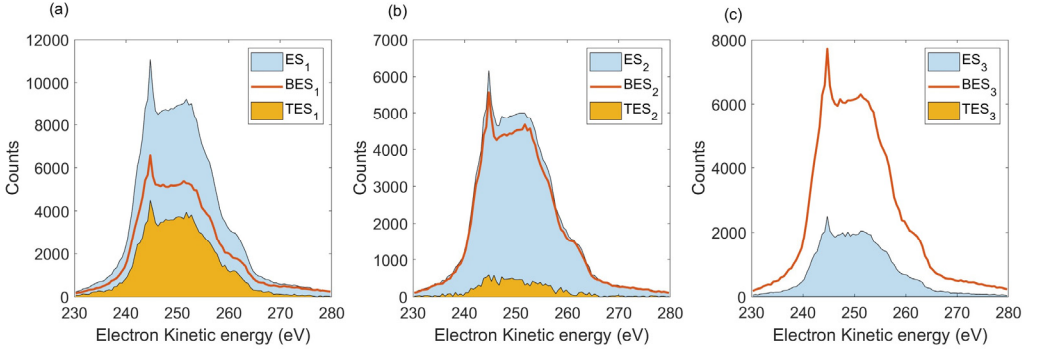
Figure. 4.13 The Auger electron kinetic energy spectrum (AES) of adamantane recorded at 350 eV photon energy using the EPICEA setup. The experimental data is shown in blue, the calculated background is shown in red line and the corrected true electron spectrum is shown in yellow. The AES for one electron and one ion coincidence events is shown in (a), for one electron and two ions coincidence events is shown in (b) and one electron and three ions coincidence events is shown in (c).

Filtering the electron spectrum is not straightforward because the random triggers do not measure any electron data, so we don't have a reference background measurement. However, using the probabilities calculated in the previous section we can generate a background and subtract it from the measured electron spectrum. The total measured electron kinetic energy $AES(e_{KE})$ spectrum consists of $ES_x(e_{KE})$, where x is number of ions detected in coincidence with these electrons.

$$AES(e_{KE}) = ES_0(e_{KE}) + ES_1(e_{KE}) + ES_2(e_{KE}) + ES_3(e_{KE}) \qquad (4.3.11)$$

Let's assume a hypothetical spectrum $HES_x(e_{KE})$ consisting of only x true ions. We can write $HES_x(e_{KE})$ as a function of $ES_x(e_{KE})$ using equation (4.3.9),

$$HES_0(e_{KE}) = \frac{ES_0(e_{KE})}{rtP_0} \qquad (4.3.12)$$

$$HES_1(e_{KE}) = \frac{ES_1(e_{KE}) - rtP_1 \cdot HES_0(e_{KE})}{rtP_0} \qquad (4.3.13)$$

73

$$HES_2(e_{KE}) = \frac{ES_2(e_{KE}) - rtP_2 . HES_0(e_{KE}) - rtP_1 . HES_1(e_{KE})}{rtP_0} \quad (4.3.14)$$

Now the true corrected spectrum ($TES_x(e_{KE})$) with no background ion contribution is,

$$TES_x(e_{KE}) = rtP_0 . HES_x(e_{KE}) \quad (4.3.15)$$

To make it easier for data correction, we rewrite in the form of *true* spectrum is equal to measured spectrum minus the background spectrum ($BES_x(e_{KE})$).

$$TES_x(e_{KE}) = ES_x(e_{KE}) - BES_x(e_{KE}) \quad (4.3.16)$$

Here $BES_x(e_{KE})$ is function of $ES_{x'}(e_{KE})$ and constants $c_{x'+1}$.

$$BES_x(e_{KE}) = \sum_{x'<x}^{x'} c_{x'+1} . ES_{x'}(e_{KE}) \quad (4.3.17)$$

Now for events with no ions,

$$TES_0(e_{KE}) = rtP_0 . HES_0(e_{KE}) = ES_0(e_{KE}) \quad (4.3.18)$$

$\therefore TES_0(e_{KE}) = ES_0(e_{KE})$ and $BES_0(e_{KE}) = 0$, is the background for events with no ions. Similarly for events with 1 ion,

$$TES_1(e_{KE}) = rtP_0 . HES_1(e_{KE}) = rtP_0 . \frac{ES_1(e_{KE}) - rtP_1 . HES_0(e_{KE})}{rtP_0}$$
$$= ES_1(e_{KE}) - \frac{rtP_1}{rtP_0} . ES_0(e_{KE}) \quad (4.3.19)$$

Rewriting in the form,

$$TES_1(e_{KE}) = ES_1(e_{KE}) - BES_1(e_{KE}) \quad (4.3.20)$$

Comparing equations (4.3.18) − (4.3.19),

$$BES_1(e_{KE}) = c_1 . ES_0(e_{KE}) \quad (4.3.21)$$

$$c_1 = \frac{rtP_1}{rtP_0} \quad (4.3.22)$$

Similarly,

$$BES_2(e_{KE}) = c_2.ES_0(e_{KE}) + c_1.ES_1(e_{KE})$$

$$BES_3(e_{KE}) = c_3.ES_0(e_{KE}) + c_2.ES_1(e_{KE}) + c_1.ES_2(e_{KE}) \quad (4.3.23)$$

$$c_2 = \frac{rtP_2}{rtP_0} - \frac{rtP_1^2}{rtP_0^2} \quad (4.3.24)$$

$$c_3 = \frac{rtP_3}{rtP_0} + \frac{rtP_1^2}{rtP_2} - 2.\frac{rtP_1 . rtP_2}{rtP_0^2} \quad (4.3.25)$$

Fig. 4.13 (a), (b) and (c) shows the corrected Auger electron spectrum for events with one, two and three ions for core ionized adamantane data. In blue is the experimental measurement $ES_x(e_{KE})$, the red line shows the calculated background $BES_x(e_{KE})$ and in yellow is the corrected true spectrum $TES_x(e_{KE})$ for $x = 1, 2$ and 3. We observe that the background contribution increases with x. In Fig. 4.13 (a), the electrons measured below 240 eV and above 270 eV are mainly random contributions, and the corrected spectrum $TES_1(e_{KE})$ is baseline corrected. Overall, the features in ES_1 and TES_1 are similar. For $x = 2$, random background correction significantly changes the spectrum ES_2 to TES_2. The sharp feature at about 245 eV mainly comes from background ions and is removed after correction. The only true ions are detected in coincidence with electrons having energy 240 to 265 eV. For $x = 3$, the background ions contribution is expected to be larger than the measured ions. This might be because of the low efficiency of detecting 3 ions in coincidence with electrons. After correction TES_3 is negative and is set to zero. For an ideal experiment capable of detecting all ions, the area of $BES_x(e_{KE})$ would be smaller than or equal to the area of $TES_1(e_{KE})$.

Ion spectrum

Next, we remove background ion contributions from ion mass-to-charge ($m2q$) spectrum. The experimentally measured electron-triggered and random-triggered ion $m2q$ spectra of all ions are labelled as $etAI(m2q)$ and $rtAI(m2q)$ respectively. Now, the true $m2q$ spectrum $TetAI(m2q)$ is calculated as,

$$TetAI(m2q) = etAI(m2q) - BetAI(m2q) \quad (4.3.26)$$

The background ion ($BetAI(m2q)$) contribution is calculated by scaling $rtAI(m2q)$ as,

$$BetAI(m2q) = SC .rtAI(m2q) \quad (4.3.27)$$

$$SC = \frac{N_e}{N_{RND}} \quad (4.3.28)$$

The scaling factor SC is the ratio of total number of electron-triggered events to the total number of random-triggered events.

Fig. 4.14 shows the corrected $m2q$ spectrum of all ions for measured from the fragmentation of core excitation adamantane molecule. The generated background $BetAI(m2q)$ removes the background noise from experimentally measured data. The true spectrum $TetAI(m2q)$ has baseline close to zero in between the peaks and the width of the ion peaks is changed after correction. Equations (4.3.26) -(4.3.28) can be used to filter other properties of ions like time-of-flight (TOF), kinetic energy distributions or angular distributions.
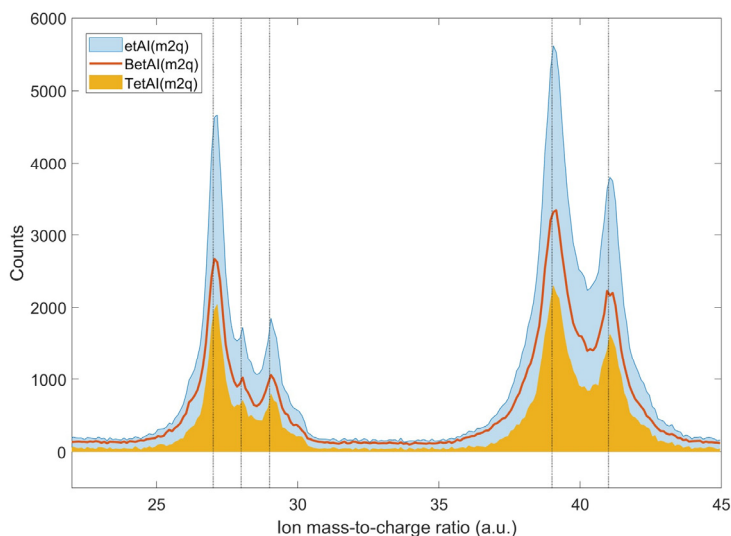
Figure. 4.14 The ions mass-to-charge ratio spectrum of all ions produced by core-excited adamantane recorded at 287.6 eV photon energy using the EPICEA setup. The experimental data is shown in blue, the calculated background is shown in red line and the corrected true ion spectrum is shown in yellow.

Auger electron-ion coincidence spectrum
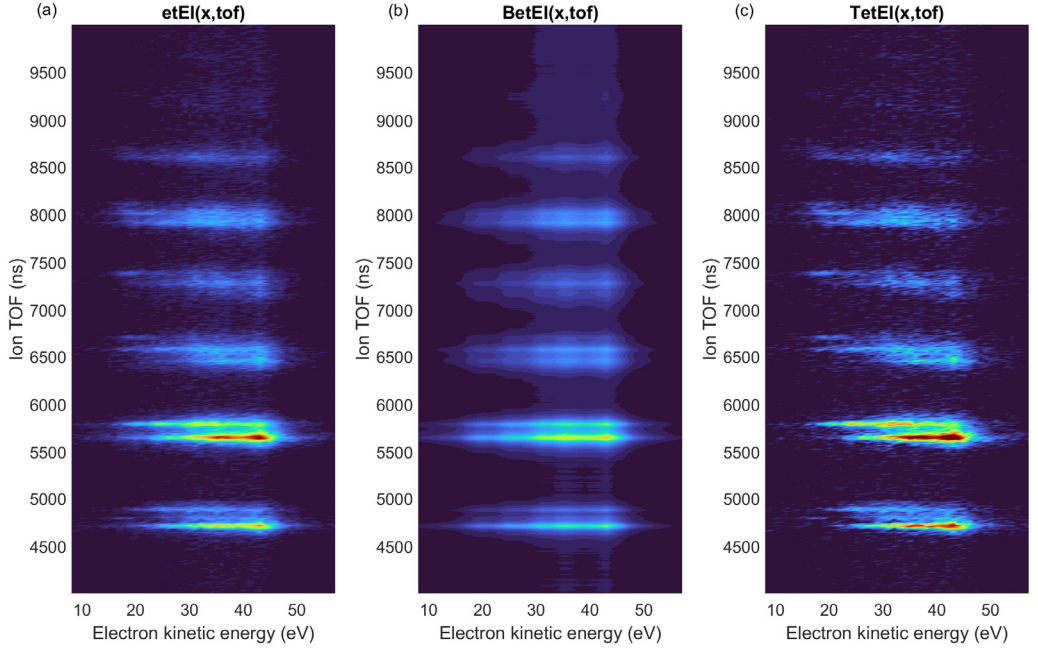
Figure. 4.15 The AEPICO plots of core-excited adamantane at photon energy of 287.1 eV recorded using the EPICEA setup. The experimental data is shown in (a), the calculated background is shown in (b) and the corrected true AEPIPICO is shown in (c). The histograms are normalized by the sum of total counts and the same color scale is used for the three plots.

A subset of the AEPIPICO data contains one electron and one ion (AEPICO) events; these events can be attributed to fragments of the cation, the mother ion, or *aborted* coincidences. This data contains information about two particles is labelled as $etEI(e_{KE}, tof)$ and contains events where one electron was measured with a true ion and events where one electron was measured with a background ion. Using the general expression (4.3.9), we can write in terms of probability as,

$$\frac{etEI(e_{KE}, tof)}{N_e} = rtP_0 \cdot \frac{HetEI(e_{KE}, tof)}{N_e} + \frac{HES_0(e_{KE})}{N_e} \cdot \frac{rtI(tof)}{N_{RND}}$$

$$(4.3.29)$$

Here $HetEI(e_{KE}, tof)$ is the hypothetical AEPICO data containing no background ion contributions and $HES_0(e_{KE})$ is the hypothetical electron spectrum with no ions, $HES_0(e_{KE}) = \frac{ES_0(e_{KE})}{rtP_0}$ and $HetEI(e_{KE}, tof) = \frac{TetEI(e_{KE}, tof)}{rtP_0}$. $TetEI(e_{KE}, tof)$ is

the true AEPICO data after background ion contributions are removed. Using these relations in (4.3.33),

$$etEI(e_{KE}, tof) = TetEI(e_{KE}, tof) + \frac{ES_0(e_{KE})}{rtP_0} \cdot \frac{rtI(tof)}{N_{RND}} \qquad (4.3.30)$$

Therefore, the background of the AEPICO data that should be subtracted from $etEI(e_{KE}, tof)$ to get the true data is,

$$BetEI(e_{KE}, tof) = \frac{ES_0(e_{KE})}{rtP_0} \cdot \frac{rtI(tof)}{N_{RND}} \qquad (4.3.31)$$

Fig. 4.15 (a) shows the experimental AEPICO data recorded for adamantane at 287.1 eV. In the experimental data the signal to noise ratio is poor, because of the background in between the features. The calculate background shown in Fig. 4.15 (b) shows a constant background for the smaller kinetic energy. After subtraction, the corrected data in Fig. 4.15 (c) has better resolution because of the improved signal to noise ratio.

Auger electron-ion-ion coincidence spectrum
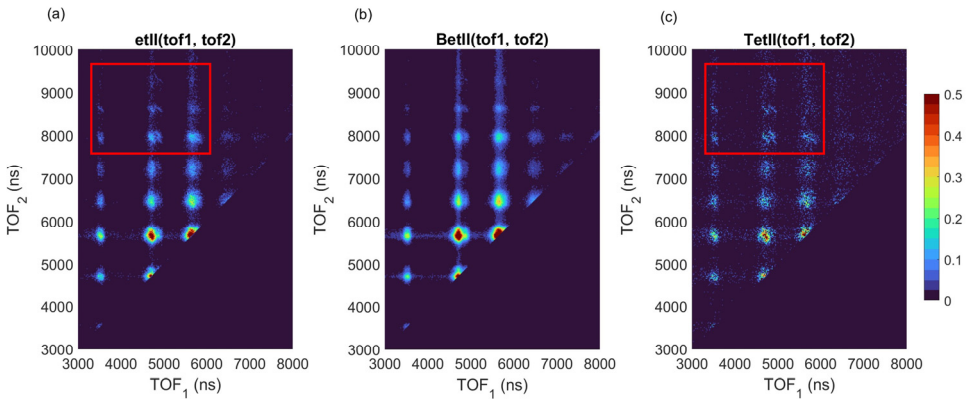
Figure. 4.16 The AEPIPICO plots of core-ionized adamantane at photon energy of 350 eV recorded using the EPICEA setup. The AEPIPICO shows the ion-ion correlation between the TOF of the first and second ions recorded in coincidence events. The experimental data is shown in (a), the calculated background is shown in (b) and the corrected true AEPIPICO is shown in (c). The histograms are normalized by the sum of total counts and the same color scale is used for the three plots.

For an electron-triggered event with two ions we can make a 2D map of the sorted ion TOF showing the correlation between them. Commonly referred to as AEPIPICO plot is shown in Fig. 4.16 (a) for core ionized adamantane. We label this

2D histogram as $etII(tof_1, tof_2)$, where tof_1 is the TOF of the ion detected first and tof_2 is the TOF of the ion detected second therefore the condition $tof_1 < tof_2$ is always fulfilled. For the random-triggered events, we can also make a 2D map of the sorted ion TOF, $rtII(tof_1, tof_2)$. The *true* 2D map ($TetII(tof_1, tof_2)$) of ion TOF is calculated using,

$$TetII(tof_1, tof_2) = etII(tof_1, tof_2) - BetII(tof_1, tof_2) \qquad (4.3.32)$$

Here, $BetII(tof_1, tof_2)$ is the contribution of background ions which depends on $rtII(tof_1, tof_2)$ and is determined here.

In the instance of two ions A and B measured in coincidence, we have 4 possible cases: A true and B true, A false and B true, A true and B false, A false and B false. Using the general expression (4.3.9), we can write the following probability relation,

$$
\begin{aligned}
\frac{etII(tof_1, tof_2)}{N_e} &= rtP_0 \cdot \frac{HetII(tof_1, tof_2)}{N_e} + \frac{rtI(tof_1)}{N_{RND}} \cdot \frac{HetI(tof_2)}{N_e} \\
&+ \frac{HetI(tof_1)}{N_e} \cdot \frac{rtI(tof_2)}{N_{RND}} + TP_0 \cdot \frac{rtII(tof_1, tof_2)}{N_{RND}}
\end{aligned}
\qquad (4.3.33)
$$

Here, $HetII(tof_1, tof_2)$ and $HetI(tof_{1,2})$ are the hypothetical spectra with no random contributions for electron-triggered events with 2 ions and 1 ion respectively. The true spectrum $TetII(tof_1, tof_2) = rtP_0 \cdot HetII(tof_1, tof_2)$, substituting this value in equation (4.3.33) we get,

$$
\begin{aligned}
TetII(tof_1, tof_2) = \; & etII(tof_1, tof_2) - TP_0 \cdot SC \cdot rtII(tof_1, tof_2) \\
& - \frac{rtI(tof_1) \cdot HetI(tof_2) + HetI(tof_1) \cdot rtI(tof_2)}{N_{RND}}
\end{aligned}
\qquad (4.3.34)
$$

The hypothetical spectrum $HetI(tof_{1,2})$ can be written as

$$
\begin{aligned}
HetI(tof_{1,2}) &= \frac{TetI(tof_{1,2})}{rtP_0} = \frac{etI(tof_{1,2}) - BetI(tof_{1,2})}{rtP_0} \\
&= \frac{etI(tof_{1,2}) - TP_0 \cdot SC \cdot rtI(tof_{1,2})}{rtP_0}
\end{aligned}
\qquad (4.3.35)
$$

Substituting the value from equation (4.3.35) in (4.3.34) and using the relation (4.3.32), we get,

$$BetII(tof_1, tof_2) = TP_0 . SC . rtII(tof_1, tof_2)$$
$$+ \frac{etI(tof_1). rtI(tof_2) + etI(tof_2). rtI(tof_1)}{rtP_0 . N_{RND}}$$
$$- \frac{2. TP_0 . SC . rtI(tof_1). rtI(tof_2)}{rtP_0 . N_{RND}} \tag{4.3.36}$$

To implement this equation to real data, one must consider all possible combinations of tof_1 and tof_2 in the TOF range relevant to the sample. The histogram $BetII(tof_1, tof_2)$ is calculated using loops of tof_1 and tof_2. For values $tof_1 > tof_2$, the value of $BetII(tof_1, tof_2)$ was set to zero.

The calculated background $BetII(tof_1, tof_2)$ for the experimental data is shown in Fig. 4.16 (b). As expected, the islands in the 2D map of $BetII(tof_1, tof_2)$ are blurred and have no sharp features. After histogram subtraction of background using equation (4.3.36), the *true* spectrum $TetII(tof_1, tof_2)$ is shown in Fig. 4.16 (c). In the corrected spectrum, we can clearly see the slopes of the islands (highlighted in red) in the 2D map, which are important for physical interpretation of ultrafast fragmentation dynamics. Also, the vertical and horizontal lines observed in Fig. 4.16 (a) due to noise are removed after correction. Similar correction can be done for m2q instead of TOF for ion-ion coincidence data.

Auger electron specific ion-ion coincidence spectrum
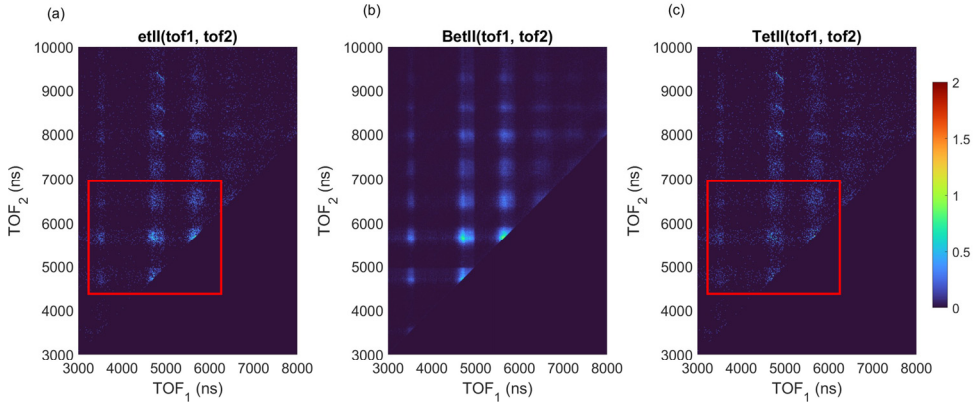
Figure. 4.17 The electron specific AEPIPICO plots of core-ionized adamantane at photon energy of 350 eV recorded using the EPICEA setup. The Auger electron kinetic energy detected in coincidence with these ions is fixed to be in the range of 262 to 280 eV. The experimental data is shown in (a), the calculated background is shown in (b) and the corrected true AEPIPICO is shown in (c). The histograms are normalized by the sum of total counts and the same color scale is used for the three plots.

The AEPIPICO data contains information about 3 particles and can be interpreted in different ways. The 3D data set is labelled as $etEII(e_{KE}, tof_1, tof_2)$. The total

ion-ion coincidence map $etII(tof_1, tof_2)$ is a function of the electron kinetic energy e_{KE}.

$$etII(tof_1, tof_2) = \sum_{all\ e_{KE}} etEII(e_{KE}, tof_1, tof_2) \qquad (4.3.37)$$

Therefore, we can plot the 2D map of electron-triggered ion-ion coincidence for a specific electron kinetic energy range. This section of the data treatment is an extension of the filtering described by Prumper and Ueda[169].

For the selected range of e'_{KE}, the modified 2D histogram is $etII(tof_1, tof_2)'$. For modified data set, we calculate new scaling factor SC',

$$SC' = \frac{N'_e}{N_{RND}} \qquad (4.3.38)$$

Here N'_e is the total number of electron-triggered events for electrons having kinetic energy e'_{KE}. The probabilities of detecting x ions also can be recalculated as,

$$etP_x' = \frac{etN_x'}{N_e'} \qquad (4.3.39)$$

etN_x' is the number of electron-triggered events containing x ions and electrons with kinetic energy in the range e'_{KE}. Note that the probabilities of the random-triggered events rtP_x are not affected by our selection. We also need to calculate the probability of detecting zero true ions after an electron trigger with energy e'_{KE} using equation (4.3.5),

$$TP_0' = \frac{etP_0'}{rtP_0} \qquad (4.3.40)$$

Now we can rewrite the equation (4.3.36) for 2D map of the background for ion-ion coincidence with electrons having energy e'_{KE},

$$\begin{aligned} BetII(tof_1, tof_2)' = {}& TP_0' . SC'. rtII(tof_1, tof_2) \\ & + \frac{etI(tof_1)'. rtI(tof_2) + etI(tof_2)'. rtI(tof_1)}{rtP_0. N_{RND}} \\ & - \frac{2. TP_0' . SC'. rtI(tof_1). rtI(tof_2)}{rtP_0. N_{RND}} \end{aligned} \qquad (4.3.41)$$

For calculating this 2D histogram from real data, the procedure is like the previous section with an additional condition for $etI(tof_{1,2})'$. The histogram for $etI(tof_{1,2})'$

should also satisfy the condition that the electrons having energy e'_{KE}. After the background is calculated, the true 2D map $TetII(tof_1, tof_2)'$ is calculated using the equation (4.3.32).

We utilized the same core-ionized adamantane dataset as in Fig. 4.16 and selected the electron kinetic energy range of $e'_{KE} = 262.1$ to 280 eV. Fig. 4.17 (a) shows the AEPIPICO plot of the experimental data $etII(tof_1, tof_2)'$ for the selected energy range. We observed three islands of larger ions with slopes of -1 and diffused islands for smaller ions. For the selected energy range, the dication has small internal energy and we expected to see larger fragment ions resulting from two-body breakups[78] with slope of -1 in the AEPIPICO plot. Fig. 4.17 (b) and (c) show the calculated background $BetII(tof_1, tof_2)'$ and the corrected $TetII(tof_1, tof_2)'$ respectively. We observe that once the background ions were removed, the diffused islands (highlighted in red) of smaller fragments vanished, and only the expected *true* ions with slopes -1 are visible in the corrected $TetII(tof_1, tof_2)'$ map.

Ion pair specific Auger electron spectrum

In the 3D data set $etEII(e_{KE}, tof_1, tof_2)$, the electron kinetic energy spectrum can also be written as a function of tof_1 and tof_2.

$$ES_2 = \sum_{all\ tof_1, tof_2} etEII(e_{KE}, tof_1, tof_2) \qquad (4.3.42)$$

For a selected ion pair with a range of $(tof_1,\ tof_2)$, we can plot the electron spectrum for specific selection ion pair $ES_2IIpair(e_{KE})$. The range of $(tof_1,\ tof_2)$ are the islands on the AEPIPICO plot for the selected ion pair, we call this region of interest (ROI) on the AEPIPICO plot. Defining the ROI correctly is important for this data treatment to work.

$$ES_2IIpair(e_{KE}) = \sum_{tof_1, tof_2\ in\ ROI} etEII(e_{KE}, tof_1, tof_2) \qquad (4.3.43)$$

Using the same logic as in equation (4.3.33), we can write the probability of detecting two ions in coincidence with an electron as,

$$\frac{etEII(e_{KE}, tof_1, tof_2)}{N_e} = rtP_0 . \frac{HetEII(e_{KE}, tof_1, tof_2)}{N_e}$$
$$+ \frac{rtI(tof_1)}{N_{RND}} . \frac{HetEI(e_{KE}, tof_2)}{N_e} + \frac{HetEI(e_{KE}, tof_1)}{N_e} . \frac{rtI(tof_2)}{N_{RND}}$$
$$+ \frac{HES_0(e_{KE})}{N_e} . \frac{rtII(tof_1, tof_2)}{N_{RND}} \qquad (4.3.44)$$

The *true* ions data $TetEII(e_{KE}, tof_1, tof_2) = rtP_0 \cdot HetEII(e_{KE}, tof_1, tof_2)$ and $TetEI(e_{KE}, tof_{1,2}) = rtP_0 \cdot HetEI(e_{KE}, tof_{1,2})$, therefore we can write it in terms of $etEII(e_{KE}, tof_1, tof_2)$, using the above equation.

$$TetEII(e_{KE}, tof_1, tof_2) = etEII(e_{KE}, tof_1, tof_2) - \frac{rtI(tof_1) \cdot TetEI(e_{KE}, tof_2)}{N_{RND} \cdot rtP_0}$$
$$- \frac{rtI(tof_2) \cdot TetEI(e_{KE}, tof_1)}{N_{RND} \cdot rtP_0} - \frac{rtII(tof_1, tof_2) \cdot ES_0(e_{KE}) \cdot SC}{N_e \cdot rtP_0}$$

$$(4.3.45)$$

For a specific ion pair with a selected ROI in the AEPIPICO, we can calculate the true electron spectrum as,

$$TES_2IIpair(e_{KE}) = \sum_{tof_1, tof_2 \text{ in ROI}} TetEII(e_{KE}, tof_1, tof_2) \qquad (4.3.46)$$

The random background in the ROI is calculated by rearranging equation (4.3.45),

$$BES_2IIpair(e_{KE}) = ES_2IIpair(e_{KE}) - TES_2IIpair(e_{KE})$$

$$= \sum_{tof_1, tof_2 \text{ in ROI}} \frac{rtI(tof_1) \cdot TetEI(e_{KE}, tof_2) + rtI(tof_2) \cdot TetEI(e_{KE}, tof_1)}{N_{RND} \cdot rtP_0}$$

$$+ \frac{ES_0(e_{KE})}{N_e} \sum_{tof_1, tof_2 \text{ in ROI}} \frac{rtII(tof_1, tof_2) \cdot SC}{rtP_0} \qquad (4.3.47)$$

Fig. 4.18 shows the corrected electron spectrum for $C_2H_5^+/C_8H_{11}^+$ ion pair of core-ionized adamantane. In blue is the experimental measurement $ES_2IIpair(e_{KE})$, the red line shows the calculated background $BES_2IIpair(e_{KE})$, and in yellow is the corrected true spectrum $TES_2IIpair(e_{KE})$. The experimental data has two peaks, at narrow one at about 266 eV and a broad peak at about 250 eV. After the correction, the broad feature is removed, indicating that it was coming from the background ions. Therefore, removal of random coincidences is important for correct physical interpretation of data from the EPICEA setup.
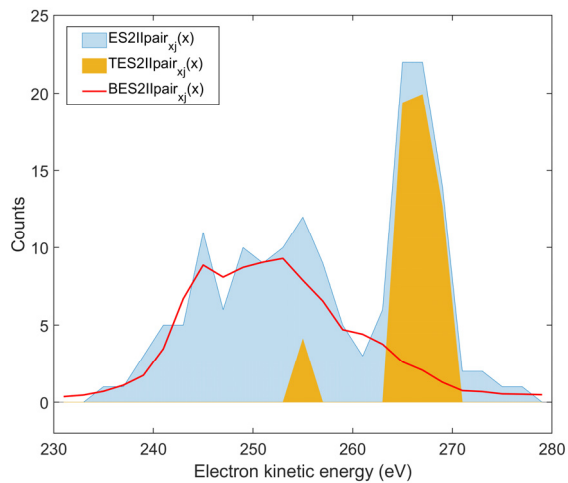
Figure. 4.18 The ion pair specific Auger electron kinetic energy spectrum of the $C_2H_5^+/C_8H_{11}^+$ ion pair produced from core-ionized adamantane recorded at 350 eV photon energy using the EPICEA setup. The experimental data is shown in blue, the calculated background is shown in red line and the corrected true electron spectrum is shown in yellow.

5 Results

This chapter provides a summary of the papers in this thesis, which investigate soft X-ray induced ultrafast dynamics of molecular adamantane and carbon dioxide clusters using electron-ion coincidence spectroscopy. The first section focuses on adamantane fragmentation, which is a complex process influenced by competing relaxation pathways such as hydrogen loss, hydrogen migration, cage opening, and C-C bond breaking. The study used core ionization (**Paper II**) and resonant excitation (**Paper III**) and theoretical calculations to investigate the site-dependent fragmentation of the carbon cage of adamantane. The second section presents a joint experimental and theoretical study on the photoreactions of core ionized CO_2 clusters (**Paper I**). The study found that the production of O_2^+ from CO_2 clusters is significantly enhanced compared to isolated CO_2 molecules, and identified two fragmentation pathways that contribute to this enhancement. The effects of cluster size and geometry on the O_2^+ yield is also explored.

5.1 Ultrafast dynamics of adamantane

Adamantane is the smallest diamondoid with molecular formula $C_{10}H_{16}$ and a carbon cage geometry. All the carbons are sp^3 hybridized and hydrogen-terminated. It has 6 secondary carbon atoms (CH_2) and 4 tertiary carbon atoms (CH) (see Fig. 5.1). In bulk diamonds, these CH and CH_2 types of carbons form the surface. The molecule is highly symmetric and belongs to T_d point group. The ground state electronic configuration of adamantane is:

$$\textbf{(10 C-1s)}^{20}(3a_1)^2(3t_2)^6(2e)^4(4t_2)^6(4a_1)^2\ (5a_1)^2(5t_2)^6(1t_1)^6(6t_2)^6(2t_1)^6(3e)^4(7t_2)^6$$

The ultrafast dynamics of adamantane were studied using synchrotron radiation in for site selective excitation of the C 1s electrons in the molecule. In **Paper II**, adamantane is C 1s ionized using 350 eV photons and then the theoretical Auger spectrum is used to identify which dication states correspond to CH and CH_2 type of carbon. These states are used to investigate site-sensitivity in the fragmentation of the adamantane dication using AEPIPICO spectroscopy. In **Paper III**, the photon energy is tuned to resonantly excite the CH or CH_2 type of carbon in adamantane at 287.1 eV and 287.6 eV respectively. The fragmentation of the cation and dication is discussed and compared for the two site-selective core excitations of adamantane.
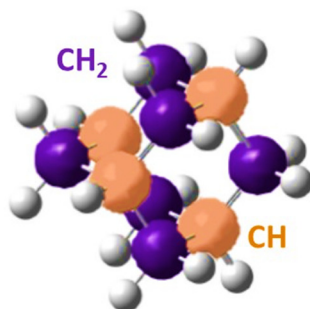
Figure. 5.1 Adamantane molecule with two types of carbon sites CH (highlighted in orange) and CH_2 (highlighted in purple). The core excitation and ionization of these two carbon sites are studied in this section.

5.1.1 Adamantane ions in a nutshell

After absorbing a photon, the adamantane molecules can form excited multiply charged cations. The single, double, and triple ionization thresholds are 9.2 eV, 23.9 eV and 43.6 eV respectively. For photon energies less than 23.9 eV, the valence electrons are ionized and an excited adamantane cation is formed. The adamantane cation $C_{10}H_{16}^+$ in its electronic ground state has a reduced C_{3v} symmetry compared to neutral adamantane due to Jahn Teller distortion[170]. This distorted geometry has three elongated CC σ bonds creating two units C_4H_7 and C_6H_9 and a weakened C-H bond of one of the tertiary carbons. Therefore, the cation readily eliminates an H atom with the weakened C-H bond to form the stable 1-adamantyl cation with C_{3v} symmetry and three elongated C_α-C_β σ bonds. However, the adamantane cation can also lose one H atom from one of the secondary carbons to form the less stable 2-adamantyl isomer. Compared to the neutral geometry, theoretical calculations predict that the 2-adamantyl cation is severely distorted of C_s symmetry with bending of the C_α-C^+-C_α bridge[171,172]. Previous studies have estimated that the cation requires about 1.5 eV and 2 eV for losing an atomic H to form the 1-adamantyl and 2-adamantyl isomers respectively[173,174].

It is observed that the removal of one electron from adamantane leads to preferentially formation of the 1-adamantyl cation[170,175,176], and therefore previous mass spectroscopy studies of the adamantane cation were only able to probe the 1-adamantyl cation[174,177,178]. The mass spectrum of the 2-adamantyl cation has never been reported. Candian et al[174] found that for the 1-adamantyl cation, C_3H_X loss is the dominant fragmentation product for photon energies 11.3 to 12 eV, followed by H and C_4H_Y loss. Hence, the mass spectrum was dominated by the $C_7H_9^+$ ion. They also calculated the potential energy surface (PES) of adamantane cation. The PES calculations show that the carbon cage opens, and one hydrogen migrates to a

secondary carbon forming CH_3 termination before further fragmentation of the cation. This cage opening of the cation has a small energy barrier of 1.62 eV[174].

It is worth noting that the adamantane cation can also lose H_2 instead of atomic H losses, Kappe et al[179] calculated that the pathways involving H_2 loss are less energetically demanding than H loss for the cation for the first 3 hydrogen losses but there is no experimental evidence of H_2 loss from the singly charged cation.

For photon energies above 23.9 eV, the adamantane can lose two valence electrons to form $C_{10}H_{16}^{2+}$. The dissociation of the adamantane dication after valence ionization has been studied using XUV femtosecond pulses[78,178]. The PES calculations of adamantane dication found that it dissociates via barrier-less cage opening[78] in the femtosecond timescale and the lowest energy configuration has an open-cage geometry with at least one CH_3 termination which is not present in the ground state adamantane. After double valence ionization, the molecule spontaneously dissociates and the two body breakup into $C_2H_5^+/C_8H_{11}^+$ was reported as the dominant channel[78].

Statistical fragmentation simulations of relaxation of $C_{10}H_{16}^{2+}$ show that the C-C bond breaking also strongly depends on the internal energy of the dication[78]. For internal energies less than 4 eV the dication mainly breaks up into two charged fragments, creating ion pairs like $C_2H_5^+/C_8H_{11}^+$, $C_4H_7^+/C_6H_9^+$, $C_3H_6^+/C_7H_{10}^+$ and $C_3H_5^+/C_7H_{11}^+$ with no hydrogen loss. Whereas for energies larger than 4 eV (up to 10 eV) the dication breaks up into two charged fragments and one neutral fragment.

In hydrocarbon dications, dehydrogenation reactions of H/H_2 loss are common to 'cool' the molecule and prevent the carbon backbone fragmentation into two singly charged hydrocarbons[180]. Milko et al[181] studied the general trends in the dissociation of hydrocarbon dications $C_mH_n^{2+}$ and found that for smaller hydrocarbons H/H_2 loss are major dissociation channels. They also suggested that dications with even number of hydrogens and carbons (i.e., m and n are even) prefer H_2 loss over H loss. This would imply that the adamantane dication with m=10 and n=16, should preferentially eliminate H_2. The neutral H_2 loss cannot be measured experimentally yet. No hydrogen loss calculations are available so far for the adamantane dication, however by comparing to other hydrocarbon dications[182–184], the adamantane dication might also prefer H_2 loss over H loss.

Therefore, the ultrafast dynamics of adamantane cation and dication may involve cage opening and hydrogen migration before fragmentation. This section presents the first study of the fragmentation pathways of core-excited and ionized adamantane.

5.1.2 Electronic relaxation after core excitation and ionization

The binding energies of the C-1s core orbitals of adamantane of the CH and CH_2 sites show a chemical shift of about 200 meV confirmed by XPS measurements and theoretical calculations. Also, the C-1s core molecular orbitals of adamantane are well localised on the CH and CH_2 type of carbons (see Paper II). This makes the adamantane molecule suitable for site selective core-excitation studies of the CH and CH_2 sites.
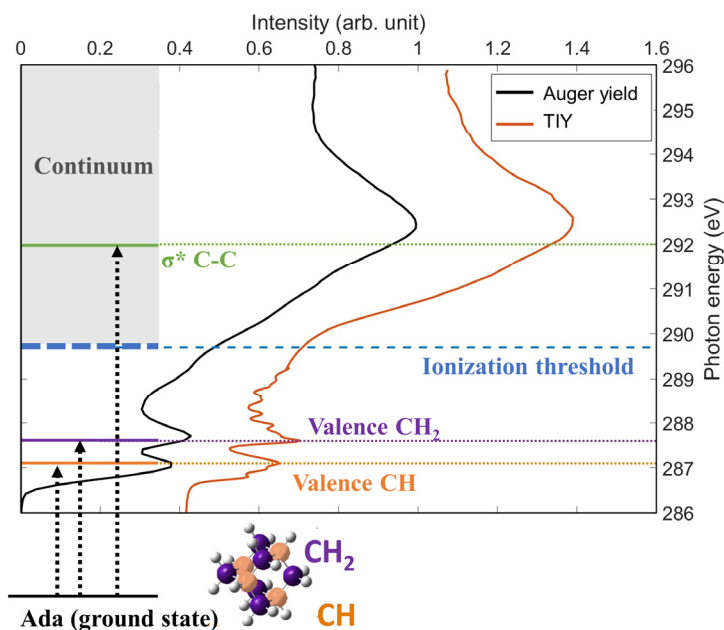
Figure. 5.2 Near C 1s edge features of adamantane using Auger yield NEXAFS (black line) and Total ion yield (TIY) NEXAFS (red) measurements. The ionization threshold of adamantane is about 289.7 eV. The pre-edge resonances are assigned to CH and CH_2 valence states. The vibrational modes of the C-H bond are visible in the higher-resolution TIY spectrum. Above the edge, a broad resonance at 292 eV is assigned to σ* states of the C-C bonds.

For core excitation studies, it is necessary to first identify the resonant features near the C 1s ionization edge. We measured Auger yield Near edge X-ray absorption spectrum (NEXAFS) shown in Fig. 5.2 using a wide-angle lens VG-Scienta R4000 hemispherical electron energy analyzer and cleaned the data to remove the overlap of photoelectron spectrum as described in the data analysis chapter. We observe two sharp resonances below the ionization threshold and a broad resonance above the threshold. The pre-edge features in hydrocarbons often have a mixed Rydberg-valence character due to C-H bonds[185,186]. In previous studies, the sharp resonances at 287.1 eV and 287.6 eV are related to valence CH and CH_2 type orbitals by

comparing them to diamond clusters[187] and other carbon cage molecules[188]. The broad resonance at 292 eV is attributed to σ* states of the C-C bonds[187,188]. We also measured the total ion yield (TIY) spectrum using the EPICEA setup in a continuous ion extraction field mode with higher photon energy resolution (30 meV) to resolve the vibrational modes of the C-H bonds[187,188]. These unoccupied virtual valence states of the C-H bonds are expected to be localized on specific carbon sites[188]. Therefore, we select these two resonances of C 1s→ CH and C 1s→ CH_2 valence orbitals for site-selective fragmentation studies between the two carbon sites of adamantane.

Another approach of confirming if the nature of these pre-edge orbitals is valence-like uses Resonant Auger electron energy spectrum (RAES). Using tunable synchrotron radiation, we selectively created a core hole in either CH or CH_2 type of carbon in adamantane using the photon energies for the resonances discussed in the previous section. Fig. 5.3 and 5.4 show the RAES for the three C 1s resonances observed in NEXAFS of adamantane, namely, C 1s→ CH, C 1s→ CH_2 and C 1s→ σ* C-C excitations. From the resonant Auger electron spectrum (RAES), one can interpret the character of the pre-edge orbital occupied by the excited electron. If this pre-edge orbital is valence-like then the molecule is more likely to undergo participator Auger decay than if the orbital is Rydberg-like[189,190,191].

To identify the participator decay states in the RAES we plot the spectrum in binding energy scale i.e., photon energy minus the measured Auger electron energy as shown in Fig. 5.3. In this representation, we see the direct assignment of the peaks by comparing them to the off-resonance valence ionization spectra (black line). After participator Auger decay the molecule relaxes to a cationic state identical to the valence ionized states, therefore the kinetic energy of the Auger electron increases linearly with photon energy. We observe that the molecule is more likely to undergo participator Auger decay after C 1s→ CH valence orbital excitation than the C 1s→ CH_2 valence orbital excitation. Therefore, even though the final state after Auger decay is energetically close to the valence ionized states, we observe that the probability of reaching these states via participator decay is site-selective.

Some studies have suggested that if the ratio between the participator Auger decay to the total Auger decay is less than about 5% then the excited pre-edge orbital is diffused Rydberg-like[186,192]. The relative intensity (I_{PA}) of the participator peaks is about 23.4% and 16.5% for C 1s→ CH valence and C 1s→ CH_2 valence orbital excitations respectively. As for both the resonance excitations I_{PA} is much greater than 5%, we interpret that these pre-edge orbitals have negligible Rydberg mixing, as predicted in previous studies[187,188].

Figure. 5.3 Identification of participator Auger decay states in adamantane, (a) shows the experimentally measured resonant Auger electron energy spectrum (RAES) for the C 1s→ σ* C-C excitation at 292 eV (in green), C 1s→ CH$_2$ valence orbital at 287.6 eV (in purple) and C 1s→ CH valence orbital at 287.1 eV (in orange). The direct valence ionization spectrum is also shown for off-resonance photon energy at 285 eV. The vertical blue lines show the valence ionization threshold for single (IT$_1$), double (IT$_2$) and triple (IT$_3$) ionization at 9.2 eV, 23.9 eV and 43.6 eV respectively. (b) shows a schematic of participator Auger decay leading to the final cation state of 7t$_2^{-1}$ lying at binding energy of 9.8 eV in (a).

The energy levels of the valence states (vertical lines in Fig. 5.3) are taken from literature on valence ionization studies of adamantane[193,194]. The schematic to the right in Fig. 5.3 visualizes the energy levels for creating the 7t$_2^{-1}$ state, the dominant peak in RAES of C 1s→ CH core resonant excitation. Among these participator decay states we observe that 3t$_2^{-1}$, 2e^{-1} and 4t$_2^{-1}$ states are more probable than others. The outer valence states 7t$_2^{-1}$, {2t$_1$ + 3e}$^{-1}$ and {1t$_1$ + 6t$_2$}$^{-1}$ are slightly more intense for C 1s→ CH valence orbital excitation. The small shift in the binding energy of the peaks in the RAES compared to the valence spectrum can be due to decay into higher vibrational states, suggesting that ultrafast dynamics can occur in the core excited state. Although there is no peak in the RAES, the intensity for the 3a$_1^{-1}$ state at 27.1 eV appears to be enhanced for these resonant excitations below the second valence ionization threshold (IT$_2$), but this could be due to the overlap of spectator decay states. To identify the 3a$_1^{-1}$ state, we plot the same data as in Fig. 5.3 in the electron kinetic energy scale in Fig. 5.4.
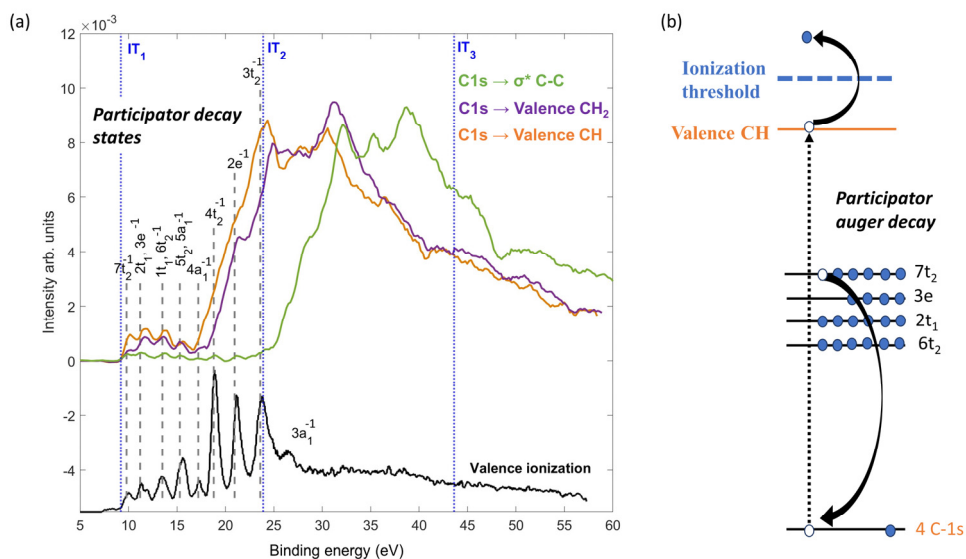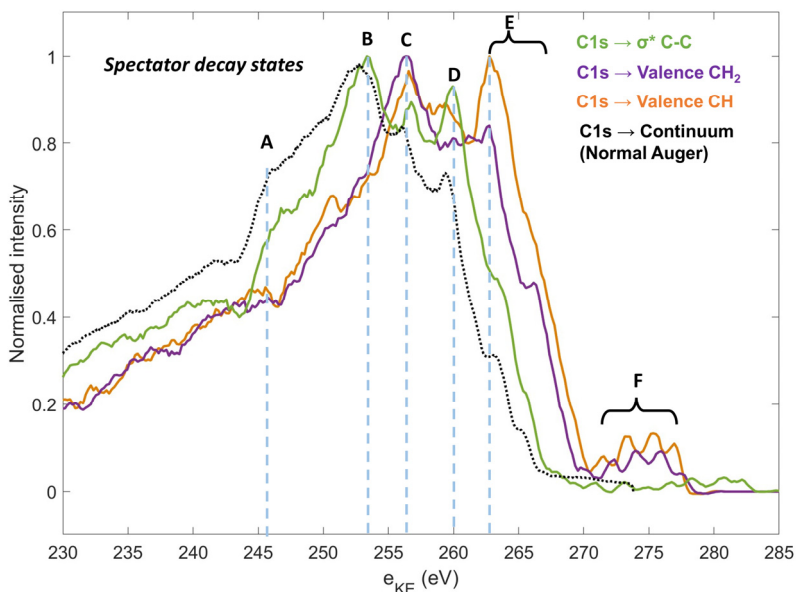
Figure. 5.4 Identification of spectator Auger decay states in adamantane, the experimentally measured resonant Auger electron energy spectrum (RAES) for the C 1s→ CH valence orbital at 287.1 eV (in orange), the C 1s→ CH$_2$ valence orbital at 287.6 eV (in purple) and the C 1s→ σ* C-C excitation 292 eV (in green). The normal Auger spectrum of C 1s ionization at 350 eV ionization spectrum is also in black dotted lines. The labels A, B, C, D, E and F are described in the text.

In Fig. 5.4 we identify the features in the RAES coming from spectator Auger decay; these features are independent of the excitation photon energy. Therefore, we can compare the below and above-threshold resonant excitations with the normal Auger decay spectrum. We label features A, B, C, D, E and F at different Auger electron energies, each feature has contributions from multiple electronic states. The above threshold resonance excitation C 1s→ σ* C-C should only undergo spectator decay; the states A, B and C are thus a result of spectator decay. The state D however is more complicated, as it overlaps with the $3a_1^{-1}$ participator state, but because D is also present in the C 1s→ σ* C-C excitation and normal Auger decay, the major contribution comes from spectator Auger decay here. Similarly, the feature E is assigned to $3t_2^{-1}$, $2e^{-1}$ and $4t_2^{-1}$ states but E also has a small contribution from the spectator decay states as it's also present in the normal Auger decay. The feature F is unambiguously assigned to the $7t_2^{-1}$, $\{2t_1 + 3e\}^{-1}$, $\{1t_1 + 6t_2\}^{-1}$, $\{5t_2 + 5a_1\}^{-1}$ and $4a_1$ states and has 'pure' participator decay contributions because F is absent in the C 1s→ σ* C-C excitation and normal Auger decay.

5.1.3 Fragmentation of adamantane with soft X-rays

In large molecules, the fragmentation processes often depend on the magnitude of the excess internal energy[81,82] after electronic relaxation of the core-hole state and lead to statistical fragmentation of the molecule. Thus after Auger decay, the excess energy of the molecule undergoes delocalization and the memory of the core hole site is essentially lost[195]. However, if the excess energy of the molecule can remain localized, in this case the fragmentation of the molecule strongly depends on the site of the core-hole[196]. It was recently shown that the smallest polyene hydrocarbon, butadiene, exhibits site-specific fragmentation[85]. Interestingly, the RAES of butadiene are strongly site specific, which is in line with our observation for adamantane. We are thus interested to investigate whether there is memory of the initial excitation/ionisation site in adamantane and if it leads to site-specific fragmentation.

Cation fragmentation

The core-hole memory[84] of the cationic state created after participator decay is studied by resonantly exciting the tertiary (CH) or secondary (CH_2) carbon sites in adamantane. We select three sets of valence states in the RAES highlighted in Fig. 5.5 (a), green for the states $7t_2^{-1}$, $\{2t_1 + 3e\}^{-1}$ and $\{1t_1 + 6t_2\}^{-1}$, blue for the $\{5t_2 + 5a_1\}^{-1}$ states and yellow for the $4a_1^{-1}$, $3t_2^{-1}$, $2e^{-1}$ and $4t_2^{-1}$ states. Fig. 5.5 (b) shows the Auger electron-photoion coincidence (AEPICO) filtered mass spectrum of the ions created after fragmentation of adamantane cation following participator Auger decay for the hole created in different selected valence states. In the AEPICO data, when the Auger electron has high kinetic energy, it indicates that lower binding energy MOs were involved in the Auger decay with small internal energy in the nuclear degree of freedom.

After C 1s$\rightarrow$ CH valence orbital excitation followed by Auger decay, when a hole is created in the outer-most valence orbitals (green in Fig. 5.5 (a)) of adamantane, we observe a peak at 136 a.u. in the mass spectrum corresponding to the mother ion $C_{10}H_{16}^+$ or the adamantyl cation $C_{10}H_{15}^+$. However, for the C 1s$\rightarrow$ CH_2 valence orbital excitation case, we see no sign of the mother ion in the mass spectrum. For both resonances, the molecule breaks up into smaller hydrocarbons with a dominance of $C_3H_5^+$ and $C_6H_7^+$. The appearance energy of $C_6H_7^+$ from adamantane is reported as 10.69 eV in the NIST database which lies in the range of green selection.
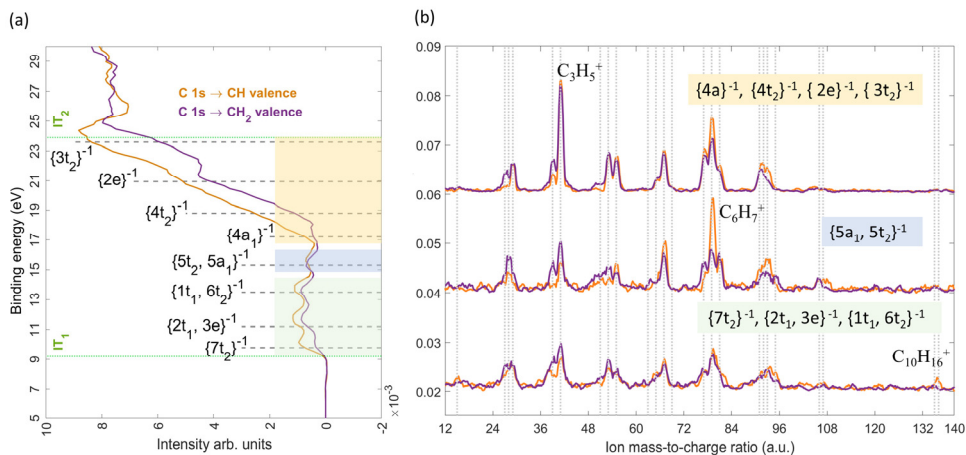
Figure. 5.5 Site-selective fragmentation of adamantane after participator Auger decay. (a) shows the zoomed in RAES data from Fig. 5.3 for the C 1s→ CH valence orbital at 287.1 eV (in orange) and the C 1s→ CH$_2$ valence orbital at 287.6 eV (in purple) with cation state assignment (dotted grey lines). The horizontal dotted green lines show the valence ionization threshold for single (IT$_1$) and double (IT$_2$) ionization at 9.2 eV and 23.9 eV respectively. (b) shows the ions detected in coincidence with the Auger electrons assigned to 7t$_2$$^{-1}$, {2t$_1$ + 3e}$^{-1}$ and {1t$_1$ + 6t$_2$}$^{-1}$ states in bottom row, {5t$_2$ + 5a$_1$}$^{-1}$ states in middle row and the 4a$_1$$^{-1}$, 3t$_2$$^{-1}$, 2e^{-1} and 4t$_2$$^{-1}$ states in top row for the CH site (in orange) and CH$_2$ site (in purple). The selected Auger electron energy ranges below IT$_2$ for filtering the electron-ion coincidence data (AEPICO) are highlighted in (a) in light green, blue and yellow.

For the {5t$_2$ + 5a$_1$}$^{-1}$ states, we observe an enhancement of the C$_6$H$_7$$^+$ signal for the C 1s→ CH valence orbital excitation. This suggests that the {5t$_2$ + 5a$_1$}$^{-1}$ state geometry is distorted like 1-adamantyl, this creates two units C$_4$H$_7$ and C$_6$H$_9$ and which easily breaks into C$_6$H$_7$$^+$ and neutral C$_4$H$_8$. Electron ionization[177] and XUV ionization[178] studies of adamantane have previously reported C$_6$H$_7$$^+$ as the dominant ion. Mass spectrometry-based infrared multiple photon dissociation (IRMPD) studies of adamantane identified the C$_6$H$_7$$^+$ fragment as protonated benzene[177]. For the C 1s→ CH$_2$ valence orbital excitation, the mass spectrum for the {5t$_2$ + 5a$_1$}$^{-1}$ states look like the 7t$_2$$^{-1}$, {2t$_1$ + 3e}$^{-1}$ and {1t$_1$ + 6t$_2$}$^{-1}$ states with no enhancement in C$_6$H$_7$$^+$ yield. For the CH site excitation, the intensity of C$_3$H$_3$$^+$, C$_4H_3$$^+$, C$_4H_5$$^+$ and C$_6$H$_5$$^+$ is negligible compared to the CH$_2$ site. The CH site excitation results in fragments with a higher number of hydrogens attached than the CH$_2$ site, thus being an unfavorable resonance excitation for hydrogen loss.

For the inner-most valence 4a$_1$$^{-1}$, 3t$_2$$^{-1}$, 2e^{-1} and 4t$_2$$^{-1}$ states i.e., feature F of Fig. 5.4, we expect contributions from both participator (1h state) and spectator (2h-1p state) Auger decay. Hence, the ions in coincidence with this energy range are created by the fragmentation of the cation and possibly the dication. In the mass spectrum for these states, we observe an increase in the abundance of the C$_3$H$_5$$^+$ ion for both the resonant excitations. Boyer et al. reported an increase in C$_3$H$_5$$^+$ for dication

dissociation using XUV photons of 30-33 eV compared to the cation dissociation using XUV photons of 17-23 eV[178]. Thus, this indicates we have 2h-1p states in this energy range, which can decay by autoionization of the molecule leading to the breakup of the dication. The $C_6H_7^+$ intensity remains higher for the C 1s→ CH valence orbital excitation than the C 1s→ CH_2 valence orbital excitation for these higher binding energy states too.

While the localization of charge in the cation after participator Auger decay is not obvious, our results show some clear differences in the fragmentation of the molecule especially in the yield of $C_6H_7^+$ for the two resonant excitations, indicating the influence of core-hole site[197]. This could be an insignia of core-hole memory after participator decay and creation of localized valence holes on the either CH-type or CH_2-type of carbon i.e., selectively creating 1-adamantyl or 2-adamantyl cations.

Dication fragmentation

Resonant spectator Auger decay leads to a cationic state (2h-1p), with two holes in the valence orbitals and an excited electron in the higher valence orbitals discussed in Fig. 5.2. This excited cationic state usually autoionizes to form a dicationic state. Normal Auger decay also leads to a dicationic state with two holes in the valence orbitals without any excited electron. After Auger decay, the dication state will be significantly different from that reached after double valence ionization as the molecule will have high internal energy. In Paper II, indirect site-sensitivity for the CH and CH_2 sites in fragmentation of the dication after Normal Auger decay is reported.

In the C 1s ionization experiment we can ionize either the CH or CH_2 sites, therefore the site-sensitivity in fragmentation can only be studied indirectly. Fig. 5.6 (a) and (b) show the AEPIPICO plot for C 1s ionization of the CH and CH_2 sites respectively. The theoretical Auger electron spectrum (AES) is calculated for normal Auger decay of C 1s core-hole created in CH and CH_2 sites (see Paper II for details). The electron kinetic energies corresponding to these theoretical CH and CH_2 bands in the AES are used to filter the experimental AEPIPICO. Comparing Fig. 5.6 (a) and (b), we observe that the AEPIPICO plot for CH site ionization has more ions pairs containing $C_2H_5^+$ and $C_3H_5^+$ than the CH_2 site ionization. Ionizing the CH_2 type of carbon favors hydrogen loss while the CH type results in fragment ions with more hydrogens attached. The dominant ion pair for both the sites is the asymmetric ion pair $C_2H_3^+/C_3H_3^+$, followed by $C_3H_3^+/C_3H_3^+$, $C_3H_5^+/C_3H_5^+$ and $C_2H_3^+/C_2H_3^+$ ion pairs. There is a significant difference in the intensities of the larger fragment ion pairs for the two sites, with an enhancement in the two-body breakup into $C_2H_5^+/C_6H_{5,7}^+$ and $C_2H_{3,5}^+/C_7H_7^+$ for the CH site.
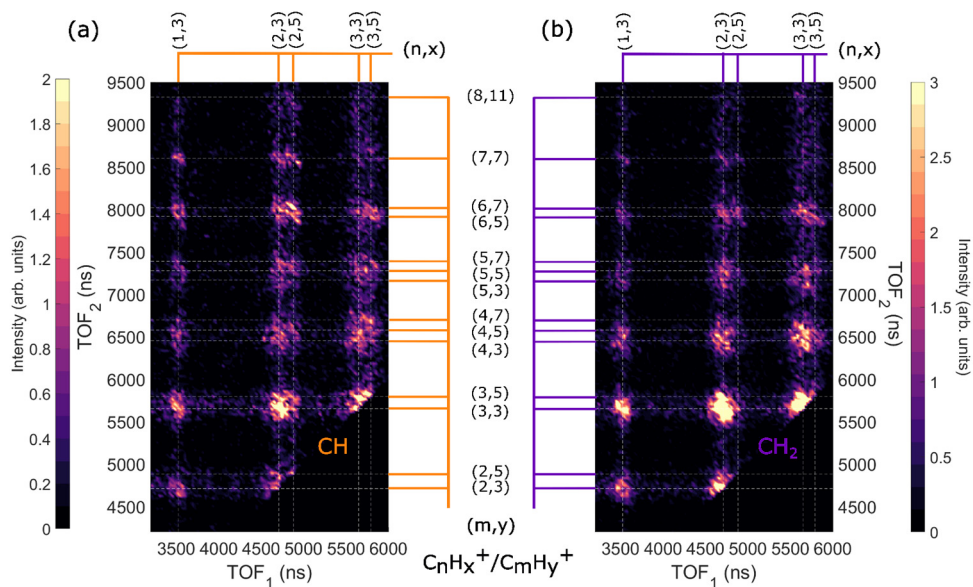
Figure. 5.6 Auger electron photo-ion photo-ion (AEPIPICO) data of adamantane for the C 1s ionization at 350 eV. The theoretically calculated Auger electron spectrum is used to filter the ion pairs detected in coincidence with the C 1s ionization of the CH site in (a) and the CH_2 site in (b). The AEPIPICO shows the ion pairs measured in coincidence i.e. the ions created in the same ionization event. The data has been filtered to remove false coincidence using method described in Data Analysis chapter. The colormaps have been normalized to maintain the $4:6$ ($4CH:6CH2$) ratio that we expect in the adamantane molecule.

We also performed direct site selection of CH or CH_2 site by resonant core excitation of adamantane. In the resonant core excitation study, we found no evidence of site-dependent fragmentation of the adamantane dication for the CH and CH_2 sites. This could be due to low statistics in the experimental measurement. However, the ion mass-to-charge spectrum (see Paper III) of adamantane dication fragmentation after core excitation and core ionization shows significant difference. Core ionization of both the sites produces more ion pairs containing CH_3^+ than core excitation. The CH_3 type of carbon does not exist in neutral adamantane, and is formed after hydrogen migration and cage opening of adamantane[78]. The difference in CH_3^+ yield might imply that the cage opening of the dication after these resonant excitations does not necessarily involve hydrogen migration. Therefore, the dicationic states of adamantane reached after spectator Auger decay and normal Auger decay undergo different fragmentation pathways.

5.1.4 Hydrogen motion in adamantane

Theoretical calculations show that the dissociation of the adamantane cation and dication start with cage opening and hydrogen migration in the molecule[78,174]. The AEPIPICO plots for C 1s ionization (see Fig 5.6 (a) and (b)) show the abundance of the methyl cation (CH_3^+). This provides evidence of hydrogen migration before fragmentation of the adamantane dication because the methyl group does not exist in neutral adamantane. Along with hydrogen migration, hydrocarbons can dehydrogenate i.e., emit neutral hydrogens to dissipate the excess energy. In general, hydrocarbons are known to fragment via multiple competing processes like C-C bond breaking, atomic hydrogen or molecular hydrogen (H_2) emission or C_2H_2 emission[85,181,198–201]. For adamantane, there is clear indication of C-C bond breaking for both the CH and CH_2 sites, and no sign of C_2H_2 emission. The adamantane cation is known to lose one hydrogen to form the stable 1-adamantyl cation[170,175,176]. We also observed that CH_2 site ionization triggers more hydrogen loss from the dication than the CH site in adamantane. In this section, hydrogen loss (H or H_2) from adamantane is explored using AEPICO spectroscopy.

Hydrogen loss

The AEPICO data of adamantane follows the general trend that the number of hydrogens attached to the ion fragment is correlated to the Auger electron energy. This effect is shown in Fig. 5.7 for the CH site excitation, similar trends are found for the CH_2 site excitation and the C 1s ionization. The kinetic energy of the Auger electrons detected in coincidence with fragments $C_nH_r^+$ of different sizes (n) have the same distribution if they have the same number of hydrogens (r) attached. Fig. 5.7 (a), (b), (c) and (d) shows this effect for different values on $r = 3, 5, 7$ and 9 respectively for various values of n. For a given value of lost hydrogens r, the peak position is almost constant for different values of n. Interestingly, this trend is valid for the cation (above IT$_1$) and the dication (above IT$_2$). One possible explanation is that the hydrogen loss precedes C-C bond breaking i.e., the charged mother ion first loses hydrogens and then undergoes further fragmentation. In such a case, the number of hydrogens lost depends on the final state reached after Auger decay, irrespective of the size (n) of the fragment ions.
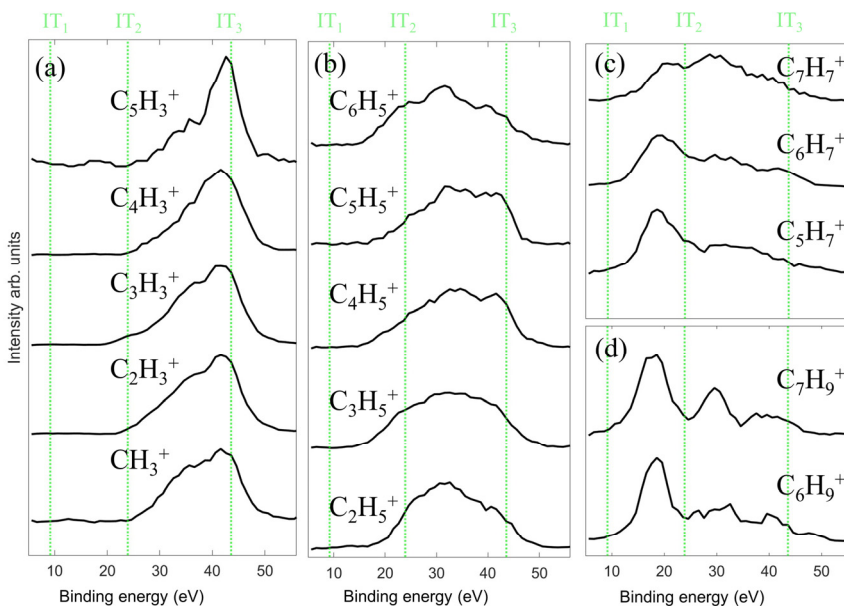
Figure. 5.7 Ion specific binding energy spectrum from the AEPICO data for the C 1s→ CH valence orbital excitation, shown in binding energy calculated as (hv - e_{KE}) where hv is the photon energy and e_{KE} is the Auger electron energy. The spectras are grouped according to the number of hydrogens attached to the ion fragment $C_n H_r^+$, for (a) $r = 3$, (b) $r = 5$, (c) $r = 7$ and (d) $r = 9$. The vertical green lines show the valence ionization threshold for single (IT_1), double (IT_2) and triple (IT_3) ionization at 9.2 eV, 23.9 eV and 43.6 eV respectively.

To estimate the energy needed for hydrogen loss in adamantane, we plot the average internal energy levels of ion fragments ($C_n H_r^+$) against the amount of hydrogen loss (x), where $x = 16 - r$. Fig. 5.8 shows the hydrogen loss for C 1s→ CH valence orbital excitation, C 1s ionization and C 1s→ CH$_2$ valence orbital excitation in (a), (b) and (c) respectively. The internal energy distributions of the ion fragments are very broad, so their standard deviations are represented as error bars. The internal energy distribution is calculated with reference to the neutral adamantane ground state. For the core excitation case in Fig. 5.8 (a) and (c), the internal energy is calculated as $hv - e_{KE}$, where hv is the photon energy and e_{KE} is the Auger electron kinetic energy. For the core ionization case in Fig. 5.8 (b), the internal energy is calculated as $(E_b(C\ 1s\ e^-) - e_{KE})$ where $E_b(C\ 1s\ e^-)$ is the binding energy of the C 1s electron of adamantane is about 290 eV (from the XPS data reported in Paper II). The data presented here is taken from AEPICO where only one ion was measured, but Fig. 5.8 (a) and (c) have contribution from the adamantane cations and dications for all the ions shown, whereas (b) only has contribution from the adamantane dications.
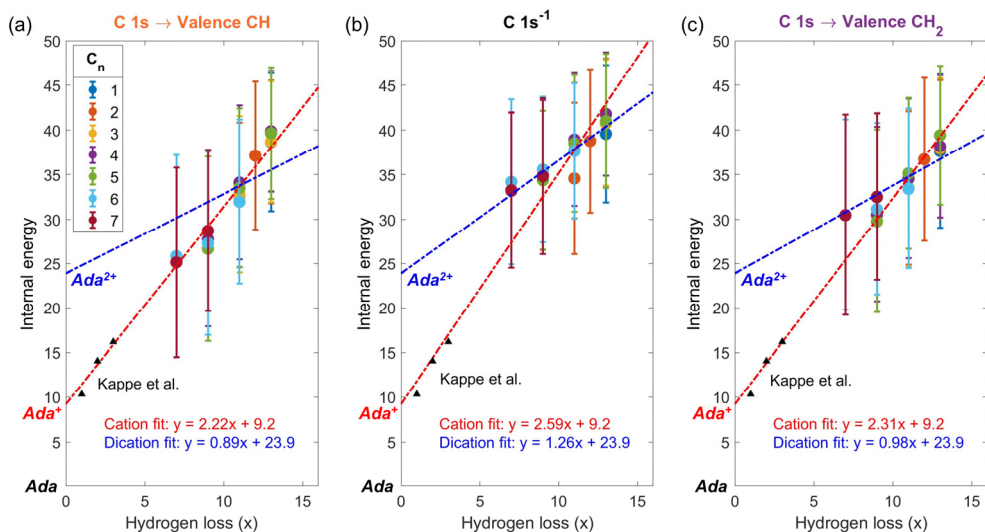
Figure. 5.8 Plot showing the internal energy dependence of hydrogen loss in adamantane for (a) C 1s→ CH valence orbital excitation at 287.1 eV, (b) C 1s ionization at 350 eV and (c) C 1s→ CH$_2$ valence orbital excitation at 287.6 eV. For the ion fragment $C_nH_{16-x}^+$, the statistical mean of the internal energy distributions is shown as a function of the hydrogen loss (x) for different values of n. The error bars show the width of the measured Auger electron binding energy distributions. The ion specific internal energy distributions are calculated from the AEPICO data using the relation (hv - e$_{KE}$) where hv is the photon energy and e$_{KE}$ is the Auger electron energy for (a) and (c). For (b) the internal energy is calculated as E$_b$(C 1s e$^-$) - e$_{KE}$, where E$_b$(C 1s e$^-$) is the binding energy of the C 1s electron is about 290 eV. The dashed lines show the linear fitted function to the experimental data with fixed intercepts at IT$_1$ (in red) and IT$_2$ (in blue). The theoretically calculated[179] hydrogen loss values for the adamantane cation are also shown in black triangles.

A linear regression analysis was performed on the experimental data for the CH site excitation in Fig. 5.8 (a). The analysis had two fixed Y-intercepts on the internal energy axis: 9.2 eV (IT$_1$) for the cation contribution and 23.9 eV (IT$_2$) for the dication contribution. The results showed that for the cation, the linear regression that fit the experimental data the best was y = 2.22 x + 9.2. This suggests that on average, an excess energy of 2.22 eV is required for each hydrogen loss during the CH site excitation. The process of hydrogen loss from adamantane can be atomic H or molecular H$_2$ emission. Theoretical calculations by Kappe et al[179] showed that H$_2$ loss from adamantane cation is energetically favorable over atomic H loss. However, the theoretical successive atomic H losses (black triangles in Fig. 5.8 (a)) agree with the experimental data and the linear regression. This suggests that site-selective excitation to the CH valence orbital favors H loss over H$_2$ loss. A similar effect was observed in propane for C 1s→ CH σ* excitation[200]. We conclude that for the CH site excitation in adamantane, each hydrogen loss requires an excess energy of 2.22 eV and the pathway for hydrogen loss is likely to be H loss.

For the C 1s ionization in Fig. 5.8 (b), all the ions shown are fragments of the dication. The dication linear regression with a fixed Y-intercept of 23.9 eV fits the experimental data with a slope of 1.26 eV. Referring to the general trend of dications favouring H_2 loss[181], the dication fit might give the energetics of H_2 loss in adamantane. In this case, both H and H_2 loss are possible pathways, each H loss will require 1.26 eV and H_2 loss will require 2.52 eV.

For the CH_2 site in Fig. 5.8 (c), the average internal energy differs significantly from that of the CH site in Fig. 5.8 (a). The dication linear regression with a slope of 0.98 eV fits the experimental data better, however, some data points match with the cation linear regression with a slope of 2.31 eV. Therefore, for the CH_2 site in adamantane, we observe that both H and H_2 loss are possible, with each hydrogen loss requiring excess energy of 0.98 eV or 2.31 eV. Therefore, the general trend for hydrogen loss in adamantane is distinct for the CH and CH_2 site excitations and the C 1s ionization.

5.2 Intermolecular reactions in CO_2 clusters

Clusters studies improve our fundamental understanding intermolecular interactions as matter evolves from a single molecule to an infinite solid. Small molecular clusters have unique chemical properties distinct from free molecules and solids that change with increasing cluster size and changing geometry. The existence of intermolecular interactions within these clusters generates a rich environment for the complex relationship between geometry and intra-cluster chemistry.

When a molecular CO_2 cluster is exposed to a soft X-ray photon with sufficient energy, it ionizes the cluster and ejects an inner-shell electron. Following this, the cluster relaxes via Auger decay, resulting in the creation of a cluster ion with multiple charges[202]. The stability of the cluster ion is primarily dependent on its size, and if the cluster is smaller than the critical size it dissociates to reach energetic stability[92,94]. Previous research[203–206] has demonstrated that the dissociation of small multiply-charged CO_2 cluster ions can result in the formation of O_2^+ and these studies attributed collision and recombination processes of O^+ with surrounding CO_2 molecules in the cluster to form O_2^+. However, these processes were not well understood. In this section, a detailed study of soft X-ray induced dissociation of CO_2 cluster ions into O_2^+ is done and a deeper understanding of the fragmentation processes is presented.

The fragmentation processes of core ionized CO_2 clusters are studied in **Paper I** using 3D momentum imaging of ions in combination with PEPIPICO spectroscopy by tuning the cluster sizes. The CO_2 clusters were produced by adiabatic expansion through a conical nozzle. The cluster beam used in the experiment was composed of a mixture of free neutral CO_2 molecules and clusters, with a mean cluster size

N_{mean}. The cluster beam was overlapped with soft X-ray beam from the synchrotron at the interaction region of a 3D momentum imaging mass spectrometer[126]. The soft X-ray photon energy was kept constant at 320 eV for all the results shown in this section. After absorbing a 320 eV photon, the C 1s electron of a molecule in the cluster is ionized and a photoelectron of energy of about 20 eV is emitted. The highly unstable core hole is then filled by Auger decay, resulting in doubly charged cluster ion or further electron loss leading to multiply-charged cluster ion. The stability of the dication depends on the cluster size and the critical cluster size for CO_2 clusters to form stable dication[94] is known to be $(CO_2)_{44}^{2+}$. Clusters smaller than this critical size, dissociate to form singly charged fragment ions.

The coincidence data was recorded using the photoelectron detection as a trigger for detecting each cluster's ion fragments independently and the photoelectron energy was not recorded. The cluster size distribution in the cluster beam is tuned by changing the stagnation pressure of the CO_2 source, and N_{mean} is estimated using empirical relationship[157] for adiabatic expansion of CO_2. Note that the actual cluster size distributions in the cluster beam follows a lognormal distribution[207,208], therefore the fragment ions shown here are coming from a range of cluster sizes, with most likely the mother cluster ion having size N_{mean}.

5.2.1 Ion fragments and increase in O_2^+ yield

Fig. 5.9 shows the mass-to-charge ratio (m/q) of the fragment ions of C 1s ionized CO_2 clusters for N_{mean} of about 4 to 94 molecules. Overall, we observe that the intensity of the cluster fragments $(CO_2)_n^+$ where n = 1, 2, 3, … increases as the cluster size increases. For $N_{mean}\sim4$, the dominant ions are $C^+, O^+, CO^+, CO_2^+, CO_2^{2+}$ which are fragments of the molecular CO_2 background in the cluster beam. The ion peak CO_2^+ can have contributions from the molecular and the cluster part of the beam and can be distinguished by looking at the momentum distribution of the ion. If the CO_2^+ is a molecular fragment, then it has a sharp TOF distribution, indication low kinetic energy. Whereas for the cluster, the CO_2^+ fragment will have a broad TOF distribution due to the non-zero kinetic energy gained when the cluster fragments. The other cluster fragments observed are CO_2CO^+ and $(CO_2)_2^+$. The signal for O_2^+ (indicated by red dotted line in Fig. 5.9) is very small at this cluster size.

For $N_{mean}\sim11$, there is a significant increase in the intensity of the cluster fragments and larger fragments $(CO_2)_n^+$ where n = 3 to 10 appear in the spectrum. For $N_{mean}\sim20$ to 94, yield of O_2^+ remains high and the characteristic three peak structure[203,204,206,209] of the CO_2 clusters fragments appears for the ions $(CO_2)_nO^+$, $(CO_2)_nCO^+$ and $(CO_2)_nO_2^+$. For $N_{mean}\sim94$, the largest singly charged cluster fragment recorded is $(CO_2)_{41}^+$ and the stable dication $(CO_2)_{44}^{2+}$ is also observed in the mass spectrum.

Free doubly-charged CO_2 molecules can undergo bond rearrangement to form covalent bonds between the O atoms followed by two-body Coulombic explosion into O_2^+/C^+. However, the probability of this pathway leading to O_2^+ production from CO_2 molecules is below 1% at this photon energy[67]. The step increase in the yield of O_2^+ with increasing cluster size shows that the fragmentation pathway leading to O_2^+ production is clearly distinct for CO_2 clusters than that observed for free CO_2 molecules. This can be indicative of activation of new fragmentation mechanisms that are exist only in the larger clusters $N_{mean} \geq 4$. These fragmentation mechanisms of core ionized CO_2 clusters that lead to strong enhancement of the O_2^+ yield is further explored using ion-ion coincidence mapping.
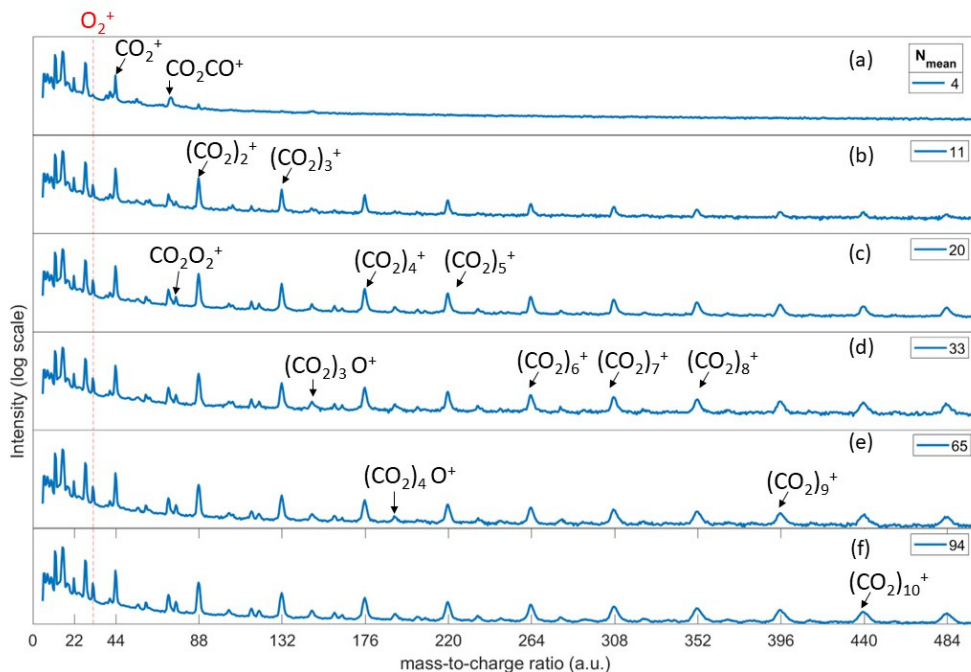
Figure. 5.9 The mass-to-charge (m/q) spectrum of ions produced from C 1s ionized CO_2 clusters for mean clusters sizes N_{mean} of about 4 in (a), 11 in (b), 20 in (c), 33 in (d), 65 in (e) and 94 in (f). The photon energy was kept constant at 320 eV. The red vertical line at m/q = 32 a.u. emphasises the change in O_2^+ yield for increasing cluster sizes.

5.2.2 Ion-ion coincidence mapping

The ion-ion coincidence map (PEPIPICO) of the ion pairs relevant to the O_2^+ production (in red highlights) is shown in Fig. 5.10 for N_{mean} of 4 in (a), 20 in (b) and 94 in (c). For $N_{mean} \sim 4$, there are two ion pairs contributing to the O_2^+ yield, the O_2^+/C^+ion pair from the breakup of the molecular background resulting an

anticorrelated slope in the PEPIPICO and the weak cluster fragments O_2^+/CO_2^+. The other cluster fragments C^+/CO_2^+, O^+/CO_2^+ and CO^+/CO_2^+ are also shown. The vertical lines in the PEPIPICO are false coincidences.

Figure. 5.10 The ion-ion coincidence map of PEPIPICO measurements of C 1s ionized CO_2 clusters at 320 eV for different mean cluster sizes N_{mean} of 4 in (a), 20 in (b) and 94 in (c). The ion pairs contributing to the O_2^+ production are highlighted in red.

As the cluster size increases $N_{mean} \sim 20$, we observe a significant increase in the production of O_2^+ in this was due to the appearance of new ion pairs of the form $O_2^+/(CO_2)_n^+$. These ion pa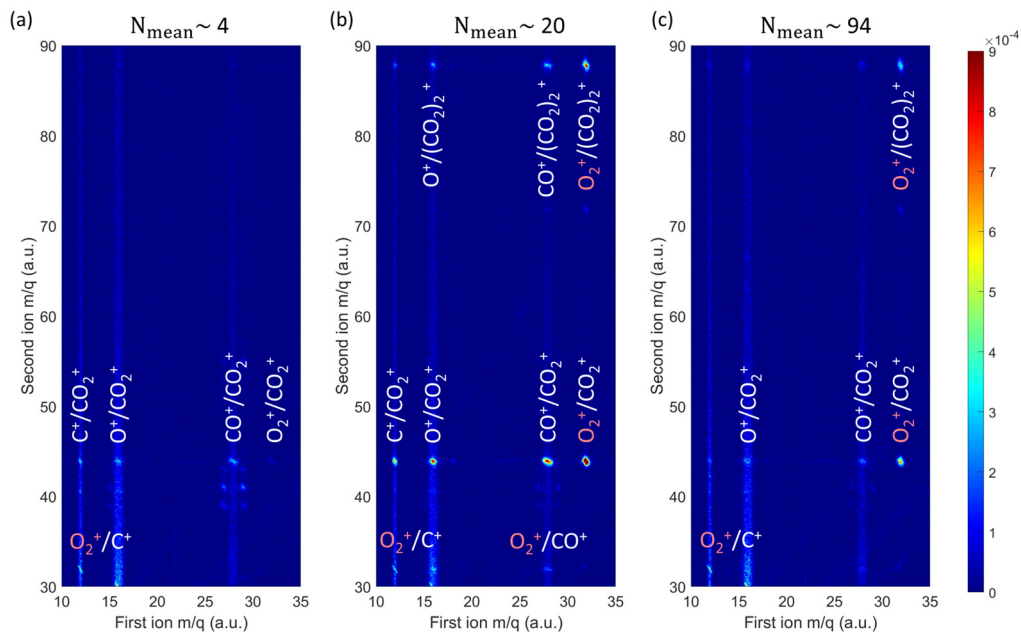ir islands have broad distribution in the PEPIPICO and do not have well defined slope indicating that multiple fragmentation pathways/mechanisms contribute to their formation. The intensity of other cluster ion pairs like $C^+/(CO_2)_n^+$, $O^+/(CO_2)_n^+$ and $CO^+/(CO_2)_n^+$ also increases compared to $N_{mean} \sim 4$. In the total PEPIPICO, the $O_2^+/(CO_2)_n^+$ ion pairs are the second most abundant ion pairs resulting from the dissociation of CO_2 clusters. The dominant ion pairs are of the form $(CO_2)_n^+/(CO_2)_m^+$, where n, m = 1, 2, 3, … corresponding to the dissociation of clusters into smaller singly-charged units of CO_2, they are not shown in Fig. 5.2.2. Hence in the cluster, multiple fragmentation pathways are competing to form either $O_2^+/(CO_2)_n^+$ or $(CO_2)_n^+/(CO_2)_m^+$. There is also a weak ion pair O_2^+/CO^+ at this cluster size. For $N_{mean} \sim 94$, the islands of $O_2^+/(CO_2)_n^+$ are visible but less intense than for $N_{mean} \sim 20$. The intensity of all the cluster fragments $C^+/(CO_2)_n^+$, $O^+/(CO_2)_n^+$ and $CO^+/(CO_2)_n^+$ also decreases at this cluster size. The

decrease in the intensity of the islands on PEPIPICO is likely due to the production of $O_2^+/(CO_2)_n^+$ where n $\gg$ 1 for very larger cluster ions.

The enhancement in the O_2^+ yield is due to reactions accessible to clusters of size $N_{mean} \geq 4$ and results from a multiply charged cluster ion with charge c+ and size N that breaks up into molecular oxygen ion along with singly-charged units of CO_2.

$$(CO_2)_N^{c+} \rightarrow O_2^+ + (CO_2)_n^+ + \cdots \qquad (5.2.1)$$
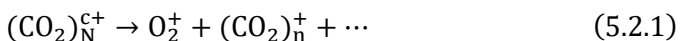
In the fragmentation there are other neutral and/or charged fragments which are not measured in the coincidence event. While we cannot find the mass-to-charge ratios of these *missing fragments*, we can use 3D momentum imaging of ions to find the momentum of these missing fragments. We further analyze the momentum correlation between the ions from the PEPIPICO island of O_2^+/CO_2^+. To visualize the momentum correlation between ions in a coincidence event a Dalitz plot is used. The general description of a Dalitz plot is previously explained in the Data Analysis chapter.
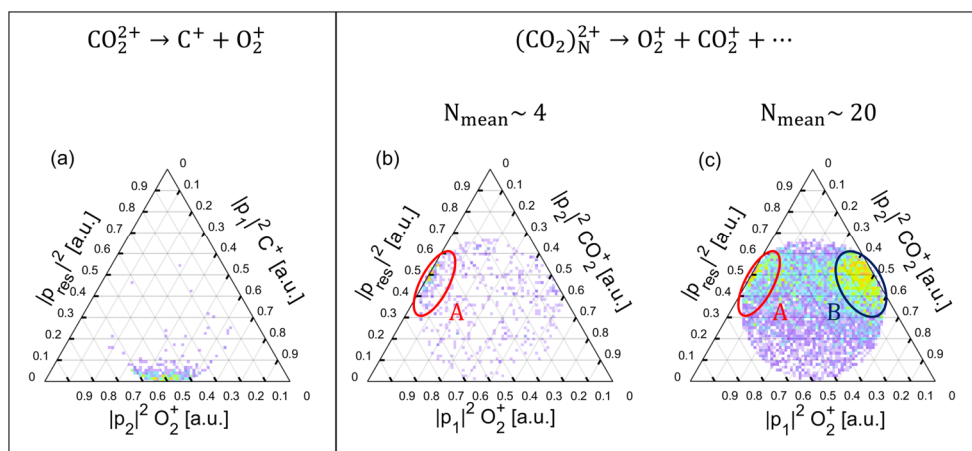
Figure. 5.11 Dalitz plot displaying the momentum correlation between the ions in coincidence events. The panel (a) shows the momentum correlation of O_2^+/C^+ ion pair created by two-body Coloumb explosion of free CO_2 molecules with no missing fragment. The panels (b) and (c) show the momentum correlation of O_2^+/CO_2^+ ion pair created by complex intracluster reactions from CO_2 clusters for $N_{mean} \sim 4$ and $N_{mean} \sim 20$. The two prominent regions A and B in the Dalitz plot are marked in red and blue respectively.

The Dalitz plots are shown in Fig. 5.11 of the ion pairs O_2^+/C^+ in (a) and O_2^+/CO_2^+ are in (b) and (c). The reference O_2^+/C^+ ion pair is created by Coulomb explosion of the CO_2 molecular dication, therefore the norm of momentum of the O_2^+ and C^+ are equal while the direction of the momentum vectors is opposite. This creates a distribution in the lower part of the Dalitz plot with the fraction of the total

momentum being 0.5 for both O_2^+ and C^+. The total kinetic energy released in this fragmentation process is about 7 eV[67]. This is an intramolecular reaction occurring in free CO_2 molecules after core ionization.

$$CO_2{}^{2+} \rightarrow O_2^+ + C^+ + 7eV \qquad (5.2.2)$$

In Fig. 5.11 (b), the Dalitz plot for the O_2^+/CO_2^+ ion pair at $N_{mean} \sim 4$ is shown, there appears to be a distribution on the left-hand side of the plot labelled as region A. In region A, the CO_2^+ ions have less than 0.1 of the total momentum whereas the O_2^+ and the missing fragments have 0.9 of the total momentum. As the momentum of CO_2^+ is uncorrelated to that of O_2^+ and the missing fragments the fragments are produced sequentially by the following reaction,

$$(CO_2)_N^{c+} \rightarrow CO_2^+ + T^{(c-1)+}$$

$$\vdots$$

$$T^{(c-1)+} \rightarrow O_2^+ + X \qquad (5.2.3)$$
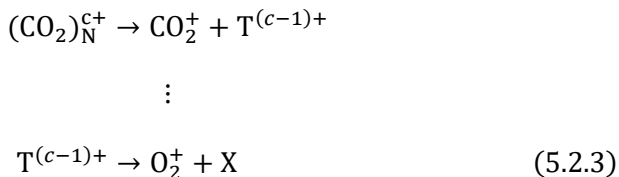
Here, $T^{(c-1)+}$ is the short-lived transient species created in the first step and X is the missing fragment(s) which have the residual momentum. The measured kinetic energy of O_2^+ is less than 5 eV and CO_2^+ is about 0.15 eV for this cluster size.

For the larger cluster size of $N_{mean} \sim 20$, a broad distribution appears to the right-hand side of the Dalitz plot in Fig. 5.11 (c) labelled as region B. The fragmentation mechanisms that create region A also exist at this cluster size, but region B is more intense in the Dalitz plot. In region B, the momentum of the O_2^+ ions less than 0.1 of the total momentum whereas the CO_2^+ and the missing fragments have 0.9 of the total momentum. Here the momentum of O_2^+ is uncorrelated to that of CO_2^+ and the missing fragments the fragments are produced sequentially by the reaction similar to region A,

$$(CO_2)_N^{c+} \rightarrow O_2^+ + T^{(c-1)+}$$

$$\vdots$$

$$T^{(c-1)+} \rightarrow CO_2^+ + X \qquad (5.2.4)$$
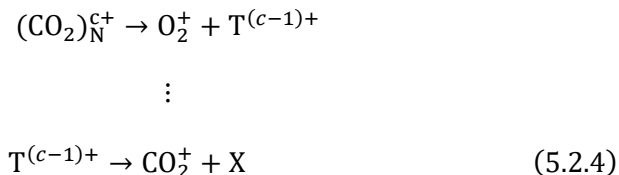
The measured kinetic energy of O_2^+ is about 0.37 eV and CO_2^+ is less than 5 eV for this cluster size. Therefore, the sequentially fragmentation mechanisms that lead to region A and B have very different kinematics. These mechanisms are fundamentally different from the O_2^+/C^+ because they involve intermolecular interaction within the cluster. For larger cluster size of up to $N_{mean} \sim 94$ we found similar Dalitz plots to Fig. 5.11 (c). The mechanism corresponding to region A exists

at all cluster sizes (4 to 94) while the mechanism leading to region B requires a critical cluster size which lies between the cluster sizes of 4 to 20.
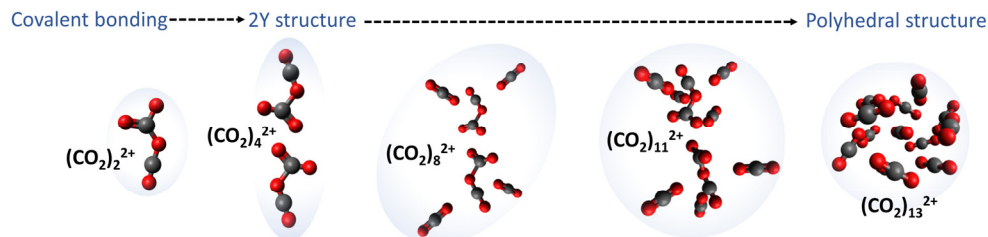

Figure. 5.12 The change in geometry of the doubly-charged CO_2 cluster from covalent bonding to a 2Y-structure for small clusters to a polyhedral structure for cluster sizes above 11.

The geometry of the cluster dication $(CO_2)_N^{2+}$ were optimized using density functional theory (DFT) calculations[6] to obtain the structures shown in Fig. 5.12 for cluster size 2 to 13. The neutral CO_2 clusters are bound by Van der Waals interaction between the molecules in the cluster but the optimized geometries of the small cluster dications have covalent bond formation between the CO_2 molecules. The $(CO_2)_2^{2+}$ dimer dication has a 'Y-like' structure, this structure evolves with the increasing cluster size. For the $(CO_2)_4^{2+}$, a geometry with double Y or '2Y structure' is formed and it consists of the two sets of covalently bonded molecules which interact with each other. As the cluster grows from 4 to 12, the 2Y structure is preserved with additional molecules interacting with it via non-covalent bonding which eventually forms a polyhedral geometry with no covalent bonding. The $(CO_2)_{13}^{2+}$ closely resembles the neutral cluster geometry. For N > 12, the 2Y structure are not observed in the optimized geometries. Interestingly, the enhancement in the O_2^+ yield is also observed in this cluster size range from 4 to 20 and therefore might be due to the change in the cluster dication geometry from 2Y structure to polyhedral structure.

To further understand how the cluster dication fragments into O_2^+/CO_2^+ ion pair, ab initio molecular dynamics (AIMD) simulations within the first few hundred femtoseconds of ionized $(CO_2)_5^{2+}$ were performed. According to the simulations, two distinct pathways of fragmentation were identified (see Paper I). In the first pathway, the $(CO_2)_5^{2+}$ complex structure undergoes rearrangement, leading to the formation of O_2^+/CO_2^+ within 70 femtoseconds after dication formation. The second pathway involves dissociation of the ionized CO_2 molecule, followed by intracluster reactions resulting in O_2^+/CO_2^+ within 80 femtoseconds.

---

[6] Theoretical study done by Sergio Diaz-Tendero and Dario Barreiro-Lage

To understand the energetic characteristics of these mechanisms, we also investigated the potential-energy surfaces (PES) responsible for generating these fragments (see Paper I). The core-ionized molecule in the cluster can undergo a localized or delocalized Auger decay leading to different PES. For the delocalized case, the Auger decay can occur in a neighbouring molecule in the cluster via Intermolecular Coulombic Decay[61,103,210] (ICD) instead of the same molecule leading to delocalized dicationic states of the $(CO_2)_N^{2+}$ cluster with structures shown in Fig. 5.12. The PES calculations of $(CO_2)_4^{2+}$ showed the 2Y structure undergoes further rearrangement if it has sufficient internal energy. It can undergo two endothermic reactions reaching the dissociation channels O_2^+/CO_2^+ and O_2^+/CO^+ with potential energy barriers of 4.11 eV and 5.42 eV respectively.

For the localized Auger decay, a molecular dication CO_2^{2+} is created in the cluster surrounded by neutral CO_2 molecules. Due to Coulomb explosion of the doubly charged molecule, O^+ and CO^+ are created with kinetic energy release of about 6 eV[211]. The surrounding neutral molecules can act as a cage for 'trapping' these high energy ions and increasing the probability of recombination reactions of O^+ and CO^+ with the neutral molecules. The PES calculation of the $CO_2^{2+}(CO_2)_7$ complex showed that the recombination reaction of O^+ with neutral CO_2 molecules forms $OCOO^+$ ion[212,213] that dissociates into O_2^+ exothermically. And the interaction of CO^+ with neutral CO_2 molecules results in exothermic charge transfer reaction forming CO_2^+. These recombination reactions calculated using PES exploration were analogous to the ion-neutral collision reactions[214–218] of O^+ and CO^+ with neutral CO_2 molecules reported previously.

Therefore, the PES calculations suggest three pathways of O_2^+ production from CO_2 clusters. Delocalized Auger decay leads to the $(CO_2)_N^{2+}$ cluster which dissociates endothermically to form O_2^+/CO_2^+ or O_2^+/CO^+. Alternatively, localized Auger decay leads to $CO_2^{2+}(CO_2)_N$ cluster which undergoes intracluster collision-like ion neutral reactions to form O_2^+/CO_2^+ exothermically.

5.2.3   Branching ratios

The experimental relative yield (or branching ratio) of the O_2^+/CO_2^+ (in blue), O_2^+/CO^+ (in green) and the total O_2^+ yield (in red) is shown in Fig. 5.13 as a function of the mean cluster size, the yield is normalized with respect to the O_2^+/C^+ counts coming from the practically constant molecular background. When small clusters containing about 4 to 10 molecules are formed, there is a significant increase in the yield of O_2^+/CO^+, which is formed through an endothermic reaction with a high activation barrier. This yield reaches a maximum around 10 to 20 molecules, and then gradually decreases to a constant level for larger clusters. This behavior can be attributed to the fact that for the small cluster sizes the internal energy is enough to pass the activation barrier. However, as the cluster size increases, this internal

energy is redistributed among a growing number of degrees of freedom, resulting in decreased heat. Hence, above a certain critical size, this internal energy is no longer sufficient to overcome the activation barrier for the formation of O_2^+/CO^+, leading to a significant decrease in its signal.
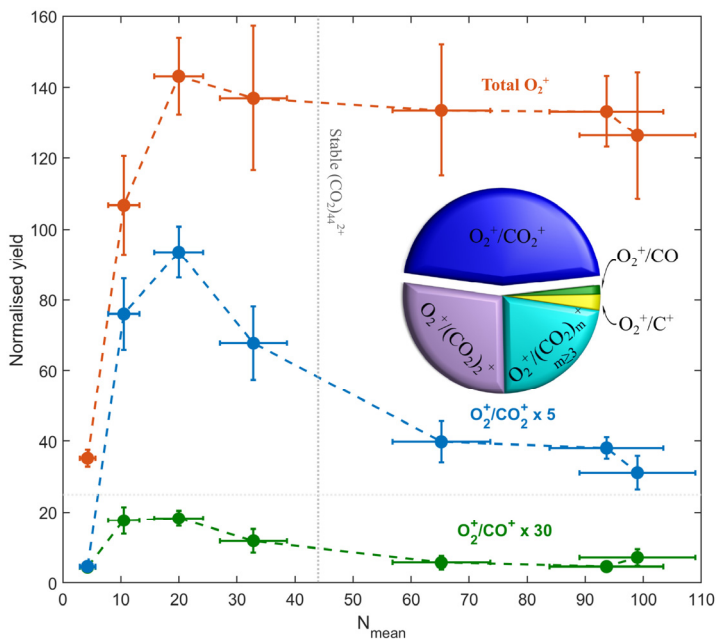
Figure. 5.13 The experimental yields of O_2^+ measured as a function of the mean cluster size (N_{mean}), with events in coincidence with CO^+ ion (green) or CO_2^+ ion (blue), and for all O_2^+ events (red), including single ion events. The yields were normalized to the O_2^+ yield from the molecule given by the coincidence signal O_2^+/C^+. The formation of a stable doubly charged cluster above the critical size of N_{mean} = 44 is indicated by the dotted line.

The yield of O_2^+/CO_2^+ exhibits a peaked structure and is made up of contributions from different types of reactions. Similar to the O_2^+/CO^+ channel, there is an endothermic reaction involved. However, even for larger clusters there is a significant yield of O_2^+/CO_2^+, which is the signature of an exothermic reaction due to intra-cluster collisions also suggested by PES calculations. This behaviour reflects the complex interplay between the internal energy of the system, the number of degrees of freedom, and the activation barriers associated with different chemical reactions.

The pie chart in Fig. 5.13 shows the contributions of different ion pairs to the total O_2^+ signal for $N_{mean} \sim 20$, the dominant contributions are from O_2^+/CO_2^+ and $O_2^+/(CO_2)_2^+$. For larger mean cluster sizes there are multitude of competing fragmentation channels forming $O_2^+/(CO_2)_m^+$ ($m \geq 3$) which become dominant.

However, the yield of these ion pairs involving larger fragments in coincidence with O_2^+ is limited by the experimental detection efficiency and can result in aborted coincidence events[219] with only the O_2^+ measured. Therefore, the total O_2^+ yield is useful to account for all possible fragmentation channels including the aborted coincidence events. The total O_2^+ yield behaves like a step function reaching its maxima between $N_{mean} \sim 10$ to 20 molecules. The step function indicates that the exothermic reaction is activated only when the cluster has minimum of ~10 molecules. After the activation, the efficiency of O_2^+ production is roughly constant for large CO_2 clusters, even beyond the critical size for the formation of stable CO_2 clusters dications.

5.2.4 Classical simulations of intra-cluster collision reactions

The quantum chemical PES and AIMD calculations do not calculate the momentum distribution of the ions and therefore cannot be directly correlated with the signature of two processes in the Dalitz plot. To understand the momentum correlations between the O_2^+/CO_2^+ ions, a simple classical intracluster collision model was used to simulate the exothermic reaction, originating from the breakup of the doubly charged molecule into O^+ and CO^+. These ions collide and react with the surrounding neutral CO_2 molecules to form the O_2^+/CO_2^+ ion pair.
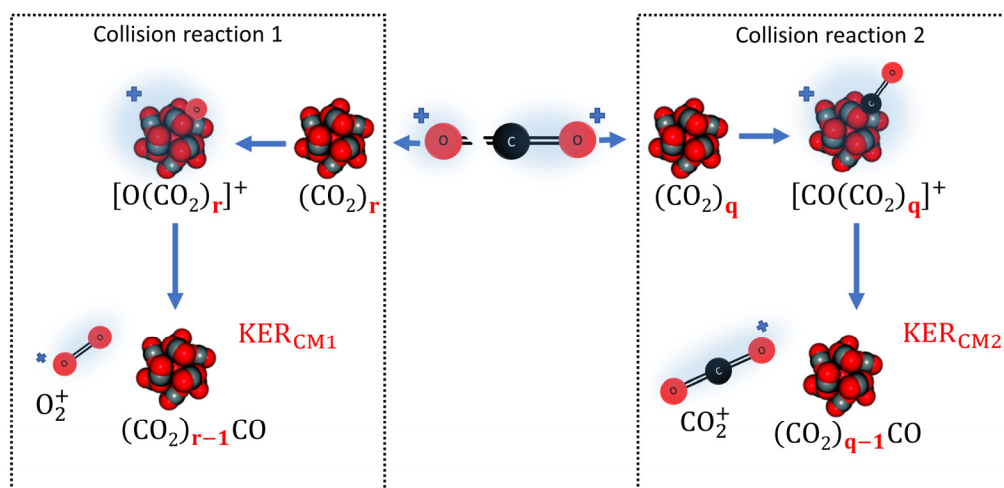
Figure. 5.14 Schematic showing the chemical reactions simulated using classical intracluster collision model. There are two collision reactions occuring independently in the cluster involving collision of O^+ and CO^+ with the surrounding neutral molecules. In the first collision reaction, The O^+ collides with $(CO_2)_r$, and forms a complex $[O(CO_2)_r]^+$ which fragments into O_2^+ and $(CO_2)_{r-1}CO$, with a total kinetic energy release of KER_{CM1}. In the second collision reaction, CO^+ collides $(CO_2)_q$, and forms a complex $[CO(CO_2)_q]^+$ which fragments into CO_2^+ and $(CO_2)_{q-1}CO$, with a total kinetic energy release of KER_{CM2}.

The summary of the simulated reactions is shown in Fig. 5.14. We consider two ion-neutral cluster reactions occurring inside the cluster. The O^+ collides with a part of the cluster $(CO_2)_r$, and forms a complex $[O(CO_2)_r]^+$ which eventually fragments into O_2^+ and $(CO_2)_{r-1}CO$. Similarly, the CO^+ collides with a part of the cluster $(CO_2)_q$, and forms a complex $[CO(CO_2)_q]^+$ which eventually fragments into CO_2^+ and $(CO_2)_{q-1}CO$. It is assumed that these two collision reactions are independent of each other and that the mother cluster $CO_2{}^{2+}(CO_2)_N$ is at rest for simplicity. When the dication breaks up, the momentum of the two ions O^+ and CO^+ are correlated by the relation,

$$\overrightarrow{p_{O^+}} = -\overrightarrow{p_{CO^+}} \tag{5.2.5}$$

After the $[O(CO_2)_r]^+$ complex is formed the total momentum of this complex is equal to $\overrightarrow{p_{O^+}}$, given that the $(CO_2)_r$ cluster was at rest and if no energy lost or gained after the complex is formed. Similarly, the momentum of $[CO(CO_2)_q]^+$ is equal to $\overrightarrow{p_{CO^+}}$.
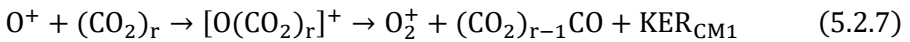
$$\overrightarrow{p_{[O(CO_2)_r]^+}} = \overrightarrow{p_{O^+}}$$
$$\overrightarrow{p_{[CO(CO_2)_q]^+}} = \overrightarrow{p_{CO^+}}$$
$$\overrightarrow{p_{[O(CO_2)_r]^+}} = -\overrightarrow{p_{[CO(CO_2)_q]^+}} \tag{5.2.6}$$

To calculate the momentum of the fragments O_2^+ and $(CO_2)_{r-1}CO$ from the first complex, consider the center of mass (CM) frame of the $[O(CO_2)_r]^+$ complex. In the following, all the quantities in the CM frame will have a prime ($'$) notation. The chemical reaction evolves as follows,

$$O^+ + (CO_2)_r \rightarrow [O(CO_2)_r]^+ \rightarrow O_2^+ + (CO_2)_{r-1}CO + KER_{CM1} \tag{5.2.7}$$

Here, KER_{CM1} is the total kinetic released in the center of mass frame of the $[O(CO_2)_r]^+$ complex. In this frame of reference, the magnitude of momentum of the fragment O_2^+ is given by,

$$\left|\overrightarrow{p'_{O_2^+}}\right| = \sqrt{2 . KER_{CM1} . m_{O_2^+} . x'(r)} \tag{5.2.8}$$

where the scaling factor,

$$x'(r) = \frac{m_{(CO_2)_{r-1}CO}}{m_{O_2^+} + m_{(CO_2)_{r-1}CO}} \tag{5.2.9}$$

Therefore, when $m_{(CO_2)_{r-1}CO} \gg m_{O_2^+}$, the scaling factor $x'(r) \to 1$ and the magnitude of momentum of O_2^+, $\left|\overrightarrow{p'}_{O_2^+}\right| \to \sqrt{2.\,KER_{CM1}.\,m_{O_2^+}}$ for very large values of r. Likewise, for the second collision complex $\left[CO(CO_2)_q\right]^+$ the chemical reaction evolves as follows,

$$CO^+ + (CO_2)_q \to \left[CO(CO_2)_q\right]^+ \to CO_2^+ + (CO_2)_{q-1}CO + KER_{CM2} \quad (5.2.10)$$
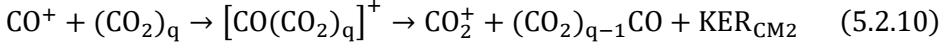
And we can calculate the magnitude of momentum of the fragment CO_2^+ is given by,

$$\left|\overrightarrow{p'}_{CO_2^+}\right| = \sqrt{2.\,KER_{CM2}.\,m_{CO_2^+}.\,y(q)} \quad (5.2.11)$$

Where the scaling factor,

$$y'(q) = \frac{m_{(CO_2)_{q-1}CO}}{m_{CO_2^+} + m_{(CO_2)_{q-1}CO}} \quad (5.2.12)$$

And for large q, $m_{(CO_2)_{q-1}CO} \gg m_{CO_2^+}$, the scaling factor $y'(q) \to 1$ and $\left|\overrightarrow{p'}_{CO_2^+}\right| \to \sqrt{2.\,KER_{CM2}.\,m_{CO_2^+}}$.

The dependence of $\left|\overrightarrow{p'}_{O_2^+}\right|$ and $\left|\overrightarrow{p'}_{CO_2^+}\right|$ on r and q respectively is shown in Fig. 5.15 for different values of KER_{CM}. It appears to be sensitive for small r and q values and then tends to constant for $r, q > 10$. Thus, according to this simple model, for large clusters with $N > 20$ the magnitude of the momentum of O_2^+ and CO_2^+ will be independent of the cluster size N if each ion collides and interacts with half of the cluster ($r = q = N/2$).

Now in the centre of mass frames of reference, the fragments O_2^+ and CO_2^+ can be emitted in any direction[220]. The resulting momentum vectors of O_2^+ and CO_2^+ will be isotropic therefore we must consider the spheres in 3D momentum space with radius defined by equations (5.2.8) and (5.2.11). We can write these vectors in 3D spherical coordinates as,

$$\overrightarrow{p'}_{O_2^+} = \sqrt{2.\,KER_{CM1}.\,m_{O_2^+}.\,x(r)}\,\hat{\rho} + \theta\,\hat{\theta} + \phi\,\hat{\phi} \quad (5.2.13)$$

$$\overrightarrow{p'}_{CO_2^+} = \sqrt{2.\,KER_{CM2}.\,m_{CO_2^+}.\,y(q)}\,\hat{\rho} + \theta\,\hat{\theta} + \phi\,\hat{\phi} \quad (5.2.14)$$

Here, ρ is the radius, θ is the elevation angle and ϕ is the azimuthal angle. The vectors are calculated by scanning θ between $\left[-\dfrac{\pi}{2}, \dfrac{\pi}{2}\right]$ and ϕ between $[-\pi, \pi]$.
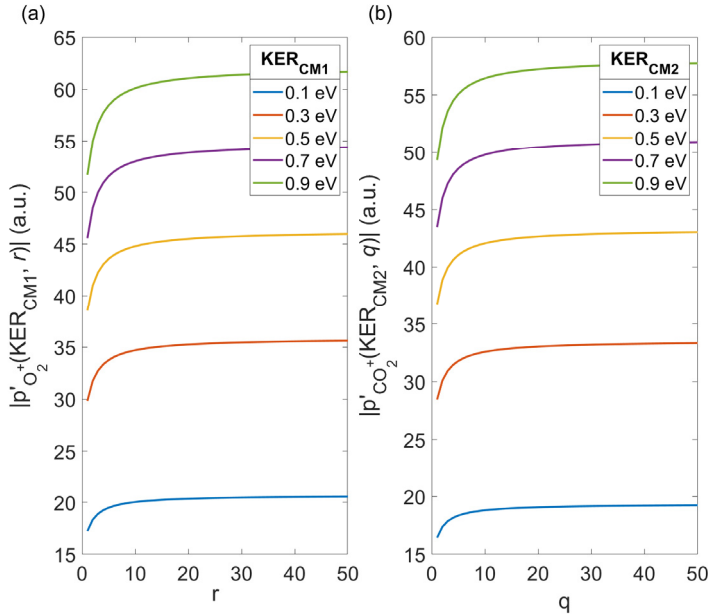
Figure. 5.15 The cluster size dependence of the momentum of O_2^+ in (a) and CO_2^+ in (b), it is calculated in the CM frame for different values of kinetic energy release ($\mathrm{KER_{CM1}}, \mathrm{KER_{CM2}}$). The momentum in the CM frame is sensitive to the cluster size for $r, q < 10$ and for larger clusters it reaches an asymptotic limit for all values of $\mathrm{KER_{CM}}$.

To compare to the experimental data, we must convert the vectors from the cluster CM frame to the laboratory frame by adding the velocity of the CM frame. The momentum vectors in the lab frame are given by,

$$\overrightarrow{p_{O_2^+}} = \overrightarrow{p'_{O_2^+}} + m_{O_2^+} \cdot \overrightarrow{v_{[O(CO_2)_r]^+}} \qquad (5.2.15)$$

The velocity of the $[O(CO_2)_r]^+$ complex is calculated using equation (5.2.6),

$$\overrightarrow{v_{[O(CO_2)_r]^+}} = \frac{\overrightarrow{p_{O^+}}}{m_{[O(CO_2)_r]^+}} \qquad (5.2.16)$$

Therefore, combining equation (5.2.15) and (5.2.16),

$$\overrightarrow{p_{O_2^+}} = \overrightarrow{p'_{O_2^+}} + \overrightarrow{p_{O^+}} \cdot x(r) \qquad (5.2.17)$$

Here the scaling factor is,

$$x(r) = \frac{m_{O_2^+}}{m_{[O(CO_2)_r]^+}} \tag{5.2.18}$$

For large r, the scaling factor $x(r) \to 0$ and $\left|\overrightarrow{p_{O_2^+}}\right| \sim \left|\overrightarrow{p'_{O_2^+}}\right| \to \sqrt{2.\,KER_{CM1}.\,m_{O_2^+}}$ and the momentum vectors of O_2^+ become independent of r.

Similarly, for the CO_2^+ fragment the momentum vector in laboratory frame is calculated using,

$$\overrightarrow{p_{CO_2^+}} = \overrightarrow{p'_{CO_2^+}} + \overrightarrow{p_{CO^+}}.\,y(q) \tag{5.2.19}$$

Using the equation (5.2.5) we can rewrite as a function of $\overrightarrow{p_{O^+}}$,

$$\overrightarrow{p_{CO_2^+}} = \overrightarrow{p'_{CO_2^+}} - \overrightarrow{p_{O^+}}.\,y(q) \tag{5.2.20}$$

Here the scaling factor is,

$$y(q) = \frac{m_{CO_2^+}}{m_{[CO(CO_2)_q]^+}} \tag{5.2.21}$$

And for large q, the momentum vectors $\left|\overrightarrow{p_{CO_2^+}}\right| \to \sqrt{2.\,KER_{CM2}.\,m_{CO_2^+}}$ in the laboratory frame. The final momentum vectors of O_2^+ and CO_2^+ remain correlated in the laboratory frame even though the collision reactions are occurring independently. In the laboratory frame, for a given value of $\overrightarrow{p_{O^+}}$, any of the possible vectors $\overrightarrow{p_{O_2^+}}$ and $\overrightarrow{p_{CO_2^+}}$ can be detected in coincidence in the experiment. Hence, to preserve the nature of coincidence detection, all possible combinations of the two collision reactions are considered for simulating the experimental coincidence data.

For the simulations, the vectors $\overrightarrow{p_{O^+}}$ are taken from the experimental data for molecular CO_2 and fixed in the positive X direction. We have four free parameters are that are tuned to match with the experimental data are,
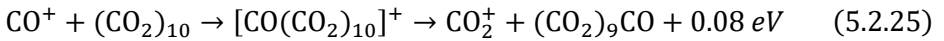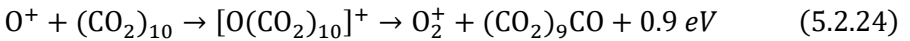
1. The size of the cluster complexes (r, q) formed after collision, for simplifying the problem we set the total cluster size $N = r + q$. Therefore, we have two free parameters related to cluster size: N, r.
2. The kinetic energy released in the center of mass frames due to the fragmentation of the cluster complexes: KER_{CM1}, KER_{CM2}.

For testing this classical collision model, we compared the simulated data to the experimental data measured at $N_{mean} \sim 20$ for the two prominent regions A and B discussed in Fig. 5.11. For the simulations, the free parameters related to cluster size are set as $N = 20$ and $r = q = 10$. The starting point of the simulation for KER_{CM1} and KER_{CM2} was estimated by taking the statistical mode[7] in the experimental distributions of $\left|\overrightarrow{p_{O_2^+}}\right|$ and $\left|\overrightarrow{p_{CO_2^+}}\right|$ and using the approximation for large r and q.

$$KER_{CM1}^{Start} = \frac{\left|\overrightarrow{p_{O_2^+}(mode)}\right|^2}{2m_{O_2^+}} \tag{5.2.22}$$

$$KER_{CM2}^{Start} = \frac{\left|\overrightarrow{p_{CO_2^+}(mode)}\right|^2}{2m_{CO_2^+}} \tag{5.2.23}$$

Then the KER_{CM1} and KER_{CM2} are fine tuned to match the experimental $\left|\overrightarrow{p_{O_2^+}}\right|$ and $\left|\overrightarrow{p_{CO_2^+}}\right|$ distributions respectively. Finally, for the best-found values of KER_{CM1} and KER_{CM2} the dalitz plots are made. In Fig. 5.16 and Fig. 5.17 the simulated Dalitz plot for Region A and B are shown along with experimental data. For region A, the best fit of the kinetic energy released was found for $KER_{CM1} = 0.9\ eV$ and $KER_{CM2} = 0.08\ eV$. Whereas for region B, the best fit of the kinetic energy released was found for $KER_{CM1} = 0.13\ eV$ and $KER_{CM2} = 1\ eV$. The simulated chemical reactions for region A are,

$$O^+ + (CO_2)_{10} \rightarrow [O(CO_2)_{10}]^+ \rightarrow O_2^+ + (CO_2)_9 CO + 0.9\ eV \tag{5.2.24}$$

$$CO^+ + (CO_2)_{10} \rightarrow [CO(CO_2)_{10}]^+ \rightarrow CO_2^+ + (CO_2)_9 CO + 0.08\ eV \tag{5.2.25}$$

For region B the simulated chemical reactions are,

$$O^+ + (CO_2)_{10} \rightarrow [O(CO_2)_{10}]^+ \rightarrow O_2^+ + (CO_2)_9 CO + 0.13\ eV \tag{5.2.26}$$

$$CO^+ + (CO_2)_{10} \rightarrow [CO(CO_2)_{10}]^+ \rightarrow CO_2^+ + (CO_2)_9 CO + 1\ eV \tag{5.2.27}$$
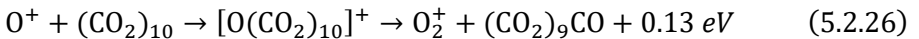
The best-found values for KER_{CM1} and KER_{CM2} would be applicable for larger values of $r, q > 10$ (see Fig. 5.15), for smaller r and q however the region A and B cannot be simulated using the same KER_{CM1} and KER_{CM2}. Here an example of symmetric cluster fission when $r = q$ is shown. It should be noted that the

---

[7] In a histogram, the statistical mode represents the bin with the highest frequency, where a bin is range of values that are grouped together.

calculated values of KER_{CM1} and KER_{CM2} depend on the values of (r, q) and would be different in the case of asymmetric breakup i.e., $r \neq q$.

Region A
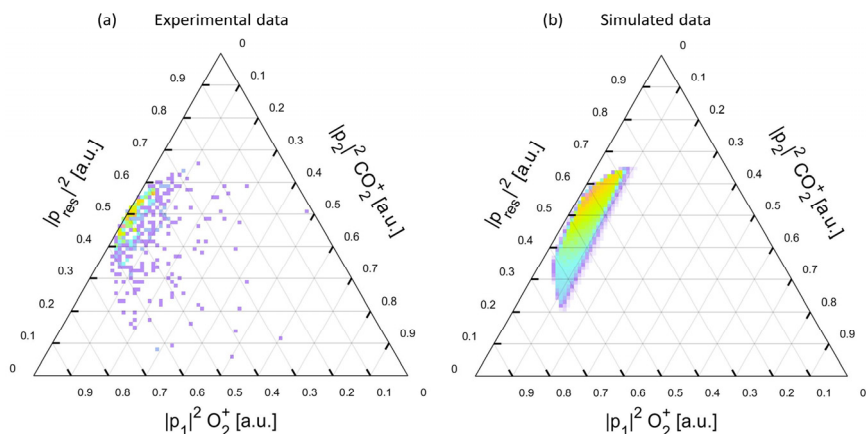
Figure. 5.16 The experimental and simulated Region A of the momentum correlation of the O_2^+/CO_2^+ ion pair produced from CO_2 clusters with cluster size $N_{mean} \sim 20$. (a) shows the filtered experimental momentum correlation of the O_2^+/CO_2^+ ion pair to extract only the Region A of the Dalitz plot. (b) shows the simulated data using the intracluster coliision model described in the text using the chemical reactions in (5.2.24) and (5.2.25).

Region B
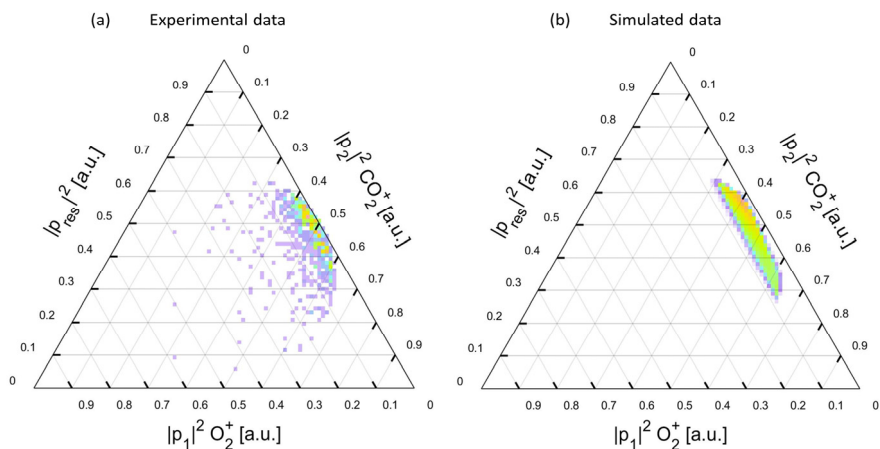
Figure. 5.17 The experimental and simulated Region B of the momentum correlation of the O_2^+/CO_2^+ ion pair produced from CO_2 clusters with cluster size $N_{mean} \sim 20$. (a) shows the filtered experimental momentum correlation of the O_2^+/CO_2^+ ion pair to extract only the Region B of the Dalitz plot. (b) shows the simulated data using the intracluster coliision model described in the text using the chemical reactions in (5.2.26) and (5.2.27).

According to the model, the momentum distributions will be sensitive to cluster sizes N < 20, for the larger clusters the momentum distribution will be independent of N and depend on KER_{CM}. Also, we could calculate the difference in kinetic energy release of collision chemical reactions to simulate the region A and B in the Dalitz plot. Therefore, using the classical intracluster collision model we can simplify the problem of cluster fragmentation. We studied the effect of different cluster sizes and kinetic energy release on the momentum distributions observed on the Dalitz plot.

6   Conclusion and Outlook

This thesis investigates the ultrafast dynamics of core excited/ionized adamantane and carbon dioxide clusters using synchrotron radiation. Our results provide new insight into the fragmentation dynamics of these small quantum systems, employing 3D momentum imaging and electron-ion coincidence spectroscopy. We provide evidence that the interplay between electronic and nuclear dynamics can depend on structural changes and preserve site selectivity, exemplifying the richness of the field of X-ray-induced photochemistry. Additionally, the thesis advances coincidence spectroscopy by demonstrating false coincidence removal in Auger electron-Photoion-Photoion coincidence (AEPIPICO) data and reports details of the newly commissioned ICE REMI spectrometer, which will facilitate future research in this area.

On Cluster Photochemistry

In **Paper I**, we investigated the photoreactions of core-ionized CO_2 clusters. Combining our experimental results with quantum chemistry calculations, we determined that the enhanced production of O_2^+ was due to a structural transition of the clusters from a covalently bonded arrangement to a weakly bonded polyhedral geometry that activates an exothermic reaction producing O_2^+. The kinematics of the exothermic intracluster collision reaction is simulated using a simple classical model, and the influence of cluster size on the kinematics is reported.

It is crucial to conduct an in-depth analysis of the impact of cluster size and geometry on the photoreactions for their quantitative application in atmospheric chemistry, considering the wide range of clusters or particle sizes involved. However, the currently available cluster beam sources produce broad size distributions, especially for large cluster sizes, which limited the accuracy of the results due to uncertainty about the exact cluster size. To overcome this limitation, future experiments could use size-selected clusters to reduce uncertainty in cluster size. Additionally, this work can be extended to include cluster systems doped with solvents or heavy metals to study the influence of the environment on cluster fragmentation reactions.

In the case of CO_2-rich planetary atmospheres, such as that of Mars, significant photochemical processes occur due to exposure to ionizing radiation. CO_2 clusters are predicted to exist at high altitudes in the Martian atmosphere[26], and thus, it is essential to understand their photochemistry. However, large photochemistry

models of the Martian atmosphere have underestimated the O_2^+ abundance compared to experimental measurements, possibly due to neglecting the photoreactions of CO_2 clusters. Our study reveals that CO_2 clusters generate O_2^+ at least 100 times more efficiently than CO_2 molecules when exposed to ionizing radiation. Hence, the photochemistry of small clusters or particles can significantly impact the ion balance in planetary atmospheres and needs to be considered in models. However, further benchmark measurements comparing ion yields of clusters with free molecules are necessary for accurately implementing cluster chemistry in large astrochemistry models. Further, to examine the impact of cluster photochemistry on the lower altitudes of the Martian atmosphere, it would be useful to expand these benchmark studies to include CO_2-water mixed clusters.

On Molecular Photochemistry

In **Paper II**, the electronic relaxation and fragmentation of C 1s ionized adamantane depends on the carbon atom ionization site. The theoretical calculations were used to determine the final two-hole (2h) state reached after normal Auger decay of the core hole for the CH or CH_2 site. In the experimental Auger electron-ion-ion coincidence data, by selecting the theoretical 2h states for the CH and CH_2 site, we observed that the fragmentation of the adamantane dication is site-dependent. More specifically, we found that the CH_2 site ionization promotes neutral hydrogen loss.

In **Paper III**, after resonant excitation of the C 1s electron of adamantane, when the molecule undergoes participator Auger decay and reaches a one-hole (1h) final state, the core-hole memory is preserved. The fragmentation of the cation depends on the core-hole site and the excess internal energy of the final state. The C 1s$\rightarrow$ CH valence orbital excitation favors the production of $C_6H_7^+$ after participator decay. If the molecule undergoes spectator Auger decay, then the final two-hole state with spectator electron (2h-1p) also depends on the core-hole site, however, no significant difference in dication fragmentation was observed between the two sites. The study also found a difference in the yield of the methyl ion CH_3^+ compared to previous results, suggesting a difference in cage opening of the adamantane dication following C 1s excitation and ionization. Additionally, neutral hydrogen loss from adamantane cation and dications is studied and the excess internal energy required for hydrogen loss is estimated.

We infer from **Paper II** and **Paper III** that the nature of site sensitivity for C 1s electron excitation and ionization is very different. It results in unique fragmentation of the carbon cage of adamantane with many competing relaxation pathways like hydrogen loss, hydrogen migration, cage opening, and C-C bond breaking. One possible approach to directly measure the ultrafast dynamics and compare the cage opening of core excited and ionized adamantane is to employ time-resolved coincidence spectroscopy[221–224] with free electron lasers, which allows the study of the electronic and nuclear relaxation of the core hole state. During the thesis work, studies were conducted to explore the cage-opening mechanism of adamantane

upon direct valence ionization. Further development of these studies is critical to improving our understanding of core excited/ionized systems.

The adamantane study addresses the question of why diamondoids are not found in the interstellar medium. We found that ionizing radiation breaks down adamantane and possibly larger diamondoids into smaller hydrocarbons, indicating a lack of photostability. In contrast, polyaromatic hydrocarbons (PAHs) are abundant in the interstellar medium[225,226]. They maintain their carbon backbone despite undergoing H_2 or C_2H_2 loss and are thus more photostable than adamantane. We show that irradiated adamantane also undergoes H/H_2 loss, but it leads to carbon backbone fragmentation. Therefore, to fully answer the research question, this study needs to be extended to larger diamondoids. Finally, an interesting aspect of the adamantane study touches upon the very debated topic of site-selective fragmentation. While it is common in heteronuclear molecules, site-selectivity in highly symmetric homonuclear molecules like adamantane is surprising. By understanding the site-selective fragmentation of molecules, it may be feasible to engineer photochemical reactions with precise outcomes by manipulating factors like the shape of the molecule. This could lead to significant advancements in fields like radiation therapy.

On experimental development

In **Paper IV**, the development and commissioning results of the ICE end station at MAXIV Laboratory are discussed. The ICE REMI spectrometer is capable of detecting photoelectron-ion coincidences using various sample delivery systems to study molecules and clusters and combines X-ray Photoelectron Spectroscopy (XPS) with ion mass spectrometry and 3D momentum imaging. It can be operated in different modes to optimize electron or ion momentum resolution based on experimental requirements. Overall, this end station is expected to advance X-ray-induced photochemistry research in Lund.

Coincidence spectroscopy is a valuable tool for studying core excited/ionized systems because it allows for the measurement of the correlated electrons and ions that result from the evolution of the core hole state. To achieve a complete understanding of these systems, it is crucial to measure all the particles generated during the relaxation of the core hole state. Complete coincidence measurements, such as the Photoelectron-Auger electron-photoion-photoion coincidence, require further development of spectrometers and detectors.

References

1. Einstein, A. Über einen die Erzeugung und Verwandlung des Lichtes betreffenden heuristischen Gesichtspunkt. (1905).

2. Siegbahn, K. *ESCA: atomic, molecular and solid state structure studies by means of electron spectroscopy. Nova Acta Regiae Societatis Scientiarum Upsaliensis* (Almqvist & Wiksell, 1967).

3. Gelius, U. & Siegbahn, K. ESCA studies of molecular core and valence levels in the gas phase. *Faraday Discuss. Chem. Soc.* **54**, 257–268 (1972).

4. Ossiander, M. *et al.* Absolute timing of the photoelectric effect. *Nature* **561**, 374–377 (2018).

5. Baer, T. & Dunbar, R. C. Ion Spectroscopy: Where Did It Come From; Where Is It Now; and Where Is It Going? *J. Am. Soc. Mass Spectrom.* **21**, 681–693 (2010).

6. Zettergren, H. *et al.* Roadmap on dynamics of molecules and clusters in the gas phase. *Eur. Phys. J. D* **75**, 152 (2021).

7. Bozek, J. D. & Miron, C. Ultrafast molecular dynamics illuminated with synchrotron radiation. *J. Electron Spectros. Relat. Phenomena* **204**, 269–276 (2015).

8. Carroll, T. X. *et al.* Carbon 1s core-hole lifetime in CO2. *Phys. Rev. A - At. Mol. Opt. Phys.* **61**, 7 (2000).

9. Tielens, A. G. G. M. The molecular universe. *Rev. Mod. Phys.* **85**, 1021–1081 (2013).

10. Peeters, E., Mackie, C., Candian, A. & Tielens, A. G. G. M. A Spectroscopic View on Cosmic PAH Emission. *Acc. Chem. Res.* **54**, 1921–1933 (2021).

11. Tielens, A. G. G. M. Interstellar polycyclic aromatic hydrocarbon molecules. *Annu. Rev. Astron. Astrophys.* **46**, 289–337 (2008).

12. Peeters, E. The PAH hypothesis after 25 years. *Proc. Int. Astron. Union* **7**, 149–161 (2011).

13. Henning, T. & Salama, F. Carbon in the Universe. *Science.* **282**, 2204–2210 (1998).

14. Oomens, J. *et al.* Infrared spectroscopic investigation of higher diamondoids. *J. Mol. Spectrosc.* **238**, 158–167 (2006).

15. Acke, B. & van den Ancker, M. E. A survey for nanodiamond features in the 3 micron spectra of Herbig Ae/Be stars. *A&A* **457**, 171–181 (2006).

16. Zhang, R., Khalizov, A., Wang, L., Hu, M. & Xu, W. Nucleation and growth of nanoparticles in the atmosphere. *Chem. Rev.* **112**, 1957–2011 (2012).

17. Kulmala, M. *et al.* Direct Observations of Atmospheric Aerosol Nucleation. *Science.* **339**, 943–946 (2013).

18. Kulmala, M. *et al.* Formation and growth rates of ultrafine atmospheric particles: A review of observations. *J. Aerosol Sci.* **35**, 143–176 (2004).

19. Kulmala, M. *et al.* Toward direct measurement of atmospheric nucleation. *Science.* **318**, 89–92 (2007).

20. Formisano, V., Maturilli, A., Giuranna, M., D'Aversa, E. & Lopez-Valverde, M. A. Observations of non-LTE emission at 4–5 microns with the planetary Fourier spectrometer abord the Mars Express mission. *Icarus* **182**, 51–67 (2006).

21. Clancy, R. T., Wolff, M. J., Whitney, B. A., Cantor, B. A. & Smith, M. D. Mars equatorial mesospheric clouds: Global occurrence and physical properties from Mars Global Surveyor Thermal Emission Spectrometer and Mars Orbiter Camera limb observations. *J. Geophys. Res. Planets* **112**, E04004 (2007).

22. Scholten, F. *et al.* Concatenation of HRSC colour and OMEGA data for the determination and 3D-parameterization of high-altitude CO2 clouds in the Martian atmosphere. *Planet. Space Sci.* **58**, 1207–1214 (2010).

23. Vincendon, M., Pilorget, C., Gondet, B., Murchie, S. & Bibring, J. New near-IR observations of mesospheric CO2 and H2O clouds on Mars. *J. Geophys. Res. Planets* **116**, E00J02 (2011).

24. Määttänen, A. *et al.* Mapping the mesospheric CO2 clouds on Mars: MEx/OMEGA and MEx/HRSC observations and challenges for atmospheric models. *Icarus* **209**, 452–469 (2010).

25. Määttänen, A. *et al.* Nucleation studies in the Martian atmosphere. *J. Geophys. Res. Planets* **110**, 1–12 (2005).

26. Ortega, I. K. & Kurtén, T. Carbon dioxide–water clusters in the atmosphere of Mars. *Comput. Theor. Chem.* **965**, 353–358 (2011).

27. Peter, K. *et al.* The lower dayside ionosphere of Mars from 14 years of MaRS radio science observations. *Icarus* **359**, 114213 (2021).

28. Zewail, A. H. Laser Femtochemistry. *Science.* **242**, 1645–1653 (1988).

29. Zewail, A. H. Femtochemistry: Atomic-scale dynamics of the chemical bond. *J. Phys. Chem. A* **104**, 5660–5694 (2000).

30. Lépine, F., Ivanov, M. Y. & Vrakking, M. J. J. Attosecond molecular dynamics: Fact or fiction? *Nat. Photonics* **8**, 195–204 (2014).

31. Kling, M. F. *et al.* Control of electron localization in molecular dissociation. *Science.* **312**, 246–248 (2006).

32. Sansone, G. *et al.* Electron localization following attosecond molecular photoionization. *Nature* **465**, 763–766 (2010).

33. Siu, W. *et al.* Attosecond control of dissociative ionization of O2 molecules. *Phys. Rev. A* **84**, 63412 (2011).

34. Lucchini, M. *et al.* Autoionization and ultrafast relaxation dynamics of highly excited states in N 2. *Phys. Rev. A - At. Mol. Opt. Phys.* **86**, 1–4 (2012).

35. Belshaw, L. *et al.* Observation of ultrafast charge migration in an amino acid. *J. Phys. Chem. Lett.* **3**, 3751–3754 (2012).

36. Calegari, F. *et al.* Attosecond spectroscopy of bio-chemically relevant molecules. *La Riv. del Nuovo Cim.* **41**, 415–461 (2018).

37. Calegari, F. *et al.* Ultrafast electron dynamics in phenylalanine initiated by attosecond pulses. *Science.* **346**, 336–339 (2014).

38. Kraus, P. M. *et al.* Measurement and laser control of attosecond charge migration in ionized iodoacetylene. *Science.* **350**, 790–795 (2015).

39. Yu, X. *et al.* Femtosecond Time-Resolved Neighbor Roles in the Fragmentation Dynamics of Molecules in a Dimer. *Phys. Rev. Lett.* **129**, 23001 (2022).

40. Gong, X. *et al.* Attosecond spectroscopy of size-resolved water clusters. *Nature* **609**, 507–511 (2022).

41. Erk, B. *et al.* CAMP@FLASH: an end-station for imaging, electron- and ion-spectroscopy, and pump-probe experiments at the FLASH free-electron laser. *J. Synchrotron Radiat.* **25**, 1529–1540 (2018).

42. Berrah, N. *et al.* Femtosecond-resolved observation of the fragmentation of buckminsterfullerene following X-ray multiphoton ionization. *Nat. Phys.* **15**, 1279–1283 (2019).

43. Murphy, B. F. *et al.* Femtosecond X-ray-induced explosion of C 60 at extreme intensity. *Nat. Commun.* **5**, 4281 (2014).

44. Fermi, E. *Nuclear physics: a course given by Enrico Fermi at the University of Chicago*. (University of Chicago Press, 1950).

45. Dirac, P. A. M. The quantum theory of the emission and absorption of radiation. *Proc. R. Soc. London. Ser. A, Contain. Pap. a Math. Phys. Character* **114**, 243–265 (1927).

46. Zhang, J. M. & Liu, Y. Fermi's golden rule: Its derivation and breakdown by an ideal model. *Eur. J. Phys.* **37**, 0–13 (2016).

47. Green, J. C. & Decleva, P. Photoionization cross-sections: A guide to electronic structure. *Coord. Chem. Rev.* **249**, 209–228 (2005).

48. Kosugi, N. Exchange interaction in core excitation of diatomic systems. **289**, 117–134 (2003).

49. Schöffler, M. S. *et al.* Ultrafast probing of core hole localization in N2. *Science.* **320**, 920–923 (2008).

50. Guillemin, R. *et al.* Selecting core-hole localization or delocalization in CS 2 by photofragmentation dynamics. *Nat. Commun.* **6**, 1–6 (2015).

51. Siegbahn, H., Asplund, L. & Kelfve, P. The Auger electron spectrum of water vapour. *Chem. Phys. Lett.* **35**, 330–335 (1975).

52. Inhester, L. *et al.* Chemical Understanding of the Limited Site-Specificity in Molecular Inner-Shell Photofragmentation. *J. Phys. Chem. Lett.* **9**, 1156–1163 (2018).

53. Nicolas, C. & Miron, C. Lifetime broadening of core-excited and -ionized states. *J. Electron Spectros. Relat. Phenomena* **185**, 267–272 (2012).

54. Sałek, P. *et al.* Resonant X-ray Raman scattering involving avoided crossings in the final-state potential-energy curves. *Phys. Rev. A - At. Mol. Opt. Phys.* **62**, 062506–062501 (2000).

55. Beerwerth, R. & Fritzsche, S. MCDF calculations of Auger cascade processes. *Eur. Phys. J. D* **71**, 253 (2017).

56. Carlson, T. A. & Krause, M. O. Electron Shake-Off Resulting from K-Shell Ionization in Neon Measured as a Function of Photoelectron Velocity. *Phys. Rev.* **140**, A1057–A1064 (1965).

57. Hatano, Y. Spectroscopy and dynamics of molecular superexcited states. Aspects of primary processes of radiation chemistry. *Radiat. Phys. Chem.* **67**, 187–198 (2003).

58. Hjelte, I. *et al.* Evidence for ultra-fast dissociation of molecular water from resonant Auger spectroscopy. *Chem. Phys. Lett.* **334**, 151–158 (2001).

59. Zhou, X. *et al.* Probing and controlling non-Born-Oppenheimer dynamics in

highly excited molecular ions. *Nat. Phys.* **8**, 232–237 (2012).

60. Sisourat, N., Kryzhevoi, N. V, Scheit, S., Jahnke, T. & Cederbaum, L. S. Ultralong-range energy transfer by interatomic Coulombic decay in an extreme quantum system. **6**, 6–9 (2010).

61. Jahnke, T. *et al.* Interatomic and intermolecular coulombic decay. *Chem. Rev.* **120**, 11295–11369 (2020).

62. Scheit, S., Cederbaum, L. S. & Meyer, H.-D. Time-dependent interplay between electron emission and fragmentation in the interatomic Coulombic decay. *J. Chem. Phys.* **118**, 2092–2107 (2003).

63. Saito, N., De Fanis, A., Koyano, I. & Ueda, K. Nuclear dynamics of core-excited and ionized small polyatomic molecules probed by multiple coincidence momentum imaging technique. *Phys. Scr. T* **T110**, 90–95 (2004).

64. Ueda, K. Nuclear motion, symmetry breaking and dissociation dynamics of core-excited polyatomic molecules. *Surf. Rev. Lett.* **9**, 21–29 (2002).

65. Neeb, M., Rubensson, J.-E., Biermann, M. & Eberhardt, W. Coherent excitation of vibrational wave functions observed in core hole decay spectra of O2, N2 and CO. *J. Electron Spectros. Relat. Phenomena* **67**, 261–274 (1994).

66. Kukk, E., Bozek, J. D. & Berrah, N. Photoexcitation and Auger decay of the Renner-Teller split C 1s-1 pi*u state in CO2. *Phys. Rev. A - At. Mol. Opt. Phys.* **62**, 9 (2000).

67. Laksman, J. *et al.* Role of the Renner-Teller effect after core hole excitation in the dissociation dynamics of carbon dioxide dication. *J. Chem. Phys.* **136**, 104303 (2012).

68. Muramatsu, Y. *et al.* Direct Probe of the Bent and Linear Geometries of the Core-Excited Renner-Teller Pair States by Means of the Triple-Ion-Coincidence Momentum Imaging Technique. *Phys. Rev. Lett.* **88**, 4 (2002).

69. Miron, C. *et al.* Mapping potential energy surfaces by core electron excitation: The resonant Auger decay spectrum of BF3. *Chem. Phys. Lett.* **359**, 48–54 (2002).

70. Saito, N., De Fanis, A., Koyano, I. & Ueda, K. Nuclear Dynamics of Core-Excited and Ionized Small Polyatomic Molecules Probed by Multiple Coincidence Momentum Imaging Technique. *Phys. Scr.* **2004**, 90 (2004).

71. Ueda, K. *et al.* Anisotropic Ultrafast Dissociation Probed by the Doppler Effect in Resonant Photoemission from ${\mathrm{C}\mathrm{F}}_{4}$. *Phys. Rev. Lett.* **90**, 233006 (2003).

72. Morin, P. & Miron, C. Ultrafast dissociation : An unexpected tool for probing molecular dynamics. *J. Electron Spectros. Relat. Phenomena* **185**, 259–266 (2012).

73. Travnikova, O. *et al.* Ultrafast dissociation of ammonia: Auger Doppler effect and redistribution of the internal energy. *Phys. Chem. Chem. Phys.* **24**, 5842–5854 (2022).

74. Pahl, E., Brand, J., Cederbaum, L. S. & Tarantelli, F. Impact of narrow-band excitation on resonant decay spectra. *Phys. Rev. A* **60**, 1079–1090 (1999).

75. Nenner, I. *et al.* Site Selective Fragmentation with Soft X-rays: From Gaseous Polyatomic Molecules, Free Clusters, Polymers, Adsorbates to Biological Macromolecules. *Zeitschrift für Phys. Chemie* **195**, 43–63 (1996).

76. Eberhardt, W. Fragmentation of Small Molecules Following Soft X-Ray Excitation. in *X-Ray Spectroscopy in Atomic and Solid State Physics* (eds. Ferreira, J. G. & Ramos, M. T.) vol. 50 227–236 (Springer US, 1988).

77. Thomas, T. D., Saethre, L. J., Sorensen, S. L. & Svensson, S. Vibrational structure in the carbon 1s ionization of hydrocarbons: Calculation using electronic structure theory and the equivalent-cores approximation. *J. Chem. Phys.* **109**, 1041–1051 (1998).

78. Maclot, S. *et al.* Dissociation dynamics of the diamondoid adamantane upon photoionization by XUV femtosecond pulses. *Sci. Rep.* **10**, 1–12 (2020).

79. Levola, H. *et al.* Ionization-site effects on the photofragmentation of chloro- and bromoacetic acid molecules. *Phys. Rev. A - At. Mol. Opt. Phys.* **92**, 1–10 (2015).

80. Aguirre, N. F., Díaz-Tendero, S., Hervieux, P. A., Alcamí, M. & Martín, F. M3C: A Computational Approach to Describe Statistical Fragmentation of Excited Molecules and Clusters. *J. Chem. Theory Comput.* **13**, 992–1009 (2017).

81. Kukk, E. *et al.* Internal energy dependence in x-ray-induced molecular fragmentation: An experimental and theoretical study of thiophene. *Phys. Rev. A - At. Mol. Opt. Phys.* **91**, 1–7 (2015).

82. Miron, C., Simon, M., Leclercq, N., Hansen, D. L. & Morin, P. Site-selective photochemistry of core excited molecules: Role of the internal energy. *Phys. Rev. Lett.* **81**, 4104–4107 (1998).

83. Hitchcock, A. P., Neville, J. J., Ju̇rgensen, A. & Cavell, R. G. Ionic fragmentation of inner-shell excited molecules. *J. Electron Spectros. Relat. Phenomena* **88**–**91**, 71–75 (1998).

84. Sorensen, S. L. *et al.* Site-selective participator decay of core- excited

butadiene. *J. Chem. Phys.* **105**, 10719–10724 (1996).

85. Oghbaiee, S. *et al.* Site-dependent nuclear dynamics in core-excited butadiene. *Phys. Chem. Chem. Phys.* **24**, 28825–28830 (2022).

86. Hatherly, P. A., Codling, K., Stankiewicz, M. & Roper, M. Symmetry effects in site-specific fragmentation of carbon dioxide. *J. Electron Spectros. Relat. Phenomena* **79**, 407–410 (1996).

87. Eberhardt, W. *et al.* Site-Specific Fragmentation of Small Molecules Following Soft-X-Ray Excitation. *Phys. Rev. Lett.* **50**, 1038–1041 (1983).

88. Bolognesi, P. *et al.* Site- and state-selected photofragmentation of 2Br-pyrimidine. *Phys. Chem. Chem. Phys.* **17**, 24063–24069 (2015).

89. Kooser, K. *et al.* Resonant Auger electron–photoion coincidence study of the fragmentation dynamics of an acrylonitrile molecule. *J. Phys. B At. Mol. Opt. Phys.* **43**, 235103 (2010).

90. Itälä, E. *et al.* Molecular fragmentation of pyrimidine derivatives following site-selective carbon core ionization. *J. Electron Spectros. Relat. Phenomena* **184**, 119–124 (2011).

91. Rühl, E. Core level excitation, ionization, relaxation, and fragmentation of free clusters. *Int. J. Mass Spectrom.* **229**, 117–142 (2003).

92. Echt, O. *et al.* Dissociation channels of multiply charged van der Waals clusters. *Phys. Rev. A* **38**, 3236–3248 (1988).

93. Rayleigh, Lord. XX. On the equilibrium of liquid conducting masses charged with electricity. *London, Edinburgh, Dublin Philos. Mag. J. Sci.* **14**, 184–186 (1882).

94. Echt, O., Sattler, K. & Recknagel, E. Critical sizes for stable multiply charged CO2 clusters. *Phys. Lett. A* **90**, 185–189 (1982).

95. Schröder, T., Schinke, R., Liu, S., Bačić, Z. & Moskowitz, J. W. Photodissociation of HF in ArnHF (n=1–14,54) van der Waals clusters: Effects of the solvent cluster size on the solute fragmentation dynamics. *J. Chem. Phys.* **103**, 9228–9241 (1995).

96. Garvey, J. F. & Bernstein, R. B. Solvated NH5+ formed within ionized clusters of ammonia and ammonia-benzene. *Chem. Phys. Lett.* **143**, 13–18 (1988).

97. Schriver, K. E., Camarena, A. M., Hahn, M. Y., Paguia, A. J. & Whetten, R. L. Elementary photoprocesses in benzene clusters. *J. Phys. Chem.* **91**, 1786–1789 (1987).

98. Shinohara, H., Sato, H. & Washida, N. Photoionization mass spectroscopic

studies of ethylene and acetylene clusters: Intracluster excess energy dissipation. *J. Phys. Chem.* **94**, 6718–6723 (1990).

99. Hans, A. *et al.* Core-level interatomic Coulombic decay in van der Waals clusters. *Phys. Rev. Res.* **2**, 12022 (2020).

100. Trinter, F. *et al.* Resonant Auger decay driving intermolecular Coulombic decay in molecular dimers. *Nature* **505**, 664–666 (2014).

101. Kryzhevoi, N. V & Cederbaum, L. S. Nonlocal Effects in the Core Ionization and Auger Spectra of Small Ammonia Clusters. *J. Phys. Chem. B* **115**, 5441–5447 (2011).

102. Mucke, M. *et al.* A hitherto unrecognized source of low-energy electrons in water. *Nat. Phys.* **6**, 143–146 (2010).

103. Iskandar, W. *et al.* Tracing intermolecular Coulombic decay of carbon-dioxide dimers and oxygen dimers after valence photoionization. *Phys. Rev. A* **99**, 1–13 (2019).

104. Liénard, A. *Champ électrique et magnétique produit par une charge électrique concentrée en un point et animée d'un mouvement quelconque.* (G. Carré et C. Naud, 1898).

105. Pollock, H. C. The discovery of synchrotron radiation. *Am. J. Phys.* **51**, 278–280 (1983).

106. Cammarata, M. *et al.* Chopper system for time resolved experiments with synchrotron radiation. *Rev. Sci. Instrum.* **80**, (2009).

107. Bearden, J. A. X-ray wavelengths. *Rev. Mod. Phys.* **39**, 78–124 (1967).

108. Marra, P. Theoretical approach to direct resonant inelastic x-ray scattering on magnets and superconductors. *PhD Thesis* (2016).

109. Bässler, M. *et al.* Soft x-ray undulator beam line 1411 at MAX-II for gases, liquids and solid samples. *J. Electron Spectros. Relat. Phenomena* **101–103**, 953–957 (1999).

110. Lindblad, A., Söderström, J., Nicolas, C., Robert, E. & Miron, C. A multi purpose source chamber at the PLEIADES beamline at SOLEIL for spectroscopic studies of isolated species: Cold molecules, clusters, and nanoparticles. *Rev. Sci. Instrum.* **84**, 113105 (2013).

111. Continetti, R. E. Coincidence spectroscopy. *Annu. Rev. Phys. Chem.* **52**, 165–192 (2001).

112. Arion, T. & Hergenhahn, U. Coincidence spectroscopy: Past, present and perspectives. *J. Electron Spectros. Relat. Phenomena* **200**, 222–231 (2015).

113. Becker, U. & Shirley, D. A. *VUV and Soft X-ray Photoionization*. (Springer

Science & Business Media, 2012).

114. Ulrich, V. *et al.* Photoelectron-auger electron coincidence spectroscopy of free molecules: New experiments. *J. Electron Spectros. Relat. Phenomena* **183**, 70–79 (2011).

115. Eland, J. H. D. Photoelectron-photoion coincidence spectroscopy. I. Basic principles and theory. *Int. J. Mass Spectrom. Ion Phys.* **8**, 143–151 (1972).

116. Céolin, D., Miron, C., Simon, M. & Morin, P. Auger electron–ion coincidence studies to probe molecular dynamics. *J. Electron Spectros. Relat. Phenomena* **141**, 171–181 (2004).

117. Ladislas Wiza, J. Microchannel plate detectors. *Nucl. Instruments Methods* **162**, 587–601 (1979).

118. Jagutzki, O. *et al.* Multiple hit readout of a microchannel plate detector with a three-layer delay-line anode. *IEEE Trans. Nucl. Sci.* **49 II**, 2477–2483 (2002).

119. Zhu, J. & Hill, III, W. T. Momentum and correlation spectra following intense-field dissociative ionization of H_2. *J. Opt. Soc. Am. B* **14**, 2212 (1997).

120. Frasinski, L. J., Stankiewicz, M., Randall, K. J., Hatherly, P. A. & Codling, K. Dissociative photoionisation of molecules probed by triple coincidence; Double time-of-flight techniques. *J. Phys. B At. Mol. Phys.* **19**, L819 (1986).

121. Eland, J. H. D., Wort, F. S. & Royds, R. N. A photoelectron-ion-ion triple coincidence technique for the study of double photoionization and its consequences. *J. Electron Spectros. Relat. Phenomena* **41**, 297–309 (1986).

122. Ueda, K. & Eland, J. H. D. Molecular photodissociation studied by VUV and soft x-ray radiation. *J. Phys. B At. Mol. Opt. Phys.* **38**, S839 (2005).

123. Eppink, A. T. J. B. & Parker, D. H. Velocity map imaging of ions and electrons using electrostatic lenses: Application in photoelectron and photofragment ion imaging of molecular oxygen. *Rev. Sci. Instrum.* **68**, 3477–3484 (1997).

124. Takahashi, M., Cave, J. P. & Eland, J. H. D. Velocity imaging photoionization coincidence apparatus for the study of angular correlations between electrons and fragment ions. *Rev. Sci. Instrum.* **71**, 1337–1344 (2000).

125. Mårtensson, N. *et al.* A very high resolution electron spectrometer. *J. Electron Spectros. Relat. Phenomena* **70**, 117–128 (1994).

126. Laksman, J., Céolin, D., Månsson, E. P., Sorensen, S. L. & Gisselbrecht, M. Development and characterization of a multiple-coincidence ion-momentum

imaging spectrometer. *Rev. Sci. Instrum.* **84**, 123113 (2013).

127. Laksman, J. Nuclear motion in molecular ions studied with synchrotron radiation and multicoincidence momentum imaging spectrometry. *PhD Thesis* (2012).

128. Hosaka, K. *et al.* Coincidence velocity imaging apparatus for study of angular correlations between photoelectrons and photofragments. *Japanese J. Appl. Physics, Part 1 Regul. Pap. Short Notes Rev. Pap.* **45**, 1841–1849 (2006).

129. Morin, P., Simon, M., Miron, C., Leclercq, N. & Hansen, D. L. Electron-ion spectroscopy: A probe of molecular dynamics. *J. Electron Spectros. Relat. Phenomena* **93**, 49–60 (1998).

130. Miron, C., Simon, M., Leclercq, N. & Morin, P. New high luminosity 'double toroidal' electron spectrometer. *Rev. Sci. Instrum.* **68**, 3728–3737 (1997).

131. Liu, X. J., Nicolas, C., Robert, E. & Miron, C. EPICEA: Probing High-Energy Electron Emission in the Molecular Frame. *J. Phys. Conf. Ser.* **488**, 13–14 (2014).

132. Le Guen, K. *et al.* Development of a four-element conical electron lens dedicated to high resolution Auger electron-ion(s) coincidence experiments. *Rev. Sci. Instrum.* **73**, 3885 (2002).

133. Wiley, W. C. & McLaren, I. H. Time-of-flight mass spectrometer with improved resolution. *Rev. Sci. Instrum.* **26**, 1150–1157 (1955).

134. Eland, J. H. D. & Pearson, A. H. Simple radial position-sensitive detector with short deadtime for time-of-flight and coincidence experiments. *Meas. Sci. Technol.* **1**, 36–40 (1990).

135. Moshammer, R., Unverzagt, M., Schmitt, W., Ullrich, J. & Schmidt-Böcking, H. A 4 π recoil-ion electron momentum analyzer: A high-resolution 'microscope' for the investigation of the dynamics of atomic, molecular and nuclear reactions. *Nucl. Instruments Methods Phys. Res. Sect. B Beam Interact. with Mater. Atoms* **108**, 425–445 (1996).

136. Chen, Y. Ultrafast Photoionization Dynamics Studied with Coincidence Momentum Imaging Spectrometers. *PhD Thesis* (2019).

137. Hellings, G. J. A., Ottevanger, H., Knibbeler, C. L. C. M., Van Engelshoven, J. & Brongersma, H. H. Potential distribution and focusing properties of toroidal deflection plates. Application to simultaneous energy and angle-resolved charged particle spectroscopy. *J. Electron Spectros. Relat. Phenomena* **49**, 359–382 (1989).

138. Hadjarab, F. & Erskine, J. L. Image properties of the hemispherical analyzer applied to multichannel energy detection. *J. Electron Spectros. Relat. Phenomena* **36**, 227–243 (1985).

139. Bapat, B. & Krishnakumar, E. Effusive molecular beam from a capillary array for improved resolution time-of-flight and collision spectrometry. *Rapid Commun. mass Spectrom.* **9**, 199–202 (1995).

140. Howard, W. M. Density field for rarefied flow through an orifice. *Phys. Fluids* **4**, 521–524 (1961).

141. Rugamas, F. *et al.* Angular profiles of molecular beams from effusive tube sources: I. Experiment. *Meas. Sci. Technol.* **11**, 1750–1765 (2000).

142. Smalley, R. E., Wharton, L. & Levy, D. H. Molecular Optical Spectroscopy with Supersonic Beams and Jets. *Acc. Chem. Res.* **10**, 139–145 (1977).

143. Pauly, H., Toennies, J. P. & Amdur, I. 3. Neutral-Neutral Interactions. in *Atomic and Electron Physics* vol. 7 227–360 (Academic Press, 1968).

144. Lubman, D. M., Rettner, C. T. & Zare, R. N. How Isolated Are Molecules in a Molecular Beam? *J. Phys. Chem.* **86**, 1129–1135 (1982).

145. Anderson, J. B. & Fenn, J. B. Velocity distributions in molecular beams from nozzle sources. *Phys. Fluids* **8**, 780–787 (1965).

146. Patel, M., Thomas, J. & Joshi, H. C. Flow characterization of supersonic gas jets: Experiments and simulations. *Vacuum* **192**, 110440 (2021).

147. Ashkenas, H. & Sherman, F. S. Structure and utilization of supersonic free jets in low density wind tunnels. *Rarefied Gas Dyn. -Proceedings Fourth Int. Symp. held Inst. Aerosp. Stud. Toronto* **222**, 84–105 (1964).

148. Braun, J., Day, P. K., Toennies, J. P., Witte, G. & Neher, E. Micrometer-sized nozzles and skimmers for the production of supersonic He atom beams. *Rev. Sci. Instrum.* **68**, 3001–3009 (1997).

149. Murphy, H. R. & Miller, D. R. Effects of nozzle geometry on kinetics in free-jet expansions. *J. Phys. Chem.* **88**, 4474–4478 (1984).

150. Bird, G. A. *Molecular Gas Dynamics And The Direct Simulation Of Gas Flows. Molecular Gas Dynamics And The Direct Simulation Of Gas Flows* (Clarendon Press, 1994).

151. Luria, K., Christen, W. & Even, U. Generation and propagation of intense supersonic beams. *J. Phys. Chem. A* **115**, 7362–7367 (2011).

152. Campargue, R. Progress in overexpanded supersonic jets and skimmed molecular beams in free-jet zones of silence. *J. Phys. Chem.* **88**, 4466–4474 (1984).

153. Bird, G. A. Transition regime behavior of supersonic beam skimmers. *Phys. Fluids* **19**, 1486–1491 (1976).

154. McDaniels, J. T., Continetti, R. E. & Miller, D. R. The effect of nozzle geometry on cluster formation in molecular beam sources. in *AIP Conference Proceedings* vol. 663 670–677 (American Institute of Physics, 2003).

155. Bailey, A. B., Dawbarn, R. & Busby, M. R. Effects of skimmer and endwall temperature of condensed molecular beams. *AIAA J.* **14**, 91–92 (1976).

156. Hagena, O. F. Condensation in free jets: Comparison of rare gases and metals. *Zeitschrift für Phys. D Atoms, Mol. Clust.* **4**, 291–299 (1987).

157. Harnes, J., Winkler, M., Lindblad, A., Sæthre, L. J. & Børve, K. J. Size of free neutral CO2 clusters from carbon 1s ionization energies. *J. Phys. Chem. A* **115**, 10408–10415 (2011).

158. Oostenrijk, B. Charge and proton dynamics in molecules and free clusters from atomic to nanometer scale. *PhD Thesis* (2018).

159. Slattery, A. E. *et al.* Spectroscopy and metastability of CO 22+ molecular ions. *J. Chem. Phys.* **122**, 084317 (2005).

160. D Mathur, L H Andersen, P Hvelplund, D Kella & C P Safvan. Long-lived, doubly charged diatomic and triatomic molecular ions. *J. Phys. B At. Mol. Opt. Phys.* **28**, 3415 (1995).

161. Frasinski, L. J., Stankiewicz, M., Hatherly, P. A. & Codling, K. Removal of false coincidences in triple coincidence experiments employing continuous excitation. *Meas. Sci. Technol.* **3**, 1188–1191 (1992).

162. Maul, C. & Gericke, K. H. Aspects of Photoinduced Molecular Three-body Decay. *J. Phys. Chem. A* **104**, 2531–2541 (2000).

163. Babikov, D. *et al.* Dalitz plot analysis of three-body fragmentation of Na3+ excited by He impact. *J. Chem. Phys.* **116**, 4871–4876 (2002).

164. Matsuda, A., Takahashi, E. J. & Hishikawa, A. Dalitz plot analysis of Coulomb exploding O3 in ultrashort intense laser fields. *J. Chem. Phys.* **127**, 114318 (2007).

165. Dalitz, R. H. CXII. On the analysis of τ-meson data and the nature of the τ-meson. *London, Edinburgh, Dublin Philos. Mag. J. Sci.* **44**, 1068–1080 (1953).

166. Zeng, L. & Seager, S. A Computational Tool to Interpret the Bulk Composition of Solid Exoplanets based on Mass and Radius Measurements. *Publ. Astron. Soc. Pacific* **120**, 983–991 (2008).

167. Liu, X. J., Nicolas, C. & Miron, C. Design of a lens table for a double toroidal electron spectrometer. *Rev. Sci. Instrum.* **84**, 033105 (2013).

168. Lytken, O., Wechsler, D. & Steinrück, H. P. Removing photoemission features from Auger-yield NEXAFS spectra. *J. Electron Spectros. Relat. Phenomena* **218**, 35–39 (2017).

169. Prümper, G. & Ueda, K. Electron-ion-ion coincidence experiments for photofragmentation of polyatomic molecules using pulsed electric fields: Treatment of random coincidences. *Nucl. Instruments Methods Phys. Res. Sect. A Accel. Spectrometers, Detect. Assoc. Equip.* **574**, 350–362 (2007).

170. Patzer, A., Schütz, M., Möller, T. & Dopfer, O. Infrared Spectrum and Structure of the Adamantane Cation: Direct Evidence for Jahn-Teller Distortion. *Angew. Chemie* **124**, 5009–5013 (2012).

171. Dutler, R., Rauk, A., Sorensen, T. S. & Whitworth, and S. M. An ab initio molecular orbital study of the 2-Adamantyl cation. *J. Am. Chem. Soc* **111**, 9024–9029 (1989).

172. Xiong, T. & Saalfrank, P. Vibrationally Broadened Optical Spectra of Selected Radicals and Cations Derived from Adamantane: A Time-Dependent Correlation Function Approach. *J. Phys. Chem. A* **123**, 8871–8880 (2019).

173. Yan, G., Brinkmann, N. R. & Schaefer, H. F. Energetics and Structures of Adamantane and the 1- and 2-Adamantyl Radicals, Cations, and Anions. *J. Phys. Chem. A* **107**, 9479–9485 (2003).

174. Candian, A., Bouwman, J., Hemberger, P., Bodi, A. & Tielens, A. G. G. M. Dissociative ionisation of adamantane: A combined theoretical and experimental study. *Phys. Chem. Chem. Phys.* **20**, 5399–5406 (2018).

175. Steglich, M., Huisken, F., Dahl, J. E., Carlson, R. M. K. & Henning, T. Electronic spectroscopy of fuv-irradiated diamondoids: A combined experimental and theoretical study. *Astrophys. J.* **729**, 91 (2011).

176. Polfer, N., Sartakov, B. G. & Oomens, J. The infrared spectrum of the adamantyl cation. *Chem. Phys. Lett.* **400**, 201–205 (2004).

177. Bouwman, J., Horst, S. & Oomens, J. Spectroscopic Characterization of the Product Ions Formed by Electron Ionization of Adamantane. *ChemPhysChem* **19**, 3211–3218 (2018).

178. Boyer, A., Hervé, M., Scognamiglio, A., Loriot, V. & Lépine, F. Time-resolved relaxation and cage opening in diamondoids following XUV ultrafast ionization. *Phys. Chem. Chem. Phys.* **23**, 27477–27483 (2021).

179. Kappe, M. *et al.* Electronic spectroscopy of cationic adamantane clusters and

dehydrogenated adamantane in helium droplets. *Phys. Chem. Chem. Phys.* 23142–23151 (2022) doi:10.1039/d2cp03523e.

180. Roithová, J. & Schröder, D. On a possible growth mechanism for polycyclic aromatic hydrocarbon dications: C7H62++C2H2. *Chem. - A Eur. J.* **13**, 2893–2902 (2007).

181. Milko, P., Schröder, D., Schwarz, H. & Roithová, J. General trends in dissociations of medium-sized hydrocarbon dications. *Int. J. Mass Spectrom.* **277**, 107–112 (2008).

182. Roithová, J., Schröder, D., Berger, R. & Schwarz, H. Doubly protonated benzene in the gas phase. *J. Phys. Chem. A* **110**, 1650–1657 (2006).

183. Roithová, J. *et al.* Energetics of fragmentations of indene dication from photoionization experiments. *Chem. Phys. Lett.* **423**, 254–259 (2006).

184. Perreault, H., Ramaley, L., Benoit, F. M., Sim, P. G. & Boyd, R. K. Fragmentation reactions of doubly charged ions of nitrogenous heterocyclic aromatic compounds. *J. Phys. Chem.* **95**, 4989–4998 (1991).

185. Urquhart, S. G. & Gillies, R. Rydberg-valence mixing in the carbon Is near-edge X-ray absorption fine structure spectra of gaseous alkanes. *J. Phys. Chem. A* **109**, 2151–2159 (2005).

186. Ueda, K. *et al.* Rydberg-valence mixing in the C 1s excited states of CH4 probed by electron spectroscopy. *Chem. Phys. Lett.* **236**, 311–317 (1995).

187. Willey, T. M. *et al.* Molecular limits to the quantum confinement model in diamond clusters. *Phys. Rev. Lett.* **95**, 2–5 (2005).

188. Willey, T. M. *et al.* X-ray spectroscopic identification of strain and structure-based resonances in a series of saturated carbon-cage molecules: Adamantane, twistane, octahedrane, and cubane. *J. Vac. Sci. Technol. A* **39**, 053208 (2021).

189. Ungier, L. & Thomas, T. D. Near threshold excitation of KVV Auger spectra in carbon monoxide using electron-electron coincidence spectroscopy. *J. Chem. Phys.* **82**, 3146–3151 (1984).

190. Sundin, S. *et al.* Vibrationally selective resonant Auger spectroscopy of the 3p core-to-Rydberg excitation in CO. *Phys. Rev. A - At. Mol. Opt. Phys.* **56**, 480–487 (1997).

191. Thompson, D. B., Ji, D., Chen, S. Y. & Hanson, D. M. Excitation and decay spectra of core-excited resonances in acetaldehyde, propionaldehyde and acetone. *J. Phys. B At. Mol. Opt. Phys.* **32**, 5711–5724 (1999).

192. Kosugi, N. *et al.* Rydberg and valence states in the C 1s photoabsorption and resonance Auger spectra of CH3F. *Chem. Phys. Lett.* **246**, 475–480 (1995).

193.   Boschi, R. *et al.* Complete valence shell electronic structure of adamantane from He I and He II photoelectron spectroscopy. *J. Electron Spectros. Relat. Phenomena* **2**, 377–380 (1973).

194.   Morini, F., Watanabe, N., Kojima, M., Deleuze, M. S. & Takahashi, M. Influence of molecular vibrations on the valence electron momentum distributions of adamantane. *J. Chem. Phys.* **146**, 094307 (2017).

195.   Cederbaum, L. S. & Zobeley, J. Ultrafast charge migration by electron correlation. *Chem. Phys. Lett.* **307**, 205–210 (1999).

196.   Remacle, F., Levine, R. D. & Ratner, M. A. Charge directed reactivity: A simple electronic model, exhibiting site selectivity, for the dissociation of ions. *Chem. Phys. Lett.* **285**, 25–33 (1998).

197.   Brito, A. N. De *et al.* Memories of excited femtoseconds: effects of core–hole localization after Auger decay in the fragmentation of ozone. *Chem. Phys. Lett.* **328**, 177–187 (2000).

198.   Monfredini, T., Fantuzzi, F., Nascimento, M. A. C., Wolff, W. & Boechat-Roberty, H. M. Single and Double Photoionization and Photodissociation of Toluene By Soft X-Rays in a Circumstellar Environment. *Astrophys. J.* **821**, 4 (2016).

199.   Stockett, M. H. *et al.* Competitive Dehydrogenation and Backbone Fragmentation of Superhydrogenated PAHs: A Laboratory Study. *Astrophys. J.* **913**, 46 (2021).

200.   Wallace, W. E. & Fischer, D. A. Resonant soft X-ray photofragmentation of propane. *J. Electron Spectros. Relat. Phenomena* **130**, 1–6 (2003).

201.   Reitsma, G. *et al.* Deexcitation dynamics of superhydrogenated polycyclic aromatic hydrocarbon cations after soft-x-ray absorption. *Phys. Rev. Lett.* **113**, 1–5 (2014).

202.   Dietrich, H.-J., Jung, R., Waterstradt, E. & Müller-Dethlefs, K. Correlated-Pair Fragmentation and Charge-Transfer of CO2 Clusters from Atom-Specific 1s Core Level Excitation. *Berichte der Bunsengesellschaft für Phys. Chemie* **96**, 1179–1183 (1992).

203.   Romanowski, G. & Wanczek, K. P. Studies of reactions of ionized carbon dioxide microclusters. *Int. J. Mass Spectrom. Ion Process.* **95**, 223–239 (1989).

204.   Romanowski, G. & Wanczek, K. P. Temperature and size-dependent fragmentation of carbon dioxide clusters. *Int. J. Mass Spectrom. Ion Process.* **62**, 277–288 (1984).

205.   Heinbuch, S., Dong, F., Rocca, J. J. & Bernstein, E. R. Single photon

ionization of van der Waals clusters with a soft x-ray laser: (CO 2) n and (CO 2) n (H 2O) m. *J. Chem. Phys.* **125**, 154316 (2006).

206. Dąbek, J. & Michalak, L. Size-dependent fragmentation of carbon dioxide clusters. in *Vacuum* vol. 63 555–560 (2001).

207. Wang, C. R., Huang, R. Bin, Liu, Z. Y. & Zheng, L. S. Lognormal size distributions of elemental clusters. *Chem. Phys. Lett.* **227**, 103–108 (1994).

208. Pocsik, I. Atoms, Molecules and Clusters Lognormal distribution as the natural statistics of cluster systems. *Mol. Clust.* **20**, 395–397 (1991).

209. Romanowski, G. & Wanczek, K. P. The influence of stagnation pressure and electron energy on the unimolecular decomposition of CO2 microclusters. *Int. J. Mass Spectrom. Ion Process.* **70**, 247–257 (1986).

210. Jahnke, T. *et al.* Ultrafast energy transfer between water molecules. *Nat. Phys.* **6**, 139–142 (2010).

211. Larimian, S. *et al.* Molecular oxygen observed by direct photoproduction from carbon dioxide. *Phys. Rev. A* **95**, 011404 (2017).

212. Ndome, H., Alcaraz, C. & Hochlaf, M. OOCO+ cation I: Characterization of its isomers and lowest electronic states. *J. Chem. Phys.* **127**, 64312 (2007).

213. Ndome, H., Alcaraz, C. & Hochlaf, M. OOCO+ cation. II. Its role during the atmospheric ion-molecule reactions. *J. Chem. Phys.* **127**, 64313 (2007).

214. Paulson, J. F., Mosher, R. L. & Dale, F. Fast ion-molecule reaction in CO2. *J. Chem. Phys.* **44**, 3025–3028 (1966).

215. Viggiano, A. A., Morris, R. A., Van Doren, J. M. & Paulson, J. F. Temperature, kinetic energy, and internal energy dependences of the rate constant and branching fraction for the reaction of O+ (4S) with CO2. *J. Chem. Phys.* **96**, 270–274 (1992).

216. Viggiano, A. A., Morris, R. A. & Paulson, J. F. Rate constant and branching fraction for the reaction of O+(2D,2P) with CO2. *J. Chem. Phys.* **93**, 1483–1484 (1990).

217. Fehsenfeld, F. C., Schmeltekopf, A. L. & Ferguson, E. E. Thermal-Energy Ion—Neutral Reaction Rates. V. Measured Rate Constants for C+ and CO+ Reactions with O2 and CO2. *J. Chem. Phys.* **45**, 23–25 (1966).

218. Jaffe, S. & Klein, F. S. An ion cyclotron resonance mass spectrometric study of ion molecule reactions in CO2 and CO. *Int. J. Mass Spectrom. Ion Phys.* **14**, 459–466 (1974).

219. Simon, M., LeBrun, T., Morin, P., Lavollée, M. & Maréchal, J. L. A photoelectron-ion multiple coincidence technique applied to core ionization

of molecules. *Nucl. Inst. Methods Phys. Res. B* **62**, 167–174 (1991).

220. Zapadinsky, E., Passananti, M., Myllys, N., Kurtén, T. & Vehkamäki, H. Modeling on Fragmentation of Clusters inside a Mass Spectrometer. *J. Phys. Chem. A* **123**, 611–624 (2019).

221. Meister, S. *et al.* Atomic, molecular and cluster science with the reaction microscope endstation at FLASH2. *Appl. Sci.* **10**, (2020).

222. Schnorr, K. *et al.* Time-resolved study of ICD in Ne dimers using FEL radiation. *J. Electron Spectros. Relat. Phenomena* **204**, 245–256 (2015).

223. Liekhus-Schmaltz, C. E. *et al.* Ultrafast isomerization initiated by X-ray core ionization. *Nat. Commun.* **6**, 8199 (2015).

224. Rolles, D. Time-resolved experiments on gas-phase atoms and molecules with XUV and X-ray free-electron lasers. *Adv. Phys. X* **8**, 2132182 (2023).

225. Zhang, C. *et al.* Laboratory hydrogenation of the photo-fragments of PAH cations: Co-evolution interstellar chemistry. *Astron. Astrophys.* **669**, A41 (2023).

226. Gredel, R. *et al.* Abundances of PAHs in the ISM: confronting observations with experimental results. *Astron. Astrophys.* **530**, A26 (2011).

Introducing the real brains behind this thesis...
Dr. Wally Bunny. He wrote this thesis for Smita
in exchange for a lifetime supply of bananas.